Closed-Loop Combustion Control of Advanced Internal Combustion Engines

by

Donghoon Lee

A dissertation submitted in partial fulfillment
of the requirements for the degree of
Doctor of Philosophy
(Mechanical Engineering)
in The University of Michigan
2011

Doctoral Committee:

Professor Anna G. Stefanopoulou, Chair
Professor Zoran S. Filipi
Professor Jessy W. Grizzle
Associate Research Scientist Michael Kokkolaras

To my parents, my wife and my son.

Acknowledgments

Looking back, I am surprised and at the same time very grateful for all I have received throughout these years. It has certainly shaped me as a person and has led me where I am now. All these years of my Ph.D. studies are full of such gifts.

I would like to express my deepest gratitude to my wonderful advisor, Professor Anna G. Stefanopoulou, for her excellent guidance, caring, patience, and providing me with an excellent atmosphere for doing research. Anna has always been generous with her time and has provided enormously helpful advice on my entire graduate experience not only for my research but also my child care aspect. The members of my dissertation committee, Prof. Grizzle, Prof. Filipi and Dr. Kokkolaras, have generously given their time and expertise to better my work. I thank them for their contribution and their good-natured support. I am grateful to Dr. Janković from Ford Motor company for his encouragement and practical advice. I am also thankful to him for reading my papers, commenting on my views and helping me understand and enrich my ideas. I am also indebted to the members of the Robert Bosch with whom I have interacted during my graduate studies. Particularly, I would like to acknowledge Dr. Hakan Yilmaz, Li Jiang, Mond Alan and Vanier Julien for the many valuable discussions and the experiments in the dynamometer facility that helped me understand my research area better.

I must acknowledge as well the many friends, colleagues, students and teachers who assisted, advised, and supported my research over the years. Especially, I need to express my gratitude and deep appreciation to Dr. Kyungho Ahn and Kwangjae Lee whose friendship, hospitality, knowledge, and wisdom have supported, enlightened, and entertained me over the many years of our friendship. They have consistently helped me keep perspective on what is important in life and shown me how to deal with reality. My appreciation also goes to all the great people at the Powertrain Control Laboratory for their friendship - Jason Siegel, Shyam Jade, Jacob Larimore, Phil Bonkoski, Patrick Gorzelic, Erik Hellstrom, XinFan Lin and Jixin Chen.

Most importantly, none of this would have been possible without the love and patience of my family to whom this dissertation is dedicated to. My family has been a constant

source of love, concern, support and strength all these years. I would like to express my heartfelt gratitude to my parents, parents-in-law, sister and brother, who have always supported and encouraged me with their best wishes. Finally, my wife Jungmi and my son Nathan have always been my pillar, my joy and my guiding light, and I thank them.

Table of Contents

Dedication ii

Acknowledgments iii

List of Tables viii

List of Figures ix

Abstract xiv

Chapter 1 Introduction 1
1.1 Background 1
1.1.1 Background of HCCI Engine 2
1.1.2 Background of FFV Turbocharged SIDI Engine with VVT 5
1.2 Engine System Configuration 7
1.2.1 Single Cylinder Heated-Air Inlet HCCI Engine 7
1.2.2 Turbocharged SIDI Engine with VVT 8
1.3 Overview 10
1.4 Contributions 12

Chapter 2 HCCI Crank Angle Based Model 15
2.1 Introduction 15
2.2 Model Structure 16
2.3 Flow through Throttles and Valves 16
2.3.1 Discharge Coefficient and Reference Flow Area of Throttle Flow . 18
2.3.2 Discharge Coefficient and Reference Flow Area of Valve Flow . . . 20
2.4 Intake and Exhaust Runner Dynamics 20
2.4.1 Intake Runner Dynamics 20
2.4.2 Exhaust Runner Dynamics 22
2.5 Cylinder Dynamics 23
2.5.1 Cylinder Gas Dynamics 23
2.5.2 Cylinder Part Temperatures 24
2.5.3 Woschni Heat Transfer 24
2.5.4 Fuel Mass Fraction Burned Rate 25

2.5.5 Combustion Timing 26
2.6 Steady State Validation 30
2.7 Transient Data Validation 36
2.8 Conclusion 40

Chapter 3 HCCI Closed-loop Combustion Control 42
3.1 Introduction 42
3.2 Mean Value Model and Validation 43
3.2.1 Model Structure and Notation 43
3.2.2 Cycle Averaged Pumping Flows 44
3.2.3 Combustion Timing and Duration 44
3.2.4 Exhaust Temperature 46
3.2.5 Prediction Error with Steady State Data 47
3.2.6 Validation with Transient Data 49
3.3 Combustion Duration Control 50
3.4 Control Analysis and Design 53
3.4.1 Desired Cold and Hot Throttle Settings 53
3.4.2 SISO System and Linearization 54
3.4.3 Feedforward plus PI Feedback Control 56
3.4.4 Heated Inlet Air Temperature Changes 57
3.5 Conclusion 58

Chapter 4 Air Charge Control for Turbocharged Spark Ignition Engines with Internal Exhaust Gas Recirculation 61
4.1 Introduction 61
4.2 Control-Oriented Model and Validation 62
4.3 Static Schedule of VVT 64
4.4 Valve Compensator Design 67
4.5 Simulation and Experiment during Tip-Ins and Tip-Outs 70
4.6 Conclusion 73

Chapter 5 Extremum Seeking of Variable Valve Timing and Spark Timing for On-Board Calibration 75
5.1 Introduction 75
5.2 Combustion Model 76
5.2.1 Combustion Phase 76
5.2.2 Mean Effective Pressure 77
5.2.3 Global Engine Conditions vs. Variable Valve Timing 82
5.2.4 Combustion Statistics 84
5.3 On-Board Calibration Scheme 86
5.3.1 Extremum Seeking Control 87
5.3.2 Extremum Seeking Parameter Selection 89
5.3.3 Simulation Verification 91
5.4 Conclusion 92

Chapter 6 Implementation of Extremum Seeking Control for Spark Timing . . 97
6.1 Introduction 97
6.2 Experimental Setup 97
6.2.1 Engine Characteristics 98
6.2.2 Software and Communication Setup 100
6.3 Extremum Seeking Control Verification 102
6.3.1 Simulation Verification 103
6.3.2 Overview of Experiments 105
6.3.3 ES Verification under Fixed Load 106
6.3.4 ES Verification under Sinusoidal Load 109
6.4 Conclusion 112

Chapter 7 Conclusions and Future Work 115
7.1 Conclusions 115
7.2 Future Work 117

Bibliography 119

List of Tables

Table

1.1 Specifications for a single cylinder heated-air HCCI engine. 8

2.1 Determined parameters in the discharge coefficient equations for cold and hot throttles. 19
2.2 Determined parameters in Arrhenius integral. 28
2.3 Summary of steady-State HCCI dynamometer engine experiment plan with various cold and hot throttle angles. 32
2.4 Mean (μ), standard deviation (σ), Min and Max values of the model prediction error, that is, the difference between the dynamometer engine data and model prediction values. 33
2.5 Summary of transient HCCI dynamometer engine experiment plan with load, throttle, engine speed and load/speed changes. 37

3.1 Summary of steady-State HCCI dynamometer engine experiment with various cold and hot throttle angles. 48
3.2 Mean (μ), standard deviation (σ), Min and Max values of the model prediction error. 48

6.1 Specifications for the optimized FFV engine 101
6.2 Engine operating conditions for extremum seeking (ES) control test with fixed loads. 105
6.3 Engine operating conditions for extremum seeking (ES) control test with sinusoidal loads. 106

List of Figures

Figure

1.1 Schematic of the HCCI engine setup. 8
1.2 Configuration of a turbocharged (TC) gasoline spark ignition direct injection (SIDI) engine equipped with variable intake and exhaust camshafts. . . 9
1.3 Schematic overview of the dissertation. 13

2.1 Schematic diagram and notation for the crank-angle based HCCI model. . . 17
2.2 Single cylinder HCCI engine model structure. 17
2.3 Discharge coefficients based on the cold and hot throttle angles. 19
2.4 Intake and exhaust valve lift (IVL_c, IVL_h and EVL) and corresponding discharge coefficient and reference flow area ($C_DA_{r,c}$, $C_DA_{r,h}$ and $C_DA_{r,e}$). . 21
2.5 Representation of regressed total exhaust heat transfer coefficient $(A_2h_2)_{total}$ [W/K] as a function of injected fuel per each cycle m_{fuel} [mg/cycle], and engine speed N [RPM]. 23
2.6 Prediction error of θ_{SOC} ($\theta_{SOC,sim}$ - $\theta_{SOC,dyno}$) between the dynamometer data and the model prediction. 28
2.7 θ_{CA02} vs. θ_{CA50} regression. 29
2.8 θ_{CA02} vs. θ_{CA90} regression. 31
2.9 All steady state HCCI engine test region for various load conditions at the engine speeds of 1000, 1500 and 2500 RPM. 33
2.10 Comparison of IMEP between the dynamometer engine data and the model simulation: Black solid line and blue dashed line indicate the mean and standard deviation of prediction errors, respectively. 34
2.11 Comparison of AFR between the dynamometer engine data and the model simulation: Black solid line and blue dashed line indicate the mean and standard deviation of prediction errors, respectively. 34
2.12 Comparison of θ_{CA02} between the dynamometer engine data and the model simulation: Black solid line and blue dashed line indicate the mean and standard deviation of prediction errors, respectively. 35
2.13 Comparison of θ_{CA50} between the dynamometer engine data and the model simulation: Black solid line and blue dashed line indicate the mean and standard deviation of prediction errors, respectively. 35

2.14 Comparison of T_2 between the dynamometer engine data and the model simulation: Black solid line and blue dashed line indicate the mean and standard deviation of prediction errors, respectively. 36
2.15 Mass fraction burned (MFB) curves computed from the dynamometer transient test (θ_c = 0%, θ_h = 50% $\rightarrow$ 30%, IMEP $\approx$ 2 bar, N = 1500 RPM). . . 38
2.16 θ_{CA02} and θ_{CA10} for all steady-state data 38
2.17 Load change (θ_c = 0%, θ_h = 100%, T_0 = 39$^\circ C$, T_h = 157$^\circ C$, N = 1500 RPM) : blue dashed lines show the post-processed dynamometer data and red solid lines display the model simulation result 39
2.18 Cold throttle change (θ_c = 30% $\rightarrow$ 50% $\rightarrow$ 30%, θ_h = 100%, T_0 = 34$^\circ C$, T_h = 176$^\circ C$, N = 1500 RPM) : blue dashed lines show the post-processed dynamometer data and red solid lines display the model simulation result . 40
2.19 Hot throttle change (θ_c = 0%, θ_h = 50% $\rightarrow$ 30% $\rightarrow$ 50%, T_0 = 43$^\circ C$, T_h = 185$^\circ C$, N = 1500 RPM) : blue dashed lines show the post-processed dynamometer data and red solid lines display the model simulation result . 41

3.1 Notation used for the crank-angle resolved HCCI engine model. 43
3.2 Comparison between crank-angle based HCCI engine simulation (dot points) and pumping flow map (solid lines) from (3.1) and (3.2). 45
3.3 Comparison of θ_{CA02} and $\Delta\theta_{comb}$ from the steady state dynamometer test (dot points) and (3.4) and (3.5) (solid lines) for different operating conditions. 46
3.4 θ_{CA02} versus θ_{CA50} from dynamometer test. 47
3.5 Comparison of $IMEP$, AFR, θ_{CA02}, θ_{CA50}, $\Delta\theta_{comb}$, and T_2 between the dynamometer engine test and the model simulation for different engine speeds, loads and throttle angles. 49
3.6 Model validation with the load, hot and cold throttle step changes of the single cylinder HCCI engine at N = 1500 rpm. 51
3.7 Comparison between $\Delta\theta_{comb}$ and θ_{CA50} with respect to covariance of IMEP and normalized ISFC. 52
3.8 Optimal cold and hot throttle angles (θ_c^{opt} and θ_h^{opt}) to achieve a desirable combustion duration, $\Delta\theta_{comb}$ = 7.5 CAD, for different loads m_f [mg/cycle] and hot inlet temperatures T_h [^{o}C] at the engine speed of 1500 rpm. 54
3.9 Open loop response of the linearized and nonlinear model during step changes of engine inputs. 55
3.10 Block diagram of feedforward and PI feedback control system. 56
3.11 Comparison between nonlinear open loop (NL-OL) and closed loop (NL-CL) with Feedforward + Integral controller. 57
3.12 Block diagram of feedforward and PI feedback control system with a heat exchanger. 58
3.13 Mean value model responses with and without a heat exchanger model and cold throttle feedforward map. 59
3.14 Crank-angle based model responses with and without a heat exchanger model and cold throttle feedforward map. 60

4.1 Schematic of turbocharged spark ignition direct injection engine equipped with variable intake and exhaust camshafts. 63
4.2 Cylinder pumping flow W_{cyl} versus intake manifold pressure p_{im} with various intake and exhaust valve overlaps v at N = 2000 RPM. 64
4.3 Comparison between dynamometer measurement and model simulation for throttle step change with E0 fuel and a fixed wastegate duty cycle at 0% at N = 2000 RPM; dynamometer engine inputs are presented in the first column and corresponding engine outputs (blue dashed lines) are compared with simulation results (red solid lines) in the second column. 65
4.4 Comparison between dynamometer measurement and model simulation for throttle step change with E85 fuel and a fixed wastegate duty cycle at 0% at N = 2500 RPM; dynamometer engine inputs are presented in the first column and corresponding engine outputs (blue dashed lines) are compared with simulation results (red solid lines) in the second column. 66
4.5 Cylinder pumping flow rate W_{cyl} and intake manifold pressure p_{im} with respect to throttle angles θ_{th} for various intake and exhaust valve overlaps v and corresponding VVT overlap scheduling scheme v at N = 2000 RPM. . . 67
4.6 Cylinder air charge rate W_{cyl} response of the turbocharged engine on VVT overlap v step changes; engine speed is 2000 RPM and throttle is fixed at θ_{th} = 20% (second plot) and θ_{th} = 40% (third plot). 68
4.7 Schematic diagram of VVT turbocharged engine with valve compensator. . 71
4.8 Comparison of the cylinder pumping flow during the valve overlap step changes with (red solid lines) and without (blue dashed lines) the valve compensator θ^*_{th} : both engine speed and base throttle position are fixed at N = 2000 RPM and θ_{th} = 20 %. (**Simulation**) 71
4.9 Comparison of relative road *RL* during the valve overlap step changes with (red solid lines) and without (blue dashed lines) the valve compensator θ^*_{th} : both engine speed and base throttle position are fixed at N = 2000 RPM and θ_{th} = 15 %. (**Experiment**) 72
4.10 Comparison of the throttle step cylinder air charge flow rate W_{cyl} of VVT turbocharged engine without compensation θ^*_{th} (blue solid lines) and VVT turbocharged engine with compensation (red dashed lines); engine speed is 2000 RPM, throttle is stepped as $\theta_{th} = 20 \rightarrow 22.5\% \rightarrow 25\% \rightarrow 22.5\% \rightarrow 20\%$. (**Simulation**) 73

5.1 Parameterized values of e and k as a function of θ_σ using Ricardo DoE data at N = 2000 and 3000 RPM. 77
5.2 Comparison between engine measurement and estimated crank angle of 50% and 90% fuel burned, θ_{CA50} and θ_{CA90} (left and right subplots, respectively), for throttle angle θ_{th} from 30% to 35% open at N = 2000 and 3000 RPM. 78
5.3 *Log p* versus *Log V* diagram of in-cylinder pressure and IMEP estimation. . 79
5.4 Combustion efficiency, η_{comb}, as a function of residual gas fraction x_{RG}. . . 80
5.5 Combustion and mean effective pressure (MEP) model structure. 81
5.6 Comparison between engine data and model simulation for E0 fuel. 81

5.7 Comparison between engine data and model simulation for E85 fuel. 82
5.8 Estimated NMEP and NSFC of the engine model for various VVT positions and combustion phase of θ_{CA50} with W_{air} = 100 kg/hr at the engine speed of 2000 RPM. 83
5.9 Correlation between combustion phase θ_{CA50} and IMEP (right) and histogram of θ_{CA50} (left) for 100 consecutive engine cycles with W_{air} = 100 kg/hr at N = 2000 RPM. 84
5.10 Standard deviation of θ_{CA50}, σ_{CA50}, as a function of residual gas fraction x_{RG}. 85
5.11 Combustion and mean effective pressure (MEP) model structure with stochastic combustion phase information. 85
5.12 Simulated and measured engine outputs for the throttle step changes with fuel E0 at N = 2500 RPM. 86
5.13 Structure of an on-board calibration scheme with adaptation of the production maps based on the engine input conditions. 87
5.14 Extremum seeking control for optimal θ_σ and VVT. 88
5.15 Simulation response in the NSFC signal of the engine model to a step change in spark timing from -15 to -20 CAD aTDC and VVT (i.e. EVC - IVO) from 0 to 10 CAD valve overlap. 90
5.16 Bode plots of the discrete low- (red dashed line) and high-pass (blue solid line) filters from the spark ES controller (top) and the VVT ES controller (bottom). 91
5.17 The simulation of ES convergence to the optimum of θ_σ and valve overlap (i.e. EVC - IVO) was tested separately and the internal signals of the ES controller such as load- and high-pass filters are presented in the second row. 94
5.18 The ES convergence to the optimum of θ_σ and the valve overlap (i.e. EVC - IVO) for two different initial values along with the feedback signal of throttle angle θ_{th} are shown on the left column and the corresponding engine performance of θ_{CA50}, x_{RG} and NSFC are plotted on the right column. . . . 95
5.19 Extremum seeking control trajectory. 96

6.1 NMEP and NSFC for various spark timing 99
6.2 NMEP and NSFC for various intake valve open timing 100
6.3 Experimental setup at the engine dynamometer. 101
6.4 Proposed rapid prototyping scheme with ES1000 VME. 103
6.5 Extremum seeking control for the optimal spark timing θ_σ. 104
6.6 Extremum seeking control test result : N = 2000 RPM, Relative load = 70%, $\Delta\theta_{\sigma,0}$ = 12 CAD, fuel = E0. 104
6.7 Extremum seeking control test result : N = 2000 RPM, Relative Load = 70%, $\Delta\theta_{\sigma,0}$ = 12 CAD, fuel = E70. 107
6.8 Extremum seeking control test result : N = 2000 RPM, Relative Load = 70%, $\Delta\theta_{\sigma,0}$ = 9 CAD, fuel = E70. 108
6.9 Extremum seeking control test result : N = 2000 RPM, Relative load = 70%, $\Delta\theta_{\sigma,0}$ = 6 CAD, fuel = E70. 109
6.10 Extremum seeking control test result : N = 2000 RPM, Relative Load = 50%, $\Delta\theta_{\sigma,0}$ = 12 CAD, A_{RL} = 3%, f_{RL} = 0.01, fuel = E85. 111

6.11 Extremum seeking control test result : N = 2000 RPM, Relative Load = 50%, $\Delta\theta_{\sigma,0}$ = 12 CAD, A_{RL} = 3%, f_{RL} = 0.05, fuel = E85. 112
6.12 Extremum seeking control test result : N = 2000 RPM, Relative Load = 50%, $\Delta\theta_{\sigma,0}$ = 12 CAD, A_{RL} = 3%, f_{RL} = 0.1, fuel = E85. 113
6.13 Extremum seeking control test result : N = 2000 RPM, Relative Load = 50%, $\Delta\theta_{\sigma,0}$ = 12 CAD, A_{RL} = 3%, f_{RL} = 0.15, fuel = E85. 114

Abstract

Current emphasis on decreasing vehicle fuel consumption and carbon dioxide (CO_2) emission from the automotive sector directs many research efforts towards two gasoline engine technologies, namely, the Homogeneous Charge Compression Ignition (HCCI) engines, and the downsized TurboCharged (TC) Spark Ignition Direct Injection (SIDI) engines with variable valve timing (VVT). In the HCCI category, many actuation strategies have been proposed with the more popular being the dual-fuel strategies and the high residual recycling. In this thesis, a heat recycling strategy is considered, specifically, a heated-air inlet HCCI engine with two intake throttles that control the cold and hot air streams. To facilitate the control analysis and development, a physics-based crank-angle resolved and a mean value models are developed for feedback controller design. We discover that the combustion duration $\Delta\theta_{comb}$ defined as the duration between the crank angle of 10% and 90% fuel burned, θ_{CA10} and θ_{CA90}, provides a universal set point for all speeds and loads for both combustion stability and fuel efficiency. Based on a novel allocation of two actuators, the hot and cold throttles, a feedback controller is designed and simulated to regulate the combustion duration $\Delta\theta_{comb}$ at a desired value and timing during load changes, addressing directly the slow response of the heat exchangers in the hot air stream. In the category of the TC SIDI engines, we address the important problem of reducing the calibration complexity when these engines are intended to run on gasoline (E0) and/or a blend of up to 85% ethanol (E85). Typically, there is variability in the optimal VVT and spark values for every blend of gasoline-ethanol. This variability burdens the calibration task for these engines with many degrees of freedom (throttle, VVT, wastegate, fuel injection timing and duration, and spark timing). We first address the transient coupling between throttle and VVT in controlling the air charge in boosted conditions. A model-based valve compensator is designed to improve the transient behavior of cylinder charge and torque during tip-ins and tip-outs with the VVT system transitions from set-points. The designed compensator is verified using both model simulation and vehicle engine test in a chassis dynamometer facility. The valve compensator can also alleviate the load disturbance induced by the VVT perturbations for the on-board calibration such as an extremum seeking (ES). An ES con-

troller tuned based on the engine model demonstrates the convergence of both spark timing θ_σ and VVT to the optimal values to achieve the best fuel efficiency. The ES algorithm for the optimal spark timing is then implemented and tested in a 4 cylinder TC SIDI engine on a dynamometer facility.

Chapter 1
Introduction

1.1 Background

The adaptation of non standard combustion, direct fuel injection and turbo-machinery continue to increase the thermal efficiency of internal combustion engines with simultaneous reductions in emissions [1]. With these advances, gasoline combustion engines continue to be an attractive option as prime movers for conventional and hybrid-electric vehicles since these engines offer outstanding drivability, fuel economy, and reliability with low combustion noise and extremely clean exhaust. Among these advanced engine technologies, two different types of engines are considered in this dissertation, a heated-air inlet homogeneous charge compression ignition (HCCI) engine and a turbocharged (TC) spark-ignition direct-injection (SIDI) engine with variable valve timing (VVT).

The engines with HCCI combustion increase combustion efficiency and achieve extremely low nitrogen oxides (NOx) emissions due to low peak in-cylinder temperatures through the lean combustion characteristics [2]. The levels of engine-out NOx is so low [3] that expensive and complex lean NOx exhaust aftertreatment technologies are not needed. Hence, HCCI strategies are prominent candidates for achieving higher fuel economy without a large cost penalty. Many automotive manufacturers (Ford, GM, Chrysler, etc.) are pursuing this HCCI approach and the US Department of Energy (DOE) has invested in R&D for these engines. A heated-air inlet HCCI engine with two intake throttles that control the cold and hot air streams, is introduced as one of the HCCI combustion strategies and the difficulties of the HCCI combustion control is addressed in this thesis. To facilitate the control analysis and development, a physics-based crank-angle resolved and a mean value model is developed for feedback controller design. We then discover that the combustion duration $\Delta\theta_{comb}$ defined as the duration between the crank angle of 10% and 90% fuel burned, θ_{CA10} and θ_{CA90}, provides a universal set point for all speeds and loads for both combustion stability and fuel efficiency. Based on a novel allocation of two actuators, the hot and cold throttles, a feedback controller is designed and simulated to regulate the

combustion duration $\Delta\theta_{comb}$ at a desired value and timing during load changes, addressing directly the slow response of the heat exchangers in the hot air stream.

Apart from the HCCI engines, the downsized TC SIDI strategy with VVT can achieve very high fuel economy at reasonable cost, hence it is expected to dominate the market in a few years. Existing vehicles in the market by many automotive manufacturers are employing the TC SIDI and VVT configuration at high-end vehicles with premium driving performance at fixed levels of fuel economy. There is considerable effort, however, to realize downsized versions where increased fuel economy will be achieved at fixed performance (drivability). The work in this thesis addresses the important problem of reducing the calibration complexity when these engines are intended to run on gasoline (E0) and/or a blend of up to 85% ethanol (E85). These engines enable the utilization of flexible gasoline-ethanol blends in vehicles called a flex-fuel vehicle (FFV). Typically, there is variability in the optimal VVT and spark values for every blend of gasoline-ethanol. This variability burdens the calibration task for these engines with many degrees of freedom (throttle, VVT, wastegate, fuel injection timing and duration, and spark timing). The transient coupling between throttle and VVT in controlling the air charge during tip-ins and tip-outs is also addressed and, then, resolved with a designed model-based valve compensator. The valve compensator can also alleviate the load disturbance induced by the VVT perturbations for the on-board calibration such as an extremum seeking (ES). An ES controller tuned based on the engine model demonstrates the convergence of both spark timing θ_σ and VVT to the optimal values to achieve the best fuel efficiency.

1.1.1 Background of HCCI Engine

Two major internal combustion engine categories that utilize different combustion concepts are the gasoline fueled spark-ignition (SI) engine, first developed by Otto in 1876, and the diesel fueled compression-ignition (CI) engine, invented by Diesel in 1892. Since then the automotive industry continuously improves the performance and fuel economy combined with low emissions at low cost.

A basic combustion principle of SI engine is based on flame propagation in engine cylinder. The flame is initiated by spark plug, a trigger to control the ignition timing, which makes the control of SI combustion feasible. The classical SI engine runs at well-mixed stoichiometric air-to-fuel ratio (AFR), which is required to maximize the efficiency of the three-way catalytic converter and, therefore, reduce tailpipe emissions. This type of engine has high power density and low combustion noise, while achieves relatively poor thermal efficiency compared to CI engine. Various modifications have been applied to

improve the thermal efficiency, for instance, stratified charge spark ignition (or gasoline direct injection) concepts have already appeared in limited editions of marketed vehicles. Although the stratified charge SI engines are not as widely adopted in the US, primarily due to cost associated with the complex exhaust gas aftertreatment necessary to meet US emission standards, their enabling technology, namely direct injections, are slowly becoming a dominant SI actuation.

The CI combustion is initiated by fuel injection inside the cylinder chamber environment hot enough to initiate combustion by auto-ignition after short delay, thus providing a controllable trigger for the ignition timing, and hence, allow the control of CI combustion. The CI engine has high thermal efficiency and hence good fuel economy due to its lean fuel combustion characteristics, high compression ratio and no-throttling in the intake system. However, very high combustion temperature mainly due to advanced start of injection timings and locally low temperature where the fuel is not fully atomized cause elevated formation of NOx and soot emissions, respectively, which requires more complex exhaust aftertreatment compared with SI engines.

In order to combine the benefits of these two conventional engine combustion concepts, the Homogeneous Charge compression Ignition (HCCI) engine concept, also called Active Thermo-Atmosphere Combustion (ATAC), was introduced in 1979 by Onishi *et al.* [4]. The combustion principle of the HCCI engine is simultaneous multiple auto-ignition in cylinder chamber with a spatially well-distributed (ideally homogeneous) air fuel mixture. A basic idea of HCCI is to employ premixed air-fuel mixture that is sufficiently lean or dilute to keep combustion temperature low, which leads to low NOx and particulate production [5]. The HCCI has been also named as Controlled Auto-Ignition (CAI) to primarily highlight the need for accurately controlled charge conditions which is harder to achieve than a direct manipulation of an actuator such as the spark discharge in SI engines and the injection timing in CI engines.

Similar to SI engine, the HCCI engine requires prepared air-fuel mixture (or premixed charge), while initiates the auto-ignition by increasing charge temperature by compression comparable with CI engine. On the other hand, the differences from SI and CI engine are that it has neither a distinct flame front nor turbulent flame propagation, and is not restricted by the mixing rate at the air fuel interface. It is known that combustion timing is determined by in-cylinder composition, pressure and temperature [6]. The combustion timing of HCCI affects engine torque generation, fuel consumption and emission.

The HCCI engine promises that it is an appropriate candidate for clean and economical passenger vehicle engine application of the future due to followings:

- High fuel efficiency, theoretically up to 50% [7], realistically up to 20% [8], due to

fuel-lean combustion, high compression ratio and fast heat release [9].

- Low engine-out NOx and soot emissions due to significantly lower peak temperatures and premixed lean mixture compared to the typical spark ignition or compression ignition engines.

Despite of these benefits, however, a commercial gasoline HCCI engine has not been realized yet since many challenges still remain in the practical application of the concept:

- No direct ignition trigger to initiate combustion, which has made combustion control very challenging particularly during transient operation.
- Small power range constrained at high load by engine damage or wear due to fast heat release and associated high in-cylinder peak pressure, and at low load by lean flammability limits [10].
- Engine damage or wear due to fast heat release and associated high peak pressure.

In addition, the auto-ignition in the HCCI engine is governed by the charge temperature history of the air-fuel mixture such that controlling the in-cylinder thermal condition is the most critical variable to achieve appropriate ignition timing and burn rate.

Various actuation methodologies for the HCCI combustion control have been proposed using variable compression ratio (VCR) in a multi-cylinder engine [11], variable valve systems (negative valve overlap (NVO) [12, 13, 14] and rebreathing lift (RBL) [15]), various fuel injection systems (Split injection [16] and dual fuel injection [17]) and so-called fast thermal management (FTM) accomplished by varying the cycle to cycle intake charge temperature by rapidly mixing hot and cold air streams [18, 19]. In the meantime, to understand and capture the engine fundamental aspects, different HCCI modeling methodologies have been discussed in previous literature, for instance, a multidimensional computational fluid dynamics (CFD) model [20], a reduced chemical kinetics model [21], a single-zone combustion model [22], a two-zone model [23], and a mixing model of two or more different methodologies [24], a physics-based mean-value HCCI engine model [15, 25], and so on. To manipulate these HCCI actuators effectively, various controller schemes such as a linear quadratic (LQ) optimal control [26, 27], a model predictive control (MCP) [28, 29], a nonlinear observer-based control [30], a proportional-integral-derivative (PID) based closed-loop combustion control [18] have been designed and demonstrated using the engine model as well as the real engine facilities.

Since the HCCI combustion timing depends more on cylinder charge temperature than on composition [31, 6], a heated-air inlet HCCI engine is introduced in this dissertation to control the cylinder temperature utilizing two intake ports throttled independently with one providing heated air and the other cold ambient air to the cylinder. The engine configuration of the heated-air inlet HCCI engine basically adopt a similar HCCI combustion

control actuator methodologies as the fast thermal management (FTM) in [18, 19]. Compared to the HCCI engine with other actuators presented above, the heated-air intake HCCI engine is also believed as an appropriate engine configuration to easily expand the HCCI upper load limit by air boosting independently from the intake and exhaust valve timing [32]. Another benefit of this engine is the heated-air HCCI engine requires relatively low additional cost for the two intake port system.

1.1.2 Background of FFV Turbocharged SIDI Engine with VVT

Various automotive technologies, such as a turbocharger, direct injection (DI) and variable valve timing (VVT), have been integrated into recent gasoline spark ignited engines to meet ever increasing demands on fuel consumption and pollutant emissions reduction. In addition, the sustainable and renewable processes of ethanol fuels and its comparable heat of combustion per unit air amount to the gasoline at the stoichiometric AFR condition encourage automotive companies in developing the flex-fuel vehicles (FFV) with a minimal modification of the existing gasoline engines. Incorporating all these technologies in gasoline engines constitutes one of the biggest automotive industry efforts for achieving both high fuel efficiency and low engine-out emissions. For this, increasing calibration efforts and more complex yet sophisticated control structures are compulsory for the accurate control of engine performance due to the variability of the optimal VVT and spark values for every blend of gasoline-ethanol and the transient coupling between actuators such as throttle, VVT and wastegate.

A turbochargers is a gas compressor used for forced induction of internal combustion engines, and the compressor is powered by a turbine which is driven by the engine's own exhaust gases. This technology allows more compressed air and fuel to be injected into the cylinders, generating extra power from each explosion. This allows manufacturers to use smaller engines (downsizing) without sacrificing engine performance. Compared with the conventional naturally aspirated (NA) and throttled gasoline engine, the specific power output from a downsized turbocharged engine can be significantly increased due to the improved volumetric efficiency. Therefore, the turbocharger allows to combine the fuel economy of the small engine with the maximum power equivalent to a bigger engine [33, 34].

Variable valve timing controls the flows of fresh air charge into the cylinders and exhaust out of them. When and how long the valves open (valve timings) and how much the valves move (valve lifts) both affect engine efficiency. Optimum timing and lift settings are different for different engine operating conditions. Traditional designs without VVT

mechanism use fixed timing and lift settings, which are a compromise between the optimum for high and low engine loads and speeds. VVT systems automatically alter timing and/or lift to the optimum settings for the different engine loads and speeds. The internally recirculated exhaust gas, controlled via variable valve train positions, improves combustion efficiency while reducing NOx emissions [35, 36, 37, 38, 39].

In the Turbocharged SIDI engine platform with VVT, the throttle, the turbocharger wastegate, and the Variable Valve Timing (VVT) system are three actuators in the air path system for the control of cylinder charge. The VVT system with variable camshafts allows flexible valve overlap, hence, enables high level of internal EGR (iEGR), which, if there is no combustion stability problem, typically reduces fuel and NOx emissions. The benefits of high level of iEGR for fuel consumption come with well known problems associated with drivability [40, 41] or control of transient air charge. In order to ensure accurate and fast delivery of the demanded air charge, appropriate control and coordination of the three actuators are required to realized the benefits of these advanced automotive technologies. Therefore, various Computer Aided Control System Design (CACSD) methods, relying on control-oriented models, have been applied to solve this problem. Literature that addresses the control of variable camshafts for the control of transient torque response, such as [40] for a system with mechanical throttle and [42, 41, 43] for one with electronic throttle, provides great insight into the coordination of the throttle and the VVT system. The fast electronic throttle is considered ,in this dissertation, as a primary control actuator associated with VVT for the engine air-path management.

Applicable models of turbocharged gasoline engines can be found in [44, 45, 46, 47]. Literature that addresses the control of wastegate in gasoline applications, such as [48, 49] for a system with mechanical throttle and [46] for one with electronic throttle, provides valuable insight into the coordination of the throttle and the turbocharger wastegate. In parallel with the air-path control loop, Air-to-Fuel Ratio (AFR) is regulated in the fuel path using feedback information from an Exhaust Gas Oxygen (EGO) sensor. Even though AFR regulation is not discussed in this dissertation, the closed-loop control of fuel injection can be aided by the indirect air-charge estimation approach developed based on the intake and exhaust valve timings and intake manifold pressure measurement in Chapter 4. Details of air charge estimation via an exhaust manifold pressure observer are discussed in [50] and [51] even though the effects of the VVT system and the associated internal gas recirculation have not been studied in [50, 51].

The Turbocharged SIDI Engine with VVT studied in this dissertation is also capable of running on both gasoline (E0) and a blend of up to 85% ethanol (E85). The use of ethanol fuels can reduce the consumption of non-renewable fossil fuels. In addition, the flex-fuel

vehicle (FFV) engine has the potential of efficiency improvements of 3-6% with E85 over the optimized gasoline engine at part loads mainly due to reduction in heat rejection and increased dilution tolerance [52]. At full loads, a potential of 13-15% increase in engine specific output, defined as the engine power per unit engine displacement, is available with E85 enabled by the antiknock properties of the ethanol blends and an increase in volumetric and indicated efficiencies. These benefits, however, can be achieved only by the significant increase in engine calibration efforts, which will be addressed in this dissertation.

1.2 Engine System Configuration

The system configuration and measurement sensors of the two different gasoline engines addressed in this dissertation are introduced in this section: first, a single cylinder heated air inlet HCCI engine and, second, a 4 cylinder turbocharged spark ignition (SI) direct injection (DI) engine with variable valve timing (VVT).

1.2.1 Single Cylinder Heated-Air Inlet HCCI Engine

A single cylinder engine was used in a dynamometer cell for both steady-state and transient test data acquisition. The engine specification is summarized in Table 1.1. The dynamometer engine has been designed to operate in both SI and HCCI combustion modes although the SI mode and mode transition is not covered in this dissertation. This mode change is accomplished by the use of a roller finger follower cam profile switching (CPS) mechanism on the intake and exhaust camshafts, proposed to control both valve overlap and effective compression ratio [7]. For instance, in HCCI combustion mode, negative valve overlap, widely used for trapping residual burned gas within the cylinder to enable controlled HCCI, can reduce the requirement on intake heating.

In the HCCI mode, two intake ports are independently throttled, with one port providing heated air and the other cold ambient air to the cylinder. An electric, flow-through convective heater was used as a primary air-charge heat source. Further, plenum band heaters were used to maintain a sufficient supply of heated air charge to the engine. In the vehicle application the electric heaters would be replaced by heat-exchangers utilizing (recycling) the exhaust gas heat. A bleed throttle was used to maintain hot air circulation through the intake system to prevent overheating. The hardware configuration is shown in Fig. 1.1. The intake and exhaust runners were all fitted with pressure transducers and thermocouples. The instrumentation included crank and cam position sensors. All sensor

Table 1.1 Specifications for a single cylinder heated-air HCCI engine [53]

Description	Value
Cylinder total volume	704.34 mm^3
Cylinder displacement volume	658.0 mm^3
Combustion chamber clearance volume	46.34 mm^3
Compression ratio	15.2:1
Cylinder bore	89 mm
Piston stroke	105.8 mm

signals were processed and filtered.

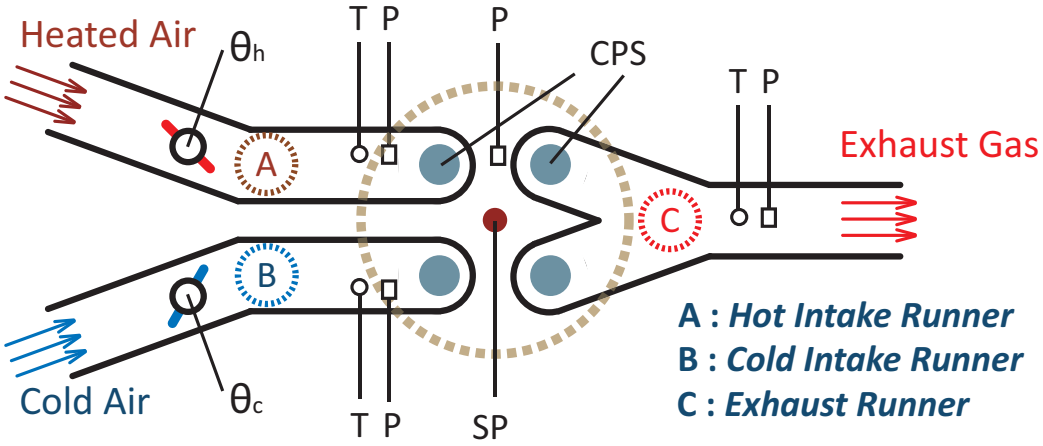

Figure 1.1 Schematic of the HCCI engine setup : T, P, V, SP and CPS refer to a temperature sensor, a pressure sensor, a valve actuator, spark timing control and cam profile switching control, respectively [54].

1.2.2 Turbocharged SIDI Engine with VVT

The engine configuration of the turbocharged gasoline spark ignition direct injection (SIDI) engine with variable valve timing is shown in Fig. 1.2. Ambient air enters the engine system and a hot-film mass flow sensor measures the intake air flow rate. Next, the air passes through the compressor side of the turbocharger and then the intercooler, which results in a boost pressure that is higher than the ambient pressure. After the air passes through the throttle, it accumulates in the intake manifold and enters the cylinder when the intake valves open. Depending on the intake and exhaust valve timings, a fraction of the exhaust gas from the current cycle remains in the cylinders and influences the combustion behavior

during the next cycle. In the mean time, the injectors spray a demanded amount of fuel directly into the combustion chamber by controlling the fuel rail pressure and injection duration. The cylinder charge mixture is then ignited by spark plug to achieve the appropriate combustion phase. On the exhaust side, part of the exhaust gas exits via the turbine and generates the power to drive the compressor, while the rest of it passes through the wastegate. The exhaust gas finally returns back to the environment after being treated in the catalyst.

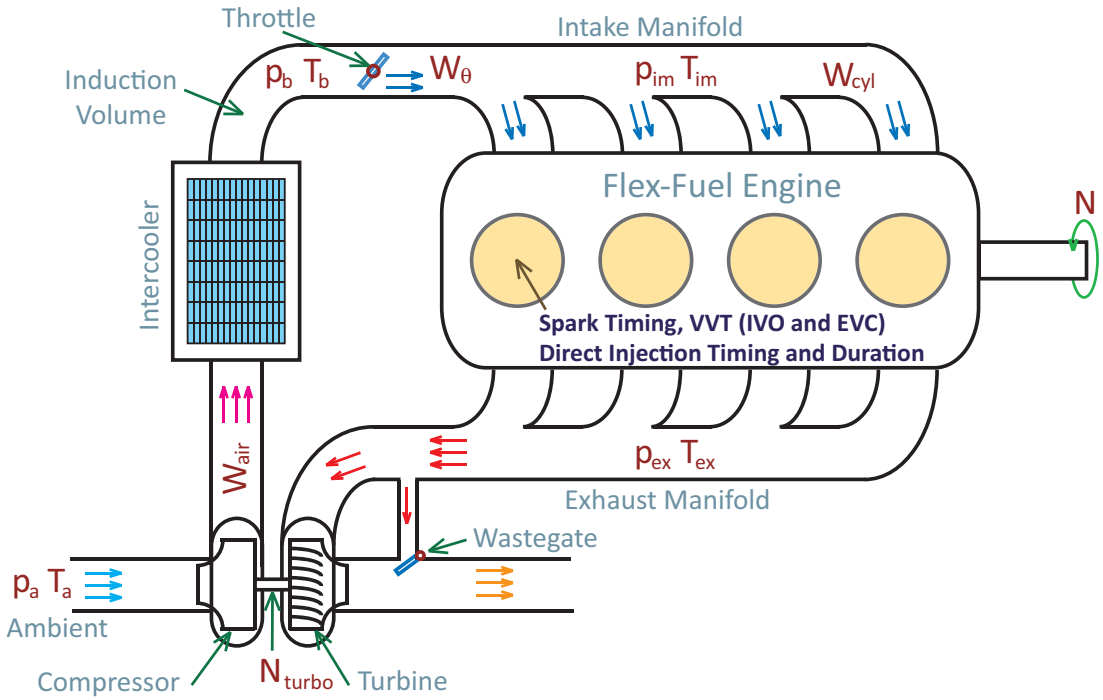

Figure 1.2 Configuration of a turbocharged (TC) gasoline spark ignition direct injection (SIDI) engine equipped with variable intake and exhaust camshafts.

The engine has been designed to run on gasoline (E0) and a blend of up to 85% ethanol (E85), which introduces an additional calibration effort in the current engine control unit (ECU). Current engine controllers in the ECU adjust the spark timing, fuel injection timing and duration, variable valve timing and turbocharger wastegate duty cycle in a feedforward manner. In-cylinder pressure sensors are used mainly to quantify the combustion phases, for instance, the crank angle of 50% fuel burned θ_{CA50} and the combustion duration defined by the crank angle between spark timing θ_σ and 90% fuel burned θ_{CA90}. An electronic throttle control (ETC) severs the mechanical link between the accelerator pedal and the throttle for vehicle traction control. The ECU determines the required throttle position by calculations from sensor measurements such as an accelerator pedal position, engine speed, vehicle speed etc.

1.3 Overview

The schematic diagram and model structure of a experimental dynamometer HCCI engine used for the data acquisition during both steady state and transient conditions is described in Chapter 2. Based on the steady-state dynamometer test data, a crank-angle based model is, then, developed by tuning all parameters in sub-models. For instance, discharge coefficients of flow rate through throttles and valves, heat transfer coefficient through the exhaust runner and various coefficients of combustion timing model (i.e. coefficients in Arrhenius integral for start of combustion timing θ_{SOC} and correlation equations between the crank angle of 02% fuel burned θ_{CA02} and 50% fuel burned θ_{CA50} and so on) are determined using either least square (LS) method or MATLAB optimization routines, so called *DIRECT* and *fminunc*.

The crank-angle based HCCI model developed is, then, validated with steady state and transient data. The HCCI engine performance variables such as indicated mean effective pressure (IMEP), air-to-fuel ratio (AFR), crank angle of 02% fuel burned θ_{CA02} and 50% fuel burned θ_{CA50}, and exhaust runner temperature T_{ex} are used for validation purpose in the steady state test, while IMEP, crank angle of 10% fuel burned θ_{CA10} and 50% fuel burned θ_{CA50}, cylinder peak pressure p_{peak} and location of cylinder peak pressure $Locp_{peak}$ for the transient test validation. First of all, for the steady state validation, data from the HCCI engine operating range from IMEP of approximately 1 bar through 5 bar at three different engine speed of 1000, 1500 and 2500 rpm are used. We include all the test data sets up to IMEP covariance of 10, which is close to unstable combustion. Next, the transient test data are compared with the model prediction in the step changes of three different engine inputs, those are, fuel injection rate, heated air inlet throttle angle and cold air inlet throttle angle, respectively. It can be observed that the HCCI model is capable in capturing proper tendency for both steady state and transient test.

In Chapter 3, we introduce a simple statistical physics based HCCI mean-value model (MVM) including an engine cycle delay and the model is validated with both steady-state and transient dynamometer test data. We then investigate an appropriate control objective, which represents engine performance, and find that the combustion duration, $\Delta\theta_{comb}$, might be a surrogate control objective for both combustion stability and fuel efficiency. Since the HCCI engine has two actuators (cold and hot throttles) and one control objective $\Delta\theta_{comb}$, the allocation of actuators is performed based on the assumption that the heated inlet air temperature varies slowly through a heat exchanger dynamics and the two actuators can be decoupled such that cold throttle manages slow hot inlet air temperature changes with a feedforward controller while hot throttle mainly manages the load disturbances using

cycle-to-cycle combustion duration measurement.

Based on the allocation of two actuators, a model based controller is designed to manage the hot throttle actuator to regulate the combustion duration at 7.5 CAD during load transients. The feedforward compensator and PI feedback controller together shows good regulation responses of $\Delta\theta_{comb}$ to achieve higher IMEP and smaller covariance of IMEP. A simple heat exchanger with the effectiveness of 0.47 and a lag is implemented and, from the simulation results, it can be verified that the decoupling of two actuators is appropriate.

Modification of the nonlinear mean value model of a turbocharged spark ignition flex-fuel engine equipped with variable camshafts and electronic throttle is presented in Chapter 4. Two static valve overlap schedules are derived for "best torque" and "best internal exhaust gas recirculation (iEGR)" requirements. To improve the transient behaviors of the cylinder charge air flow rate (or torque) during throttle step changes, the valve compensator is introduced in the air-path control loop. To reduce the disturbance of the VVT change on cylinder charge flow rate, a nonlinear model-based valve compensator is designed in addition to the base throttle controller for the turbocharged engine. This compensator improves the transient behavior of cylinder charge flow rate, especially at low load. The valve compensator is tested using both a mean-value model and a vehicle engine. The valve compensator showed a considerable improvement in the regulation of cylinder charge flow rate W_{cyl} while the valve overlap v changes.

The proposed valve compensator is originally designed to be used to conduct an on-board calibration such as an extremum seeking (ES) control algorithm. As more control parameters are introduced by the turbocharger, variable valve timing and direct fuel injection, an increased amount of calibration efforts are required to determine the optimal control set-points for engine performance and emissions. To supplement this calibration burden and take into account of all the influencing factors such as fuel properties and engine aging, the on-board calibration scheme searches the optimal VVT and spark ignition through the evaluation of engine performances while VVT and spark timing are perturbed. The valve compensator can moderate the cylinder charge disturbance and/or torque disturbance from this VVT perturbation.

A phenomenological combustion model which accounts for the cyclic combustion variability with the combustion phase θ_{CA50} variance as a function of the iEGR in Chapter 5. The mean effective pressure model is then determined based on θ_{CA50} and intake and exhaust manifold pressure measurements. Along with the θ_{CA50} variation the combustion efficiency is also modeled as a function of iEGR level. The engine model can demonstrate the optimal engine operating condition with respect to spark timing and VVT in addition to the realistic noise level of important engine performance outputs such as θ_{CA50}, mean

effective pressure (MEP) and specific fuel consumption (SFC).

The developed engine model allows us to tune and test the on-line optimization scheme such as the extremum seeking controller to search the optimum of engine inputs for the idle and cruise conditions. The ES algorithm can be used to optimize any other operating conditions with long residence time since the current ES algorithm will converge and is enabled only at steady-state driving conditions. The on-line optimization scheme can alleviate the heavy calibration burden required especially for the recent engines with many control actuators. The designed extremum seeking algorithm shows that both spark timing θ_σ and VVT values can converge to the optimum within 60 seconds even though this convergence rate may be engine and vehicle specific.

In Chapter 6, we present an ES control algorithm which has been tested in a dynamometer engine. NMEP and NSFC characteristics have been analyzed based on different spark timing and variable valve timing. Due to small and negligible NSFC changes for IVO changes, the ES control is tested only for spark timing. Implemented ES control algorithm is modified with two additional function blocks, saturation and dead-zone, which guarantee stabilized ES controller dynamics. Also, a convergence detection logic is introduced to determine whether the current spark timing is the optimum or not.

Two different types of load inputs are applied during ES algorithm test in the dynamometer engine, fixed and transient load inputs. The transient load input is realized with sinusoidal load commands with various amplitudes and frequencies. It takes approximately 20 seconds to search the optimal spark timing under both the fixed and transient load conditions. For the transient load inputs, the current ES algorithm is capable to determine the optimum up to the frequency of $f_{RL} = 0.1$, while the convergence detection logic is not capable to determine the optimum with a higher frequency, $f_{RL} = 0.15$. Therefore, it might be necessary to modify the logic to be implemented in a real vehicle if a normal driving profile often changes with a high frequency in a steady-state maneuver.

The schematic overview of this dissertation is shown in Fig. 1.3.

1.4 Contributions

The specific novel and innovative findings in this dissertation are:

- Developed the first crank-angle based model for a single cylinder heated air inlet HCCI engine with two intake throttles that control the cold and hot air streams [53]. The model can capture the critical engine performance variables such as IMEP, AFR, θ_{CA02} and θ_{CA50}, but also other engine variables, cylinder pressure and temperature traces on the crank angle basis.

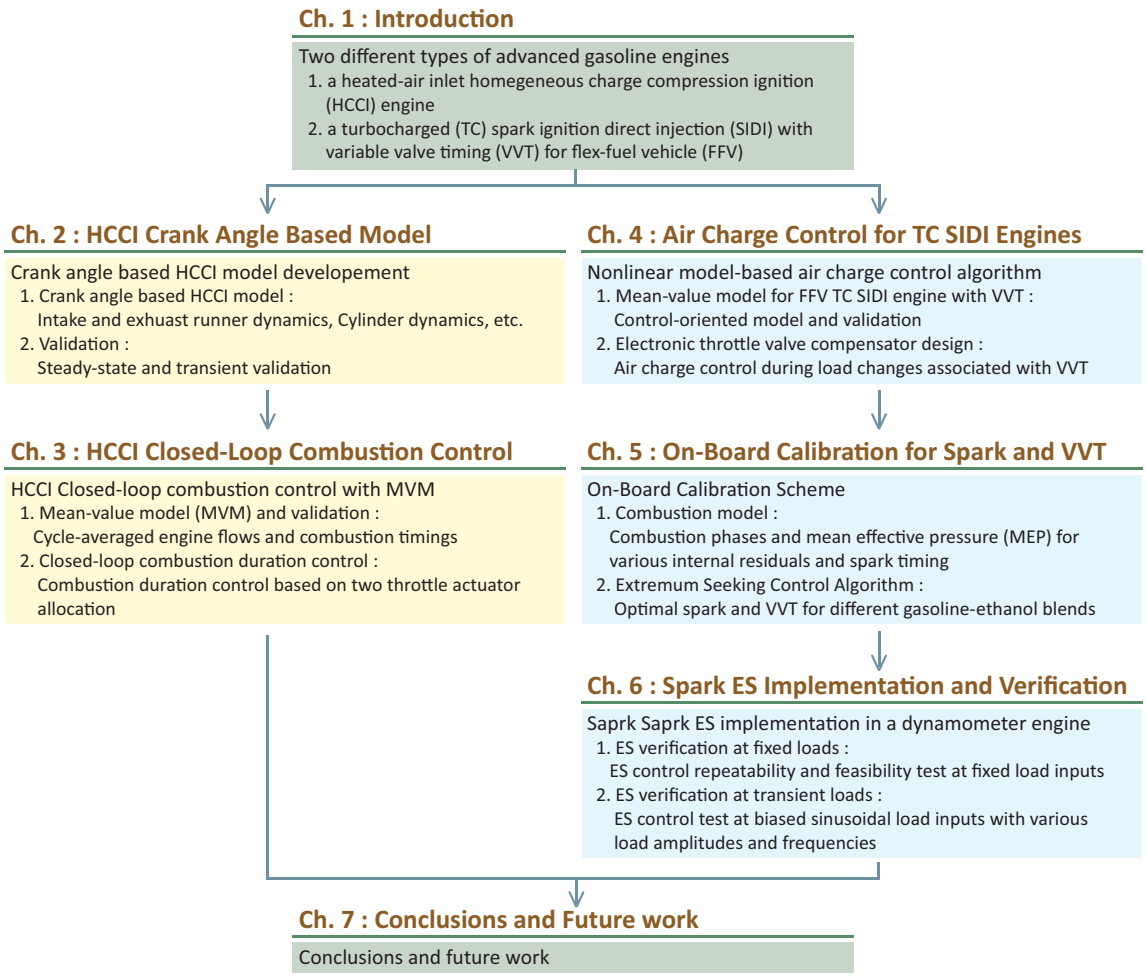

Figure 1.3 Schematic overview of the dissertation.

- Developed and validated a simple HCCI mean value model (MVM) [54] which led to a novel control set-point. Specifically, the combustion duration $\Delta\theta_{comb}$ is found to be an appropriate proxy to represent both fuel efficiency and combustion stability. A model based controller is designed based on controller allocation and simulated in both the HCCI MVM and the crank-angle based model to demonstrate the combustion duration $\Delta\theta_{comb}$ regulation.
- Modified the mean-value model in [47] for a 4 cylinder turbocharged (TC) spark ignition direct injection (SIDI) engine with variable valve timing (VVT) to capture the coupling between throttle and VVT settings in the cylinder charge [55]. A nonlinear feedforward throttle compensator is employed to improve the transient response of cylinder charge during load changes. The algorithm is also implemented and verified in a vehicle engine on a chassis dynamometer facility.
- Developed a reduced-order SI combustion model to predict the effect of internal residuals and spark timing in the combustion efficiency and in the cycle-to-cycle combustion variation [56]. An extremum seeking (ES) controller is, then, designed

to optimize and/or update VVT position and spark timing to reduce the significant calibration effort associated with various fuel blends.

- Verified the ES control algorithm test in a engine dynamometer facility for spark timing for various engine operating conditions, in specific, different engine speeds and loads. Also, the feasibility and repeatability of the ES algorithm were investigated with two different types of load inputs, namely fixed and transient load inputs. The transient load input has been realized with biased sinusoidal load commands with various amplitudes and frequencies.

Chapter 2
HCCI Crank Angle Based Model

2.1 Introduction

To design and optimize a controller for HCCI combustion, a model of the system with accurate prediction of combustion phasing is necessary. Many methods have been proposed to develop a model of HCCI combustion as close as possible to real engines. Such models include one-zone combustion model defined by chemical kinetic mechanism [57], multi-zone models [58], and multi-dimensional CFD models [59]. The approaches comprise so-called open system first law analysis with chemical concentration states and ignition correlation cycle based modeling. The other set of models are intended for control development and they attempt to capture only the part of the gas exchange and combustion behavior that is relevant to HCCI engine control design [25, 60, 22, 15].

This chapter focuses on developing a crank-angle based control oriented model for single cylinder heated air HCCI engine with two intake throttles that control the cold and hot air streams. The experimental work is dedicated to testing such a single cylinder engine, assisting to investigate important issues with HCCI operation: control, operating range, fuel benefit, and emissions. Different from typical mean value models developed for single cylinder engines, the present model not only simulates cycle average engine variables, such as combustion burn rate, indicated mean effective pressure (IMEP) and emissions, but it also calculates engine variables such as cylinder pressure and temperature on the crank angle basis. It makes the expansion of the model into a multi cylinder HCCI engine model to account for true rotational dynamics and manifold dynamics less complex. To validate the model, a detailed mapping plan was developed and data collected in a dynamometer test cell for both steady state and transient conditions.

The crank-angle based HCCI engine model combines the manifold filling dynamics (including the intake and exhaust manifold model in 2.4.1 and 2.4.2) with the cylinder dynamics (including the Woschni heat transfer to consider the heat transfer through the cylinder parts in 2.5.3 and the Arrhenius integral to compute the start of combustion θSOC

in 2.5.5). The crank-angle based model was validated with more than 200 data sets, which cover three different engine speeds (1000, 1500 and 2500 RPM) and various loads and throttle angles. We first present the model prediction at steady state. Note here that the steady state data sets were used for the parameter calibration of each sub-model in the previous chapter. For example, the air-to-fuel ratio (AFR), manifold pressure and temperature measurements along with reported throttle angles and fuel flows were used to calibrate the flow through the throttles and valves. Similarly, calculated flows and measured temperatures were used to calculate the heat transfer coefficients. In this chapter, we compare the overall model predictions, and evaluate how individual error in the sub-models propagates through to the overall input-output model prediction. We then utilize new data sets from the transient HCCI operation to evaluate the overall model prediction capability.

2.2 Model Structure

The model presented here includes a crank-angle based parameterization of HCCI behavior. The dynamical behavior of the crank angle based model is associated with (i) states representing the mass and pressure (or temperature) in the intake and exhaust runners as well as the engine cylinder and (ii) the auto-ignition timing also known as as the start of combustion (SOC) and the crank angle of 50% fuel burned θ_{CA50}. The schematic diagram and notation for the crank-angle based HCCI model is shown in Fig. 2.1. Variables associated with ambient conditions are denoted by subscript 0, while the variables related to heated air conditions by subscript h. The cold and hot intake runners are referred to as volume 1 and 1h, the exhaust runner volume as volume 2. Flows are depicted according to the notation W_{xy} where x and y are the upstream and downstream of the flow. Heated air flow is described by an additional subscript h as W_{xyh}.

The HCCI engine model structure is explained using two subcategories, one is for intake and exhaust runner dynamics and the other for cylinder dynamics. Fig. 2.2 shows the integrated model structure developed for the single cylinder crank-angle based HCCI engine.

2.3 Flow through Throttles and Valves

This section presents the model for the flow through the throttles and valves. In general, flow W_{ij} through a restriction on flow area A_r is caused by pressure difference between the upstream location i and downstream location j of it. The ideal flow is determined based on

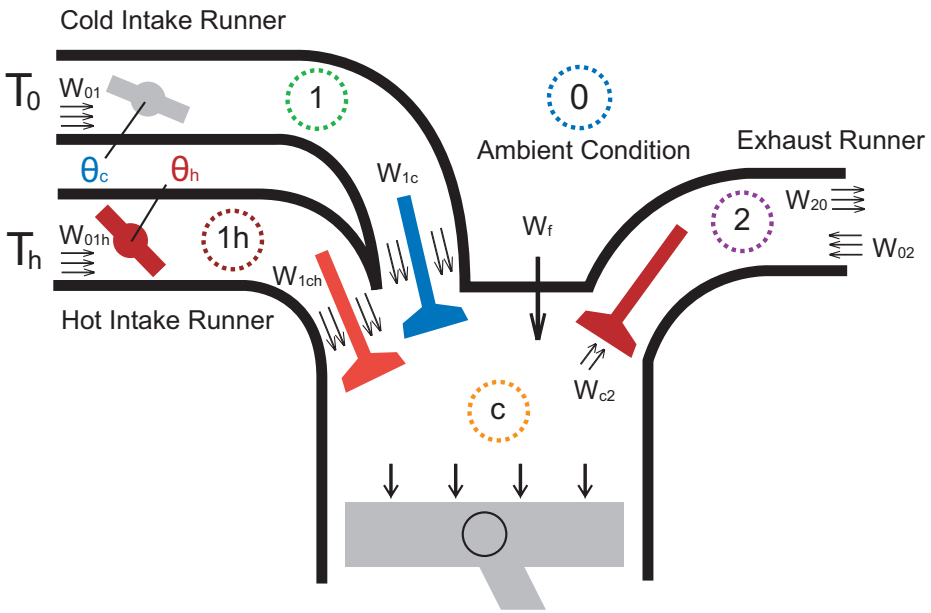

Figure 2.1 Schematic diagram and notation for the crank-angle based HCCI model.

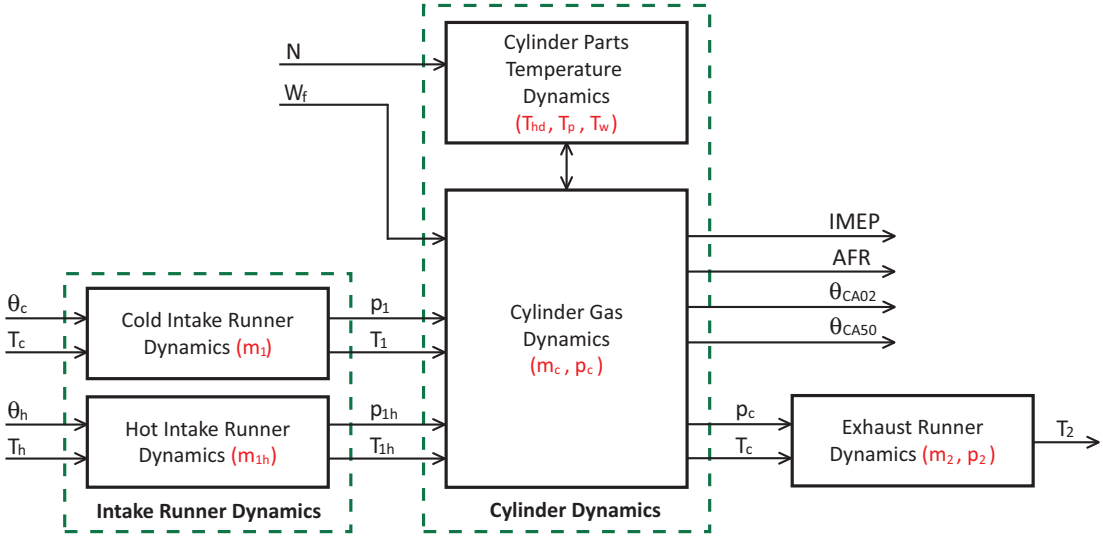

Figure 2.2 Single cylinder HCCI engine model structure.

the ideal gas law, steady flow energy equation and isentropic relation. Moreover, for a real flow, the departure from the ideal flow is corrected by introducing the discharge coefficient,

C_D (see [61], Appendix C):

$$W_{ij} = C_D A_r \frac{p_i}{\sqrt{RT_i}} \begin{cases} \gamma^{1/2} \left(\frac{2}{\gamma+1}\right)^{\frac{\gamma+1}{2(\gamma-1)}} & 0 \le \frac{p_j}{p_i} \le c_r \\ \left(\frac{p_j}{p_i}\right)^{\frac{1}{\gamma}} \sqrt{\frac{2\gamma}{\gamma-1}\left(1-\left(\frac{p_j}{p_i}\right)^{\frac{\gamma-1}{\gamma}}\right)} & c_r < \frac{p_j}{p_i} \le 1 \\ 0 & \text{otherwise.} \end{cases} \tag{2.1}$$

The critical pressure ratio $c_r = \left(\frac{2}{\gamma+1}\right)^{\frac{\gamma}{\gamma-1}}$ makes a distinction between laminar and chocked flow. The thermodynamic properties such as universal gas constant, R, specific heat ratio, γ, are assumed to be constant in (2.1). Therefore, the critical pressure ratio is also constant with $c_r = 0.5283$.

2.3.1 Discharge Coefficient and Reference Flow Area of Throttle Flow

For the throttle flow, the values of the discharge coefficient C_D according to different cold throttle angles, θ_c, are determined by a 4th order polynomial equation:

$$C_D(\theta_c) = a_{0,c} + a_{1,c}\theta_c + a_{2,c}\theta_c^2 + a_{3,c}\theta_c^3 + a_{4,c}\theta_c^4, \tag{2.2}$$

where θ_c is in the range between 0 (completely closed throttle) and 82 degrees (wide open throttle). For the hot throttle flow, on the other hand, a 6th order polynomial equation is used to establish the discharge coefficient $C_D(\theta_h)$:

$$C_D(\theta_h) = a_{0,h} + a_{1,h}\theta_h + a_{2,h}\theta_h^2 + a_{3,h}\theta_h^3 + a_{4,h}\theta_h^4 + a_{5,h}\theta_h^5 + a_{6,h}\theta_h^6, \tag{2.3}$$

where θ_c is in the range between 0 (completely closed throttle, 0%) and 82 degrees (wide open throttle, 100%). All 12 coefficients (i.e. 5 from the cold throttle discharge coefficient and 7 from the hot throttle discharge coefficient) were calibrated using the air to fuel ratio (AFR) values from the steady-state test data. In specific, first, the coefficients $a_{k,h}$, where $k = 0, \cdots, 6$ for the hot throttle flow were determined by the hot throttle sweep test data, in which the cold throttle was completely closed. With these calibrated coefficients, the coefficients $a_{k,h}$, where $k = 0, \cdots, 4$ in the cold throttle flows were, then, obtained using the cold throttle sweep test data, in which the hot throttle was wide open. In Table 2.1 and Fig. 2.3, all calibrated coefficients and the corresponding C_D plots for both cold and hot throttle flows are shown, respectively. Note that the flow area of A_r = 0.0019635 m^2 is used for

both hot and cold throttles.

Parameter	$C_D(\theta_c)$	$C_D(\theta_h)$
a_0	5.2000×10^{-3}	2.9543×10^{-3}
a_1	1.1466×10^{-4}	2.2856×10^{-4}
a_2	5.7759×10^{-5}	1.6569×10^{-4}
a_3	-7.9623×10^{-7}	7.2576×10^{-6}
a_4	3.0098×10^{-9}	1.7930×10^{-7}
a_5	-	1.7246×10^{-9}
a_6	-	4.9991×10^{-12}

Table 2.1 Determined parameters in the discharge coefficient equations for cold and hot throttles.

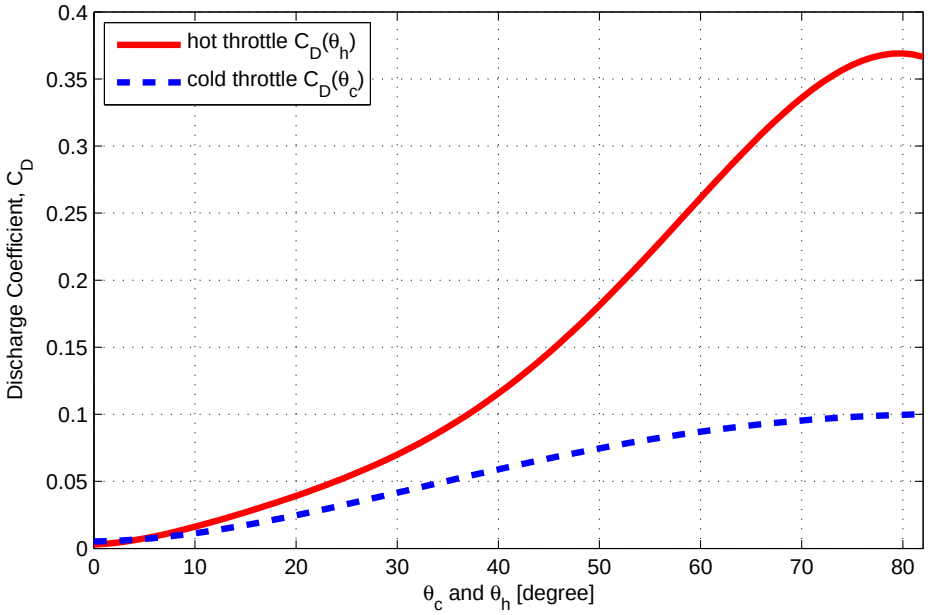

Figure 2.3 Discharge coefficients based on the cold and hot throttle angles.

2.3.2 Discharge Coefficient and Reference Flow Area of Valve Flow

Cold intake valve lift $\mathrm{IVL_c}$ determined based on the cold intake valve cam profile was computed as following:

$$IVL_c(\bar{\theta}_c) = \begin{cases} c_{0,c} + c_{1,c}\bar{\theta}_c + c_{2,c}\bar{\theta}_c^2 + c_{3,c}\bar{\theta}_c^3 + c_{4,c}\bar{\theta}_c^4 + c_{5,c}\bar{\theta}_c^5 + c_{6,c}\bar{\theta}_c^6 \\ \qquad\qquad 0 \le \bar{\theta}_c \le IVC_c - IVO_c, \\ 0 \qquad\qquad \text{otherwise,} \end{cases} \tag{2.4}$$

where $\bar{\theta}_c = \theta - IVO_c$ and θ is the engine crank angle. Similarly, for the hot intake valve lift $\mathrm{IVL_h}$ and exhaust valve lift EVL, the terms $\bar{\theta}_c$, $\mathrm{IVO_c}$ and $\mathrm{IVC_c}$ in (2.4) can be substituted by $\bar{\theta}_h$, $\mathrm{IVO_h}$ and $\mathrm{IVC_h}$ for $\mathrm{IVL_h}$, and $\bar{\theta}_e$, EVO and EVC for EVL, respectively.

Cold intake valve discharge coefficient C_D and the reference area $A_{r,c}$ characterized by the valve design was calculated by:

$$C_D A_{r,c}(IVL_c) = e_{0,c} + e_{1,c}IVL_c + e_{2,c}IVL_c^2 + e_{3,c}IVL_c^3 + e_{4,c}IVL_c^4. \tag{2.5}$$

The formulations for the case of the hot intake valve $C_D A_{r,h}$ and exhaust valve $C_D A_{r,e}$ were established by substituting the terms $\mathrm{IVL_c}$ in (2.5) with $\mathrm{IVL_h}$ and EVL, respectively. All the coefficients in (2.4) and (2.5) were provided from Ford and, hence, are not in the public domain. Fig. 2.4 shows the intake and exhaust valve lift and corresponding discharge coefficient and reference flow area.

2.4 Intake and Exhaust Runner Dynamics

In this section, sub-models for hot and cold intake runner and exhaust runner are represented based on the flow model in Sec. 2.3. First, cold and hot intake runner filling dynamics are described with a state of mass, m_1 and m_{1h}, respectively, based on isothermal condition. Exhaust runner dynamics is, on the other hand, modeled with two states, that are, exhaust runner mass m_2 and pressure p_2, including a simple heat transfer model.

2.4.1 Intake Runner Dynamics

In the hot and cold intake runners, one state for each runner is determined using an ordinary differential equation to describe the spatially averaged isothermal runner filling dynamics. The mass conservation law leads to the following state equation for the cold intake runner

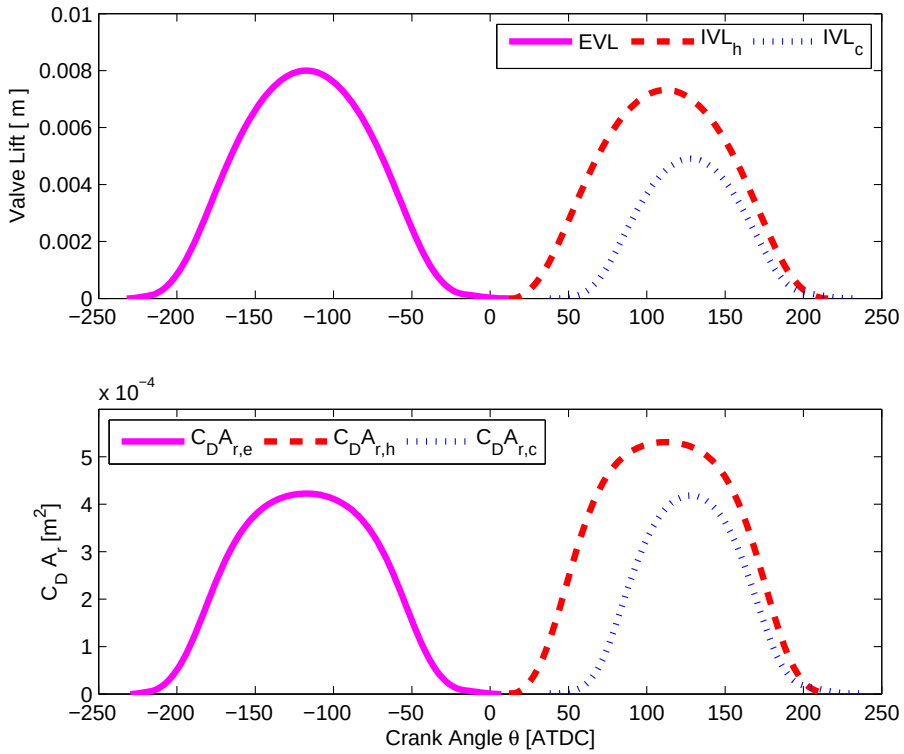

Figure 2.4 Intake and exhaust valve lift ($\mathrm{IVL_c}$, $\mathrm{IVL_h}$ and EVL) and corresponding discharge coefficient and reference flow area ($C_D A_{r,c}$, $C_D A_{r,h}$ and $C_D A_{r,e}$).

mass m_1:

$$\frac{dm_1}{dt} = W_{01} - W_{10} - (W_{1c} - W_{c1})\,. \tag{2.6}$$

With the information of mass state m_1 and assuming that the cold intake runner gas temperature is equal to the ambient temperature $T_1 = T_0$, the pressure in the cold intake runner p_1 can be simply determined using the ideal gas law $p_1 = m_1 R T_1 / V_1$. Similarly, the hot intake runner dynamics are represented with

$$\frac{dm_{1h}}{dt} = W_{01h} - W_{10h} - (W_{1ch} - W_{c1h})\,, \tag{2.7}$$

hence, the hot intake runner pressure $p_{1h} = m_{1h} R T_{1h} / V_{1h}$, where $T_{1h} = T_h$. Note that a thermocouple was located in the hot intake runner, close to the hot intake valve, to measure the hot intake runner temperature T_{1h}. The hot plenum heater is controlled to regulate T_{1h} to specified values based on the intent of the experiment.

2.4.2 Exhaust Runner Dynamics

In the exhaust runner, two states offer a spatially averaged, lumped parameter model of the temporal evolution of mass stored and pressure. The mass conservation law is used to calculate a mass rate in the runner and the energy conservation law with a certain amount of heat transfer through the exhaust runner wall determines the pressure inside the exhaust runner:

$$\frac{dm_2}{dt} = W_{c2} - W_{2c} - (W_{20} - W_{02}) \tag{2.8}$$

$$\frac{dp_2}{dt} = \frac{\gamma R}{V_2}\left[W_{c2}T_c - W_{2c}T_2 - (W_{20}T_2 - W_{02}T_0)\right] - \frac{R}{c_v V_2}A_2h_2\left(T_2 - T_0\right) \tag{2.9}$$

With the information of two states, the temperature in a exhaust runner, T_2, can be simply determined using $T_2 = p_2V_2/m_2R$. Instead of two heat transfer coefficients, for instance, one for the heat transfer between exhaust runner gas and the exhaust runner wall temperature and the other for the heat transfer between exhaust runner wall and ambient temperature, one inclusive coefficient A_2h_2 between exhaust runner gas and ambient temperature is designed to predict the exhaust runner temperature using:

$$A_2h_2 = f(m_{fuel}, N), \tag{2.10}$$

where m_{fuel} is the injected fuel amount per each cycle and N indicates the engine speed. In general, for a fixed engine speed, the overall heat transfer coefficient becomes smaller as the injected fuel amount increases. On the other hand, faster engine speed induces bigger heat transfer coefficient at a fixed injected fuel amount per each cycle [62]. Fig. 2.5 shows the regressed exhaust heat transfer coefficient A_2h_2 as a function of injected fuel per each cycle ,m_{fuel}, and engine speed, N.

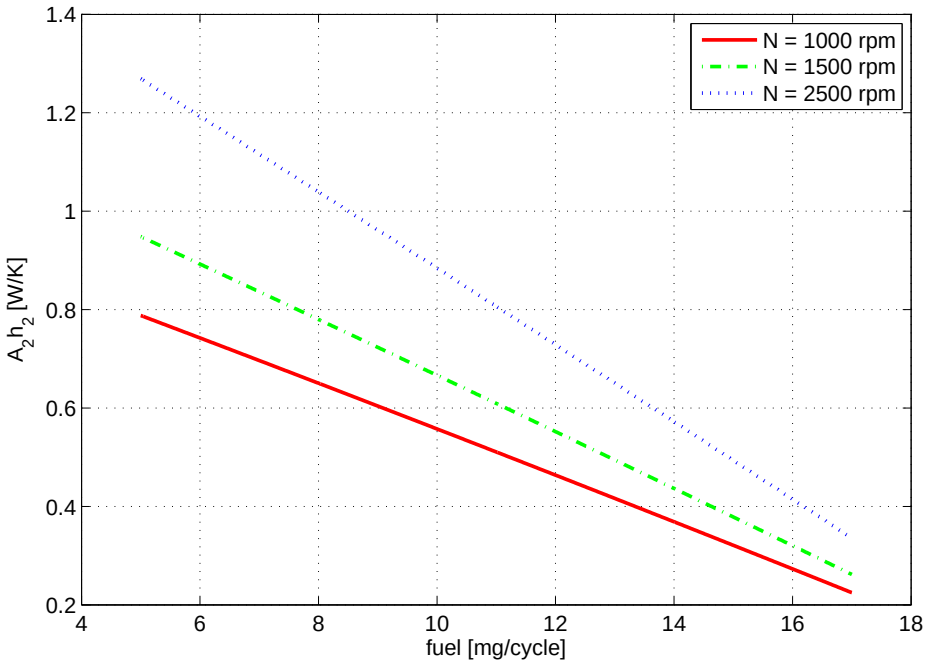

Figure 2.5 Representation of regressed total exhaust heat transfer coefficient $(A_2h_2)_{total}$ [W/K] as a function of injected fuel per each cycle m_{fuel} [mg/cycle], and engine speed N [RPM].

2.5 Cylinder Dynamics

2.5.1 Cylinder Gas Dynamics

To describe the HCCI engine cylinder gas dynamics, two ordinary differential equations for the cylinder mass m_c in (2.11) and the pressure p_c in (2.12) were derived as following:

$$\frac{dm_c}{dt} = W_{1c} - W_{c1} + W_{1ch} - W_{c1h} + W_{2c} - W_{c2} + W_{fuel}, \tag{2.11}$$

$$\frac{dp_c}{dt} = \frac{\gamma}{V_c}\left(W_{tot}T_{tot}R - p_c\dot{V}_c\right) + \frac{\gamma_c - 1}{V_c}\dot{q}_c, \tag{2.12}$$

where

$$\begin{aligned} W_{tot}T_{tot} &= W_{1c}T_1 - W_{c1}T_c + W_{1ch}T_{1h} - W_{c1h}T_c + W_{2c}T_2 - W_{c2}T_c, \\ \dot{q}_c &= Q_{LH}\dot{m}_b - h_c\left(A_p\left(T_c - T_{hd}\right) + A_p\left(T_c - T_p\right) + A_b\left(T_c - T_w\right)\right), \end{aligned}$$

where V_c and $\dot{V}_c$ indicate the cylinder volume and volume changes, respectively, which can be determined by the engine speed N and a crank angle θ. The variables A_p and A_b represent the instantaneous cylinder cross section area and wall surface area. The cylinder temperature, T_c, is computed using the ideal gas low $T_c = p_cV_c/m_cR$. The average of

injected fuel flow rate into the cylinder W_{fuel} refers to the fuel flow rate from the start of injection (SOI) to the end of injection (EOI) timing. Note $Q_{LH} = 44.0 \times 10^6$ J/kg is used for the gasoline lower heating value. The terms for the flows W_{ij} were computed based on 2.1 in Sec. 2.3. All other variables such as cylinder part temperatures (i.e. T_{hd} for cylinder head, T_p for piston and T_w for cylinder wall), the heat transfer coefficient h_c and the fuel mass burned rate $\dot{m}_b$ are introduced in Sec. 2.5.2 through 2.5.4.

2.5.2 Cylinder Part Temperatures

To compute the heat transfer in (2.12), a model of the evaluation of the cylinder head temperature T_{hd} in (2.13), piston temperature T_p in (2.14) and wall temperature T_w in (2.15) are used as follows:

$$\frac{dT_{hd}}{dt} = \frac{1}{c_{p,hd}m_{hd}}\left[A_{hd}h_{hd}\left(T_{cool} - T_{hd}\right) + A_{hd}h_c\left(T_c - T_{hd}\right)\right], \tag{2.13}$$

$$\frac{dT_p}{dt} = \frac{1}{c_{p,p}m_p}\left[A_p h_p\left(T_{oil} - T_p\right) + A_p h_c\left(T_c - T_p\right)\right], \tag{2.14}$$

$$\frac{dT_w}{dt} = \frac{1}{c_{p,w}m_w}\left[A_w h_w\left(T_{oil} - T_w\right) + A_b h_c\left(T_c - T_w\right)\right], \tag{2.15}$$

where c_p and m are specific heat and mass for each part, and A indicates the surface where the heat transfer occurs. The subscript hd, p and w were added to denote the cylinder head, piston and wall, respectively. We assume that the heat transfer coefficient between cylinder part and engine coolant (or oil) is function of engine speed. Note that a fixed engine coolant temperature T_{cool} = 367 K and oil temperature of T_{oil} = 367 K are used throughout all the simulations. The heat transfer coefficient between the cylinder gas and cylinder parts h_c was derived in the next section.

2.5.3 Woschni Heat Transfer

Using the correlation between Nusselt number and Reynolds number such as $Nu = 0.035Re^m$ proposed by Woschni in [63], an instantaneous spatially average heat transfer coefficient is derived as shown below:

$$h_c = CB^{m-1}p_c^m w^m T_c^{0.75-1.62m}, \tag{2.16}$$

where C represents a scaling factor, B the length of a cylinder bore, w the average gas velocity in the cylinder, p_c the cylinder pressure and T_c the cylinder temperature. The ex-

ponent m is chosen to be 0.8 in this crank-angle based HCCI model. The spatially averaged cylinder gas velocity w is expressed as [53]:

$$w = \left[\left(0.4B \frac{2\pi N}{2 \cdot 60} \right)^2 + \left(c_1 \bar{S_p} + c_2 \frac{V_d T_{ivc}}{p_{ivc} V_{ivc}} (p_c - p_m) \right)^2 \right]^{1/2} \tag{2.17}$$

where V_d is the cylinder displaced volume, T_{ivc}, p_{ivc}, V_{ivc} are the cylinder temperature, pressure, and volume at the intake valve closing time, and p_m is the motored cylinder pressure at the same crank angle as the cylinder pressure p_c. $\bar{S_p}$ is the averaged piston speed. Two coefficients c_1 and c_2 in this model use:

$$c_1(\theta) = \begin{cases} 2.28 & 0 \leq \theta < 180 \\ 1.5 & 180 \leq \theta < 360 \\ 6.18 & 360 \leq \theta < 540 \\ 2.28 & 540 \leq \theta < 720 \end{cases}$$

and

$$c_2(\theta) = \begin{cases} 3.24 \times 10^{-3} & \theta_{SOC} \leq \theta < \theta_{SOC} + \Delta\theta_{comb}, \\ 0 & otherwise, \end{cases}$$

where $\Delta\theta_{comb}$ refers to the combustion duration (see Sec. 2.5.5) and θ is the engine crank angle.

2.5.4 Fuel Mass Fraction Burned Rate

To represent the fuel mass fraction burned Rate versus crank angle curve, Wiebe function is used as [64]:

$$\frac{dx_b}{dt} = 6\eta_c N \frac{a_b (m_b + 1)}{\Delta\theta_{comb}} \left(\frac{\hat{\theta} - \theta_{SOC}}{\Delta\theta_{comb}} \right)^{m_b} \exp\left(-a_b \left(\frac{\hat{\theta} - \theta_{SOC}}{\Delta\theta_{comb}} \right)^{m_b+1} \right), \tag{2.18}$$

where $\hat{\theta} = \theta - \theta_{SOC}$, where θ_{SOC} is the crank angle when the start of combustion occurs. η_c indicates the combustion efficiency and N is the engine speed. Two parameters, a_b = 5 and m_b = 2 are applied for this mass fraction burned rate curve, and we also assume $\eta_c = 1$ in the HCCI mode combustion. Using this information, the fuel mass burned rate $\dot{m}_b$, is computed with $\dot{m}_b = m_f \dot{x}_b$, where m_f is the injected fuel mass per each engine cycle. All combustion

timings such as the crank angle of 02%, 50% and 90% fuel burned (θ_{CA02}, θ_{CA50} and θ_{CA90}, respectively) and the combustion duration $\Delta\theta_{comb}$ defined by $\Delta\theta_{comb} = \theta_{CA90} - \theta_{CA02}$ are presented in the following section.

2.5.5 Combustion Timing

Arrhenius Integrals

It has been suggested by many researchers [65, 66] that the combustion autoignition timing in the HCCI engine is captured using the Arrhenius integral:

$$AR(\theta_{SOC}) = 1, \tag{2.19}$$

$$\begin{aligned} \text{where } AR(\theta) &= \int_{\theta_{ivc}}^{\theta} RR(\vartheta)\, d\vartheta \qquad \text{and} \\ RR(\vartheta) &= A p_{cyl}^{n_p}(\vartheta) \Phi^{n_\Phi} \chi_{O_2}^{n_{O_2}} \exp\left(-\frac{E_a}{R T_{cyl}(\vartheta)}\right), \end{aligned}$$

where $p_{cyl}(\vartheta)$ and $T_{cyl}(\vartheta)$ are in-cylinder pressure [atm] and temperature [K] at the crank angle ϑ, R is the universal gas constant [J/mol/K]. Φ is the in-cylinder equivalence ratio and χ_{O_2} is the mole percent of the oxygen O_2 at the intake valve closing (IVC). Note that assuming only small variations in engine speed during the period from IVC $\rightarrow$ SOC, the crank angle domain (ϑ) can be used for the integration argument.

Employing the volumetric ratio $v_{ivc}(\vartheta) = V_{cyl}(\vartheta_{ivc})/V_{cyl}(\vartheta)$ with $V_{cyl}(\vartheta)$ the cylinder volume at crank angle ϑ, and assuming a polytropic compression from IVC to SOC, the Arrhenius integrand can be represented as a function of the pressure p_{ivc} [atm] and temperature T_{ivc} [K] at IVC:

$$\begin{aligned} AR_4(\theta_{SOC}) &= 1 = \int_{\theta_{ivc}}^{\theta_{SOC}} RR(\vartheta) d\vartheta \\ &= \int_{\theta_{ivc}}^{\theta_{SOC}} A p_{ivc}^{n_p} v_{ivc}(\vartheta)^{\gamma n_p} \Phi^{n_\Phi} \chi_{O_2}^{n_{O_2}} \exp\left(-\frac{E_a v(\vartheta)^{1-\gamma}}{R T_{ivc}}\right) d\vartheta \end{aligned} \tag{2.20}$$

where $\gamma = 1.3$ is the specific heat ratio and other parameters A, n_p, n_Φ and n_{O_2} in the Arrhenius integral are parameters to be identified. The subscript 4 denotes the number of parameters to be determined.

Further simplification of the Arrhenius integral can be performed by eliminating χ_{O_2} in

(2.20):

$$AR_3(\theta_{SOC}) = 1 = \int_{\theta_{ivc}}^{\theta_{SOC}} RR(\vartheta)d\vartheta$$
$$= \int_{\theta_{ivc}}^{\theta_{SOC}} Ap_{ivc}^{n_p} v_{ivc}(\vartheta)^{\gamma n_p} \Phi^{n_\Phi} \exp\left(-\frac{E_a v(\vartheta)^{1-\gamma}}{RT_{ivc}}\right) d\vartheta, \qquad (2.21)$$

This simplification without the oxygen concentration χ_{O_2} can be supported by the parameterization in the following Sec. 2.5.5. Rausen *et al.* in [15] introduced a similar simplification for Arrhenius integral, in which, both mole percent of the oxygen χ_{O_2} and in-cylinder equivalence ratio Φ were considered not to be dominant factors in the simulation model. The reason to reserve the in-cylinder equivalence ratio Φ is to predict the combustion timing deviations for different fueling levels.

Parameterization of Arrhenius Integral

Parameters A, n_p, n_Φ and n_{O_2} in (2.20) and (2.21) are determined using combination of two MATLAB optimization routines, so called *DIRECT* and $fminunc$. First, *DIRECT*, a derivative-free sampling algorithm for the global optimum, was used to choose an appropriate estimate of the global solution. *DIRECT* requires no knowledge of the objective function gradient and, instead, samples points in the domain, and uses the information it has obtained to decide where to search next [67]. Second, $fminunc$ was utilized to determine the optimum more precisely using a gradient-based nonlinear optimization, which may give only local solutions [68]. These two methods together minimize the cost function f, which represents the square sum of errors between θ_{SOC} from the simulation model and the experimentally determined crank angle of 02% fuel burned θ_{CA02} for all hot and cold throttle sweep and fueling sweep at three different engine speeds (i.e. 1000, 1500 and 2500 RPM) in a single-cylinder gasoline HCCI engine.

$$f = \sum_{k=1}^{n} \left(\theta_{SOC,k} - \theta_{CA02,k}\right)^2, \qquad (2.22)$$

where n = 218 is the number of different steady-state experimental data. First, *DIRECT* is used to search a boundary of the global optimal parameter value. Next, $fminunc$ is run to examine the neighborhood of the potential value to decide one optimized value, which minimizes the objective function. Determined parameters A, n_p, n_Φ and n_{O_2} are shown in Table 2.2. Tow different Arrhenius integrals predict nearly similar SOC timing as shown in Fig. 2.6, therefore, simpler equation (2.21) is sufficient for the modeling purpose. To

Parameters	AR_4	AR_3
A	4.3180×10^9	4.6077×10^7
n_p	1.7884	1.7872
n_Φ	1.0634	1.0711
n_{O_2}	-1.5021	-

Table 2.2 Determined parameters in Arrhenius integral.

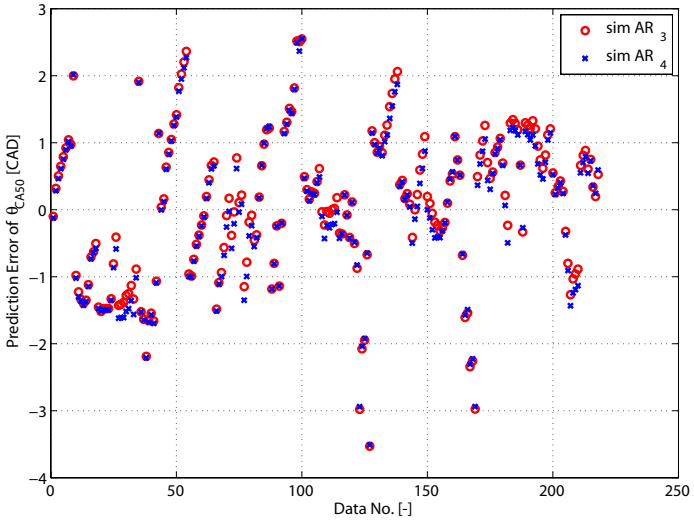

Figure 2.6 Prediction error of θ_{SOC} ($\theta_{SOC,sim}$ - $\theta_{SOC,dyno}$) between the dynamometer data and the model prediction.

enhance the prediction ability of the model, moreover, another modification was applied in the Arrhenius Integral with a saturation function for the equivalence ratio Φ. In specific, an extremely lean operating condition leads to a very low equivalence ratio Φ, which causes the late start of combustion timing. To prevent the equivalence ratio Φ from having a dominant effect in the Arrhenius integral, a saturation function $\tilde{\Phi}$ was introduced at a certain low value of Φ = 0.2246 (corresponding AFR = 65):

$$\tilde{\Phi} = \begin{cases} \Phi & \text{if } \Phi > 0.2246 \\ 0.2246 & \text{otherwise} \end{cases} \tag{2.23}$$

The simplified Arrhenius integral used in the crank-angle based HCCI model to predict the SOC timing, θ_{SOC} is:

$$AR(\theta_{SOC}) = 1, \tag{2.24}$$

$$\text{where } AR(\theta) = \int_{\theta_{ivc}}^{\theta} RR(\vartheta)\,d\vartheta \quad \text{and}$$

$$RR(\vartheta) = Ap_{ivc}^{n_p} v_{ivc}(\vartheta)^{\gamma n_p} \tilde{\Phi}^{n_\Phi} \exp\left(-\frac{E_a v(\vartheta)^{1-\gamma}}{RT_{ivc}}\right) d\vartheta.$$

Note that the Arrhenius integral is able to capture the engine misfire behavior, which is caused by (i) the loss of spark (SI mode), (ii) insufficient air/fuel mixture condition to ignite, or (iii) loss of compression (SI and HCCI mode). For instance, if engine is run at a low equivalence ratio region (lean operation condition) or cylinder temperature and pressure is not sufficiently high at IVC timing, the Arrhenius integral does not get to a trigger point, that is, $AR = 1$. This misfire, hence, results in the motored cylinder dynamics.

Computation of θ_{CA50} and θ_{CA90}

Determination of the SOC timing is challenging due to the measurement noise of the cylinder pressure sensor. Therefore, computed SOC from the model simulation is compared with the crank angle of 02% fuel burned from a HCCI dynamometer engine for the model validation purpose. To study the crank angle of 50% fuel burned, the experimental data is plotted in Fig. 2.7.

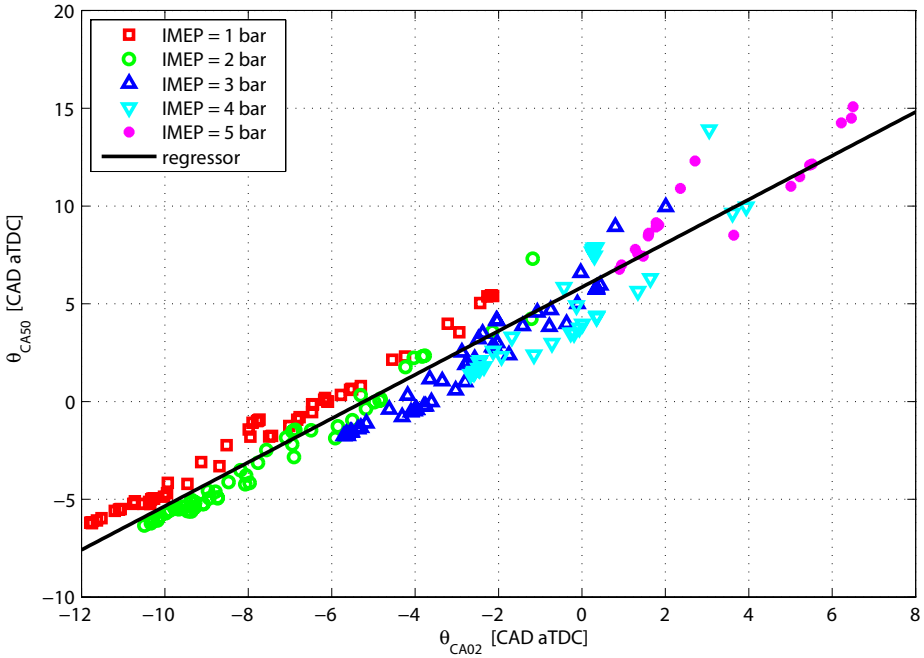

Figure 2.7 θ_{CA02} vs. θ_{CA50} regression.

This plot proposes the regression equation with similar manner in [25]:

$$\theta_{CA50} = a_1 \theta_{CA02} + a_2, \tag{2.25}$$

where the coefficients a_1 and a_2 are determined by standard least squares (LS). These two coefficients do not change significantly for different engine speeds and engine loads, hence one linear regression fit is used for the HCCI model to predict the value of θ_{CA50}. We define the combustion duration, $\Delta\theta_{comb}$, as the crank angle between 02% fuel burned and 90% fuel burned and θ_{CA90} is computed as:

$$\theta_{CA90} = \theta_{CA02} + \Delta\theta_{comb} = \theta_{CA02} + a_3 (\theta_{CA50} - \theta_{SOC}), \tag{2.26}$$

where $a_3 = 1.8$ is chosen for this model by assuming that $(\theta_{CA90} - \theta_{CA02})/(\theta_{CA50} - \theta_{CA02}) \approx 90/50 = 1.8$. This regressor between θ_{CA02} and θ_{CA90} is represented in Fig. 2.8. Note that the θ_{CA90} prediction with one simple regression equation seems not sufficient by inspection in Fig. 2.8, and more complicated equation including the injected fuel amount per each cycle m_f, instead, might be recommended. For instance, $\theta_{CA90} = f(m_f, \theta_{CA02}) = \alpha_1 m_f \theta_{CA02} + \alpha_2 m_f + \alpha_3 \theta_{CA02} + \alpha_4$ might be a more accurate regression. This new regression with steeper gradient for each fueling level, has better prediction for θ_{CA90} and, hence, combustion duration $\Delta\theta_{comb}$. The red dashed reference line (i.e. a linear line crossing the origin with a gradient of 1) in Fig. 2.8, however, indicates that the new regression with the steep gradient an very high sensitivity in SOC prediction errors. In the case where the model predict earlier SOC than the dynamometer engine, the error is magnified through the steep gradient and, hence, causes some rare but very large overall prediction errors. In light of this error propagation, the higher fidelity, fuel dependent, combustion duration is abandoned.

2.6 Steady State Validation

The purpose of the steady state experiments was to (i) assess effects of inlet air charge temperature, which is the primary control variable for this combustion control concept, on other engine variables; (ii) generate data used for model calibration and validation. The steady state data were collected at Ford Motor Co. The HCCI dynamometer engine experiments were performed with several planned mapping points for given engine speed, load, hot air temperature, hot throttle angle and cold throttle angle. This steady state operating range was determined aiming low cycle-to-cycle combustion variability. The fuel rate and the hot

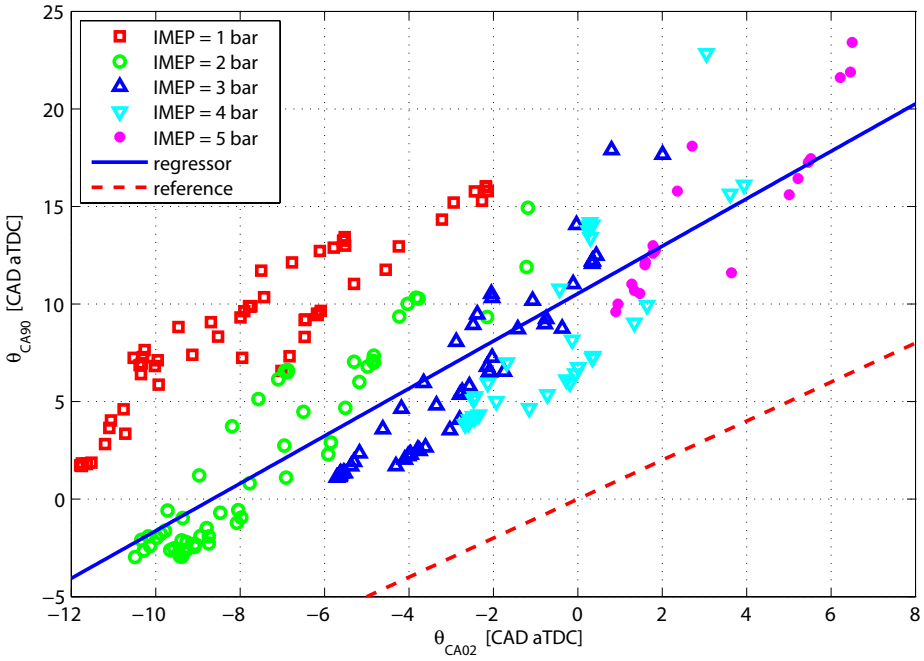

Figure 2.8 θ_{CA02} vs. θ_{CA90} regression.

inlet temperature were altered simultaneously and judiciously up until operation was not feasible due to too fast combustion, misfires or high covariance of IMEP. The steady state HCCI engine test region for various load conditions at the engine speeds of 1000, 1500 and 2500 RPM is shown in Fig. 2.9.

For the engine speeds of 1000, 1500 and 2500 RPM, different IMEP from 1.26 through 5, IMEP from 1.2 through 4.85 and IMEP from 1.4 trough 3 bar, respectively, were examined while changing the hot and cold throttle angles. Each IMEP test requires a certain amount of heat sources, or more precisely, the certain temperature of the hot inlet air flow into the cylinder. Table 3.1 shows the adjusted hot air temperature T_h, for different IMEP at different engine speeds for mapping. Each of the speed and load operating point in Table 3.1 was repeated with (i) hot throttle sweep while the cold throttle was closed and (ii) cold throttle sweeps while the hot throttle was wide open. A corresponding steady state HCCI engine test region is depicted in Fig. 2.9 based on the measured engine performance.

The inputs, N, $\dot{m}_f$, θ_c, θ_h, T_0 and T_h in the model are the constant commanded values for the steady state validation. Steady state dynamometer engine test data with a IMEP covariance less than 10 were selected for comparison purpose in this section. Table 3.2 shows mean μ, standard deviation σ, minimum and maximum values of the prediction error, which is determined by the difference between the steady state dynamometer engine test data and simulation estimation (i.e. $x_{dyno} - \hat{x}_{sim}$, where x is the output variables). It indicates how well the model predicts significant engine performance values such as IMEP,

Engine Speed [RPM]	Steady State Operating Conditions				
1000	Fuel Rate [mg/cycle]				
	6.4	8.6	11.8	15	18.2
	IMEP [bar]				
	1.26	2	3	4	5
	Hot Inlet Temperature [°C]				
	225	210	160	130	105
1500	Fuel Rate [mg/cycle]				
	6.2	8.6	11.8	15	18.2
	IMEP [bar]				
	1.2	2	3	4	4.85
	Hot Inlet Temperature [°C]				
	220	200	150	120	100
2500	Fuel Rate [mg/cycle]				
	6.4	8.6	11.8	15	18.2
	IMEP [bar]				
	1.4	2	3	-	-
	Hot Inlet Temperature [°C]				
	210	220	150	-	-

Table 2.3 Summary of steady-State HCCI dynamometer engine experiment plan with various cold and hot throttle angles.

AFR, θ_{CA02}, θ_{CA50} and exhaust temperature T_2 for all of the steady state test points using the HCCI dynamometer engine. Moreover, negative prediction error indicates the overestimation of the model during the simulation, while positive error denotes underestimation. Small mean values indicate that there is no conspicuous bias between the dynamometer engine data and simulation model prediction values. A relatively large standard deviation of θ_{CA50} and T_2 prediction errors, however, are reasons for concern. Specifically, the simple linear correlation between θ_{CA02} and θ_{CA50} in (2.25) is related to a bigger standard deviation of the prediction error of θ_{CA50} than θ_{CA02}. For the exhaust temperature T_2, a large prediction error was induced mainly by the high engine speed operating conditions. For instance, cold throttle sweep test with a load of IMEP = 1 and 3 bar at the engine speed of N = 2500 RPM. The model does not predict very well the exhaust temperature changes as throttle angle changes.

Fig. 2.10 through 2.14 compare the model prediction with the dynamometer engine

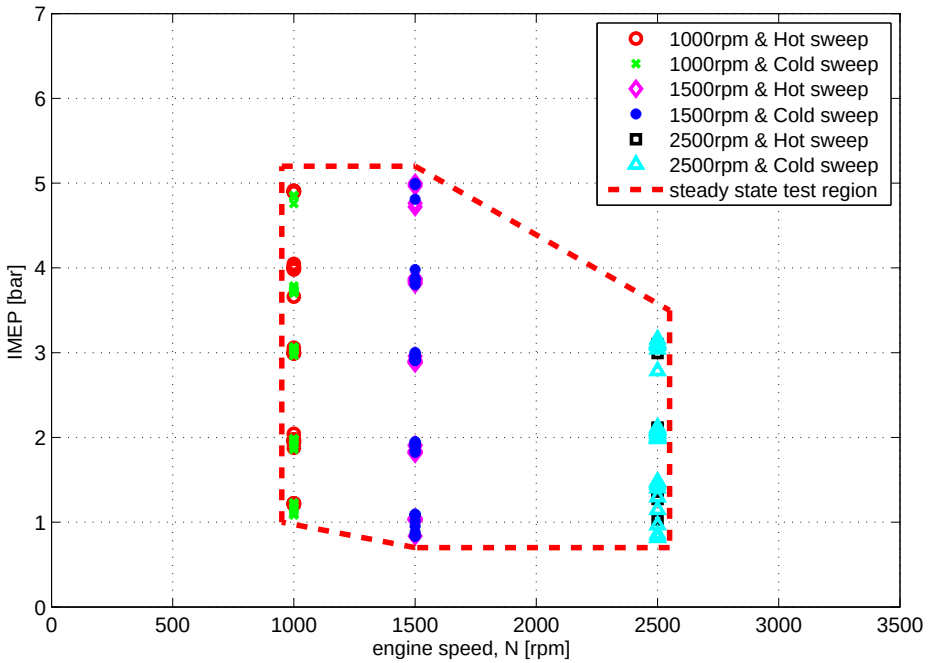

Figure 2.9 All steady state HCCI engine test region for various load conditions at the engine speeds of 1000, 1500 and 2500 RPM.

	Prediction Error			
	Mean (μ)	STD (σ)	Min	Max
IMEP [bar]	-0.0041	0.2409	-0.5409	0.5498
AFR [-]	0.2727	1.6987	-3.1150	7.6200
θ_{CA02} [CAD]	0.3068	1.0244	-4.0728	2.6284
θ_{CA50} [CAD]	0.3067	1.5093	-3.6921	4.7576
T_2 [°C]	1.6506	12.8853	-49.2808	34.8706

Table 2.4 Mean (μ), standard deviation (σ), Min and Max values of the model prediction error, that is, the difference between the dynamometer engine data and model prediction values.

data during steady state test. The x-axis is used for the dynamometer data, while the y-axis for the model prediction values. Black solid line and blue dashed line represent the mean and standard deviation of prediction errors, respectively.

For IMEP comparison in Fig. 2.10, the model tends to overestimate engine IMEP performance at low load (i.e. IMEP $\approx$ 1.3 bar), while it underestimate IMEP at high loads (i.e. IMEP $\approx$ 4 and 5 bar). The largest prediction errors happen during the cold throttle sweep validation with IMEP = 1.2 bar at N = 1500 RPM, and the hot throttle sweep with IMEP = 4 bar at N = 1000 RPM.

In Fig. 2.11, for AFR comparison, cold throttle sweep at N = 2500 RPM has the biggest

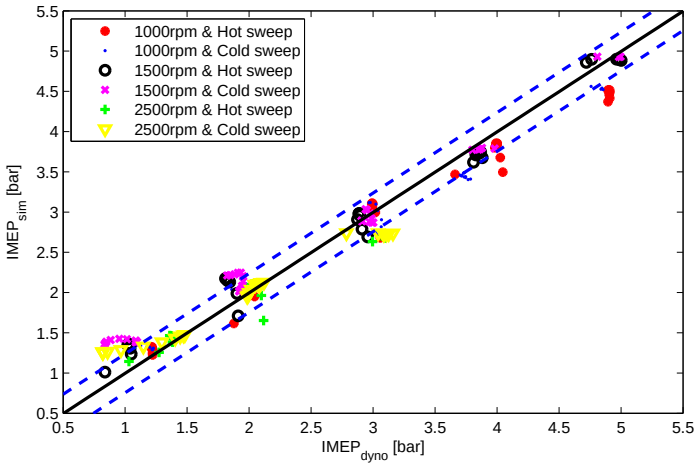

Figure 2.10 Comparison of IMEP between the dynamometer engine data and the model simulation: Black solid line and blue dashed line indicate the mean and standard deviation of prediction errors, respectively.

prediction error. The prediction capability of the model is, however, comparatively good at two low engine speed simulation (i.e. N = 1000 and 1500 RPM). This is related to the tradeoff during the model calibration process for the flows through the throttle valves, performed in Sec. 2.3. We concentrate more on the model prediction capability at lower speed than high speed.

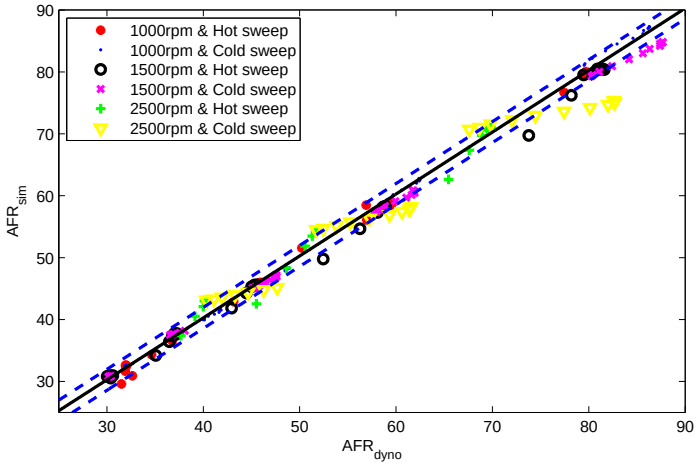

Figure 2.11 Comparison of AFR between the dynamometer engine data and the model simulation: Black solid line and blue dashed line indicate the mean and standard deviation of prediction errors, respectively.

Model simulation for hot throttle sweep at both 1000 and 1500 RPM are the cause of the large standard deviation as depicted on the θ_{CA02} comparison plot in Fig. 2.12. The largest prediction error happens in the boundary of stable combustion region. For instance, nearly closed hot throttle condition with cold throttle closed or wide open cold throttle case with

wide open hot throttle are not predicted as well. At these edges, in general, the covariance of IMEP is relatively high (i.e. close to 10).

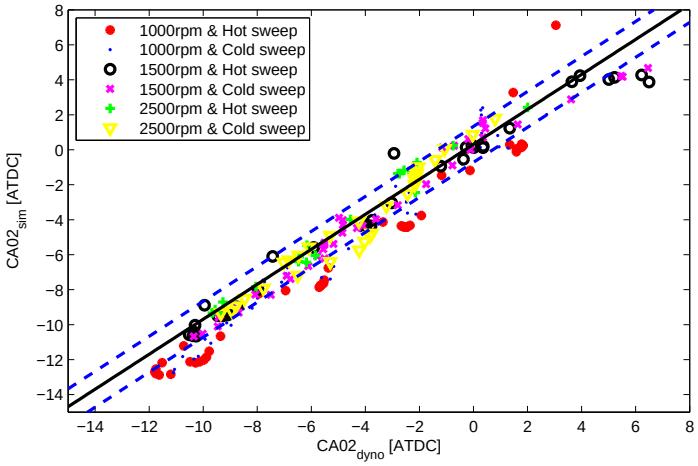

Figure 2.12 Comparison of θ_{CA02} between the dynamometer engine data and the model simulation: Black solid line and blue dashed line indicate the mean and standard deviation of prediction errors, respectively.

Fig. 2.13 shows a comparison of θ_{CA50} between the dynamometer engine data and the model simulation. Model prediction error from θ_{CA02} propagates on θ_{CA50} prediction due to the simple linear correlation model between θ_{CA02} and θ_{CA50}. Therefore, our model starts loosing fidelity at the edges of the operating region (i.e. for late or very early combustion). There might be a chance to slightly improve the θ_{CA50} prediction ability if we apply more complicated correlation than a single linear one in (2.25).

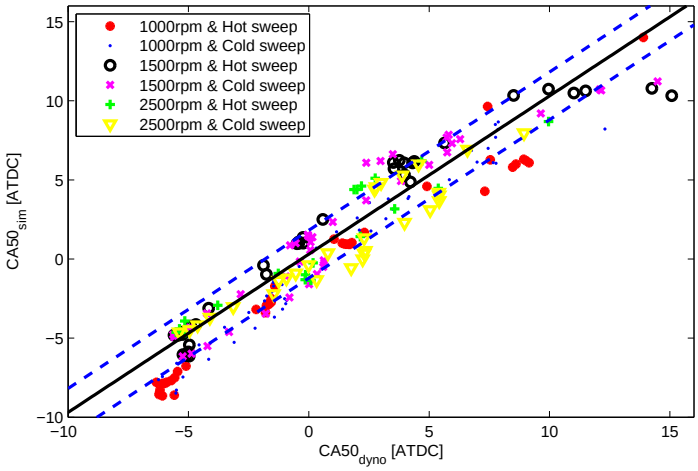

Figure 2.13 Comparison of θ_{CA50} between the dynamometer engine data and the model simulation: Black solid line and blue dashed line indicate the mean and standard deviation of prediction errors, respectively.

Similar to the AFR comparisons, the model prediction of the exhaust temperature T_2 at N = 2500 RPM has bigger error than the other two engine speeds, especially in the cold

throttle sweep simulation. Improvement of the AFR prediction in the cold throttle sweep at N = 2500 RPM can induce more accurate predictions on other engine performance variables. For instance, better accuracy on the air flow prediction through the cold throttle sweep at the high speed of N = 1500 RPM will lower the charge temperature inside cylinder at IVC and, hence, retard the SOC timing. Later SOC timing associated with larger combustion duration can induce lower peak cylinder pressure and temperature, which will improve the model prediction capability with respect to all engine performance variables, i.e. IMEP, AFR, θ_{CA02}, θ_{CA50} and T_2.

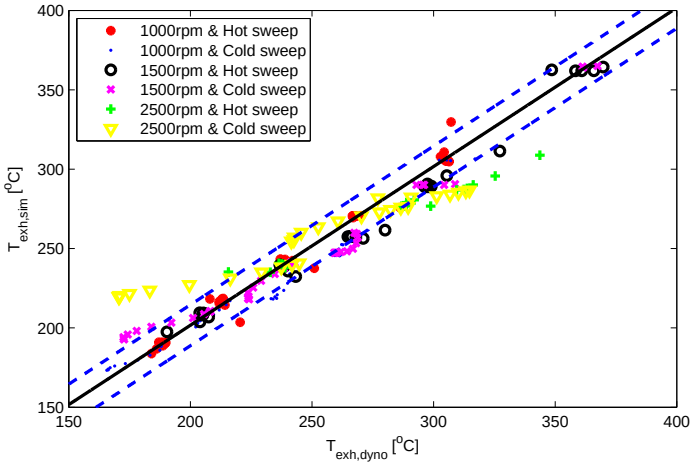

Figure 2.14 Comparison of T_2 between the dynamometer engine data and the model simulation: Black solid line and blue dashed line indicate the mean and standard deviation of prediction errors, respectively.

2.7 Transient Data Validation

To complete the model validation and apply proper control strategies, some meaningful transient test of the HCCI engine must be performed and compared with the model prediction. Table 2.5 shows three different transient test plans for the single cylinder HCCI dynamomter engine: (1) load change, (2) cold throttle change, (3) hot throttle change. Note that the marked test data sets are used for the validation in this section. The transient data were provided with two different dSPACE data sets for each test: (i) one collected at a crank-angle resolved sampling rate with 1 crank angle degree resolution, and (ii) the other saved at a 10 crank-angle resolved sampling rate. The first one contains all the information used for the real-time pressure processor, such as manifold absolute pressure (MAP) and cylinder pressure, and engine emission data. The second one involves the computed combustion timing, that is, θ_{CA02}, θ_{CA50}, θ_{CA90}, and all commanded engine control inputs,

engine speed N, cold throttle angle θ_c, hot throttle angle θ_h, fuel injection rate $\dot{m}_f$, fuel injection pulse width, and so on.

	Engine Inputs					
	N [RPM]	$\dot{m}_f$ [mg/cycle]	T_h [^{o}C]	θ_c [%]	θ_h [%]	
Load	1500	$8.5 \rightarrow 11.6 \rightarrow 8.5$	160	20	100	✓
	1500	$11.6 \rightarrow 14.5 \rightarrow 11.6$	160	20	100	
Cold throttle	1500	8.5	180	$30 \rightarrow 50 \rightarrow 30$	100	✓
	1500	14.0	120	$20 \rightarrow 40 \rightarrow 20$	100	
Hot throttle	1500	8.5	180	0	$50 \rightarrow 30 \rightarrow 50$	✓
	1500	14.0	120	0	$70 \rightarrow 40 \rightarrow 70$	

Table 2.5 Summary of transient HCCI dynamometer engine experiment plan with load, throttle, engine speed and load/speed changes.

For validation purposes, we report and compare the predicted and experimentally calculated crank angle for 10% fuel burned θ_{CA10} instead of the crank angle of 2% burned θ_{CA02} observed experimentally against the start of combustion θ_{SOC} from model prediction. θ_{CA10} has lower noise level than the θ_{CA02} from a single pressure trace. Although θ_{CA02} can be used in steady state data due to the averaging of multiple cycles, sometimes up to 50 cycles, θ_{CA02} is not a good prediction measure for single cycle processing. It is difficult for the transient test to perform the same post-processing task if the collected data have distortion and noise. Mass fraction burned (MFB) curves for two different operating conditions in Fig. 2.15 demonstrate the cycle-to-cycle variation and the the noisy in-cylinder pressure data. Crank angles at 2% fuel burned θ_{CA02} for two different operating conditions (i.e. 50% and 30% hot throttle open) are overlapping such that θ_{CA02} values are inappropriate for the comparison with the model prediction data. Instead, the crank angles at 10% θ_{CA10} are more suitable to be used for the model validation purpose since these values seem more differentiable than θ_{CA02}. Similarly, θ_{CA80} is more distinguishable than θ_{CA90}. Note also here that in closed loop control of the HCCI combustion, θ_{CA50}, location of peak pressure, and peak pressure will be used as feedback.

To predict the values of θ_{CA10} using the model, similar scheme has been applied as the θ_{CA50} computation. Since θ_{CA10} values are available from the steady-state data, we can create a simple linear equation between θ_{CA02} and θ_{CA10}, which is depicted in Fig. 2.16. For the validation purposes, during the transient tests, θ_{CA10} predictions are computed using the linear equation based on θ_{CA02} of (2.25)

$$\theta_{CA10} = 1.0961\theta_{CA02} + 2.65. \tag{2.27}$$

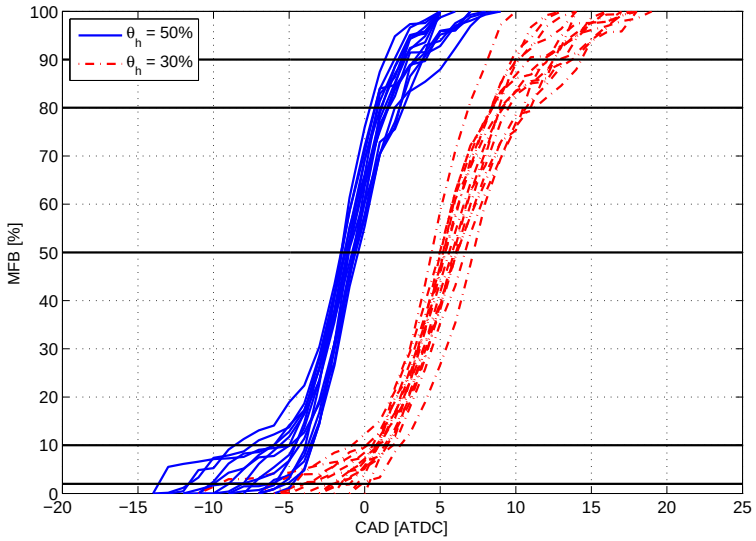

Figure 2.15 Mass fraction burned (MFB) curves computed from the dynamometer transient test (θ_c = 0%, θ_h = 50% $\rightarrow$ 30%, IMEP $\approx$ 2 bar, N = 1500 RPM).

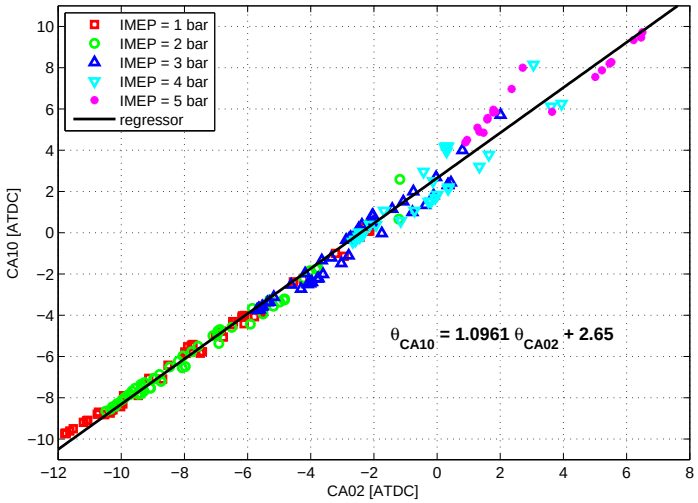

Figure 2.16 θ_{CA02} and θ_{CA10} for all steady-state data

Fig. 2.17 represents the load step changes with all the other engine inputs fixed such as cold and hot inlet air temperature, T_0 = 39°C and T_h = 157°C, cold and hot throttle angles, θ_c = 0% and θ_h = 100%, and engine speed N = 1500 RPM. The peak pressure p_{peak}, location of peak pressure $Loc\ p_{peak}$, and, hence, IMEP immediately change once fuel injection rate per each cycle changes. Underestimation of p_{peak} induces an offset in the IMEP prediction of 0.5 bar. During fuel step changes, combustion timing alters very little, but, the cylinder pressure processing does not capture the deviation in θ_{CA10} so well, while θ_{CA50} is distinguishable. The dynamometer HCCI engine has a lag in θ_{CA50} performance with

a time constant of approximately 1 second unlike the model prediction. For the model to capture this lag, it is necessary to revise the parameter selection, particularly the parameters c_p and m in (2.13) - (2.15). This will be done in the near future, along with investigation of potential order reduction of the heat transfer dynamics.

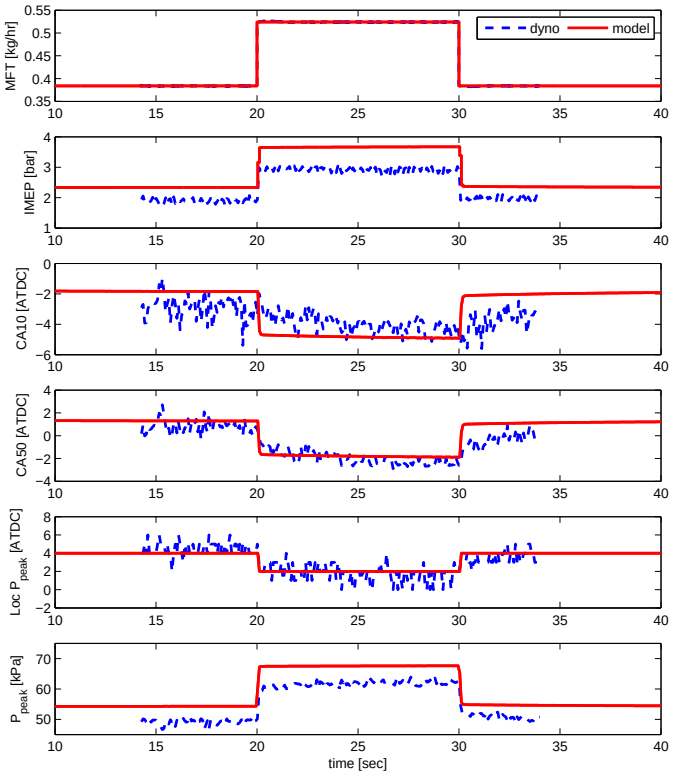

Figure 2.17 Load change (θ_c = 0%, θ_h = 100%, T_0 = 39°C, T_h = 157°C, N = 1500 RPM) : blue dashed lines show the post-processed dynamometer data and red solid lines display the model simulation result

In Fig. 2.18, the cold throttle changed during other engine inputs fixed as θ_h = 100%, T_0 = 34°C, T_h = 176°C and N = 1500 RPM. Since the magnitude of noise in the cylinder pressure data is comparable to the magnitude change achieved by the cold throttle change, there is a large fluctuation in the experimental θ_{CA10}. On the other hand, for θ_{CA50} calculation, the noise effect can be alleviated by the filtering in the pressure process algorithm. This will be explained in the next chapter. There is an offset of 3 crank angle degree and 6 kPa in the prediction of the location of peak pressure and peak pressure, respectively.

A transient test with hot throttle change is shown in Fig. 2.19, during which other engine inputs were fixed as θ_c = 0%,T_0 = 43°C, T_h = 185°C, N = 1500 RPM. IMEP prediction is good enough compared with the test data, while both θ_{CA10} and θ_{CA50} predictions show approximately 2 crank angle degree offset. p_{peak} and $Loc\ p_{peak}$ predictions demonstrate that the model has the right trend even though there exists a certain amount of bias.

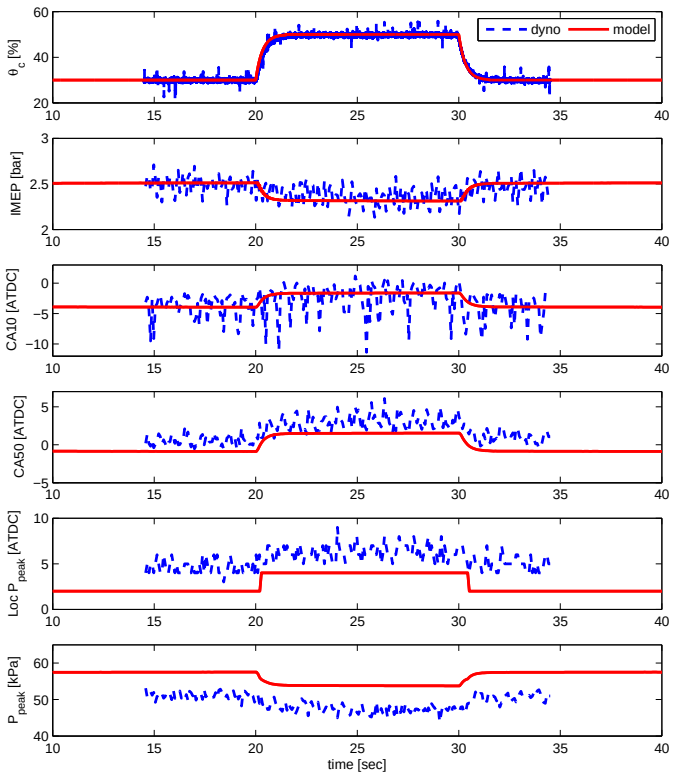

Figure 2.18 Cold throttle change (θ_c = 30% $\rightarrow$ 50% $\rightarrow$ 30%, θ_h = 100%, $T_0 = 34^{\circ}C$, $T_h = 176^{\circ}C$, N = 1500 RPM) : blue dashed lines show the post-processed dynamometer data and red solid lines display the model simulation result

2.8 Conclusion

A crank angle based HCCI engine model containing 9 states is presented in this chapter. Different from typical mean value models developed for single cylinder engines, the present model not only simulates cycle average engine variables, it is also designed to capture:

- the impact of various engine speed, that is, 1000, 1500 and 2500 RPM on the combustion performance variables θ_{CA02} and θ_{CA50} as well as IMEP and AFR
- the impact of fuel injection rates mainly on IMEP, θ_{CA02} and θ_{CA50}
- the effect of inlet air charge temperature on the engine combustion variables θ_{CA02} and θ_{CA50}
- the changes of the engine outputs due to two throttle actuators
- Misfire prediction using the Arrhenius integral.

The model provides the basis for dynamical analysis and controller design of the HCCI engine. Furthermore, it can be combined with SI mode to accomplish a control strategy for the mode changes between HCCI and SI mode.

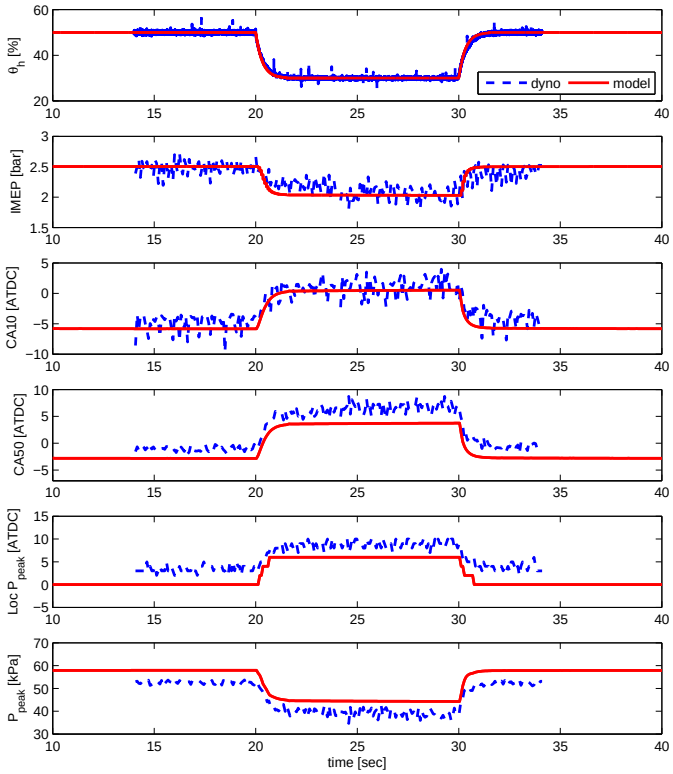

Figure 2.19 Hot throttle change (θ_c = 0%, θ_h = 50% $\rightarrow$ 30% $\rightarrow$ 50%, T_0 = 43°C, T_h = 185°C, N = 1500 RPM) : blue dashed lines show the post-processed dynamometer data and red solid lines display the model simulation result

The crank-angle based HCCI engine model developed in this chapter was validated using both steady state and transient tests in this chapter. For steady state validation purpose, the dynamometer engine test data with IMEP covariance less than 10 were used. Large deviations between engine and model with respect to the cold throttle flow at the engine speed of 2500 RPM propagate through other engine performance variables, such as AFR, IMEP, exhaust temperature T_2, θ_{CA02} and θ_{CA50}. Prediction error, however, can be diminished if we compare the model prediction with relatively large IMEP covariance, for instance, IMEP covariance = 3.

In the transient data comparison, it was observed that the HCCI model captures proper tendency for cold and hot throttle change compared to the dynamometer data, even though it shows some bias. The dynamics associated with fuel or load changes need re-tuning because the model fails to predict the slow changes in θ_{CA50}. In specific, the parameters c_p and m associated with the temperature evolution of the cylinder parts need to be reparameterized based on further investigation. Computation of combustion timing (i.e. θ_{CA10} and θ_{CA50}) using a single cycle pressure data was affected by the measurement noise. Therefore, a robust pressure processing algorithm is highly required.

Chapter 3
HCCI Closed-loop Combustion Control

3.1 Introduction

Various HCCI control methodologies have been discussed in previous literature; for instance, exhaust gas recirculation (EGR) rate [69], internal residuals with variable valve timing (VVT) [70, 71], and fast thermal management (FTM) with variable compression ratio (VCR) [72]. All these different techniques pursue a similar objective, which is sufficient thermal energy to initiate auto-ignited combustion. The heated air HCCI engine presented in this chapter regulate in-cylinder temperature by two intake port throttles, one providing heated air and the other cold ambient air into the cylinder. Control synthesis and design requires a model that represents the effects of the valve actuators to the charge conditions and the HCCI combustion characteristics. Phenomenological crankangle-resolved HCCI combustion models have been developed in Chapter 2. Although these models are indispensable for understanding and simulating HCCI combustion, low-order models are necessary for real-time feedback and observer design.

In the rest of this chapter, a mean value model (MVM) of single cylinder heated air HCCI engine is summarized and validated using transient dynamometer engine test data in section 4.2. This MVM is based on the crank-angle resolved HCCI model presented in [53]. In section 3.3, we show that the combustion duration, $\Delta\theta_{comb}$, redefined as the duration between the crank angle of 10$ and 90% fuel burned in this chapter, can be a good proxy for both combustion stability and fuel efficiency with respect to the covariance of indicated mean effective pressure (IMEP) and indicated specific fuel consumption (ISFC), respectively. Based on this observation, a controller is developed to regulate $\Delta\theta_{comb}$ by the two throttle actuators and the results are presented in section 3.4.

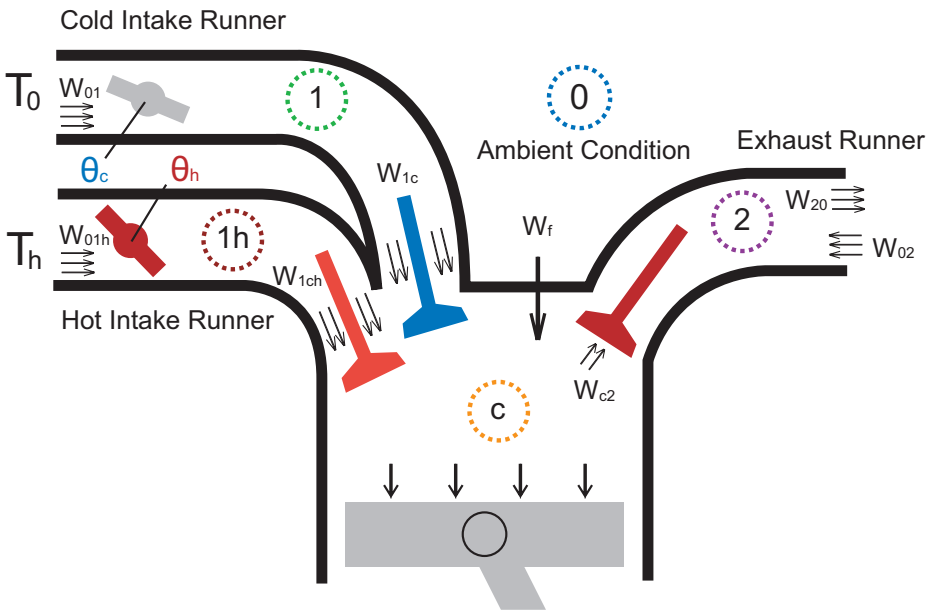

Figure 3.1 Notation used for the crank-angle resolved HCCI engine model.

3.2 Mean Value Model and Validation

In this section, the model structure and notation used for a simple HCCI MVM will be introduced first, and the validation data will be shown in the following sections.

3.2.1 Model Structure and Notation

A simple HCCI MVM presented here includes a statistical physics based parametrization of the observed HCCI behavior during dynamometer testing and measurements. The MVM attempts to represent the entire cycle (intake, compression, expansion and exhaust strokes) of a single cylinder HCCI engine with controlled throttles (θ_c and θ_h) installed at the intake ports. The represented dynamical behavior is, therefore, only associated with the cycle-to-cycle delay, $\tau = N/120$, where N [RPM] indicates the engine speed. Fig. 3.1 shows the notation used in the crank-angle resolved HCCI engine model. Variables associated with ambient condition are denoted by subscript 0, while the variables related to heated air conditions by subscript h. The cold and hot intake runners are referred to as volume 1 and 1h, the exhaust runner volume as volume 2. Flows are depicted according to the notation W_{xy} where x and y are the upstream and downstream of the flow. Heated air flow is described by an additional subscript h such that W_{xyh}.

3.2.2 Cycle Averaged Pumping Flows

The two throttle actuators in the hot and cold intake runners control both total amount of cycle averaged air mass flow into the cylinder, $W_{ivc} = W_{1c} + W_{1ch}$, and the fraction of each mass flow between the hot and cold intake runners, $r_{ivc} = W_{1ch}/W_{1c}$ at IVC. We assume that the manifold filling dynamics in the hot and cold intake runners are negligible such that cylinder pumping flows, W_{1c} and W_{1ch}, are identical to the throttle flows, W_{01} and W_{01h}, respectively. These two variables, W_{ivc} and r_{ivc}, are determined based on the hot and cold throttle angles, θ_h and θ_c, heated inlet air temperature, T_h, and engine speed, N, as followings:

$$\begin{aligned} W_{ivc} &= f_w(\theta_c, \theta_h, T_h) \\ &= -\alpha_1 e^{-\alpha_2 \theta_h} + \alpha_3 \left[1 - e^{-\alpha_4 (\frac{\theta_c}{100})^{\alpha_5}}\right] + \alpha_6 T_h + \alpha_7, \end{aligned} \tag{3.1}$$

$$\begin{aligned} r_{ivc} &= f_r(\theta_c, \theta_h, T_h) \\ &= (\beta_1 T_h + \beta_2) \left[\beta_3 - e^{-\beta_4 (\frac{\theta_h}{100})^{\beta_5}}\right] \left[(1-\beta_6) e^{-\beta_7 \theta_c} + \beta_6\right], \end{aligned} \tag{3.2}$$

where α_i and β_i for $i = 1, \ldots, 7$ are functions of engine speed (N) such that $\alpha_i = f_\alpha(N) = \alpha_{i1} N^2 + \alpha_{i2} N + \alpha_{i3}$ and $\beta_i = f_\beta(N) = \beta_{i1} N^2 + \beta_{i2} N + \beta_{i3}$.

All the parameters in (3.1) and (3.2) were determined based on averaging the simulated flows over the intake stroke using the crank angle based HCCI engine model in [53]. The comparisons of W_{ivc} and r_{ivc} between the crank angle based HCCI engine model simulation data and the pumping flow maps from (3.1) and (3.2) for various loads, engine speeds, and throttles are shown in Fig. 3.2.

3.2.3 Combustion Timing and Duration

If we neglect the effect of residual gas in cylinder after exhaust valve closing (EVC), the cylinder temperature at IVC, T_{ivc}, can be approximated as the weighted temperature sum of mixing gas flows from cold and hot intake runners, $W_c T_0$ and $W_h T_h$,

$$T_{ivc} = \frac{W_{1c} T_0 + W_{1ch} T_h}{W_{1c} + W_{1ch}}, \tag{3.3}$$

where $W_{1c} = \frac{W_{ivc}}{1+r_{ivc}}$, $W_{1ch} = \frac{W_{ivc} r_{ivc}}{1+r_{ivc}}$, and T_0 denotes the ambient air temperature.

As discussed by [31], we assume that the cylinder temperature at IVC, T_{ivc}, and injected fuel amount per each cycle, m_f [mg/cycle], are the dominant for defining the start of combustion, θ_{SOC}, and combustion duration $\Delta\theta_{comb}$. θ_{SOC} is considered to be identical with the crank angle of 02% fuel burned timing, θ_{CA02}, in this chapter. Instead of the Arrhenius

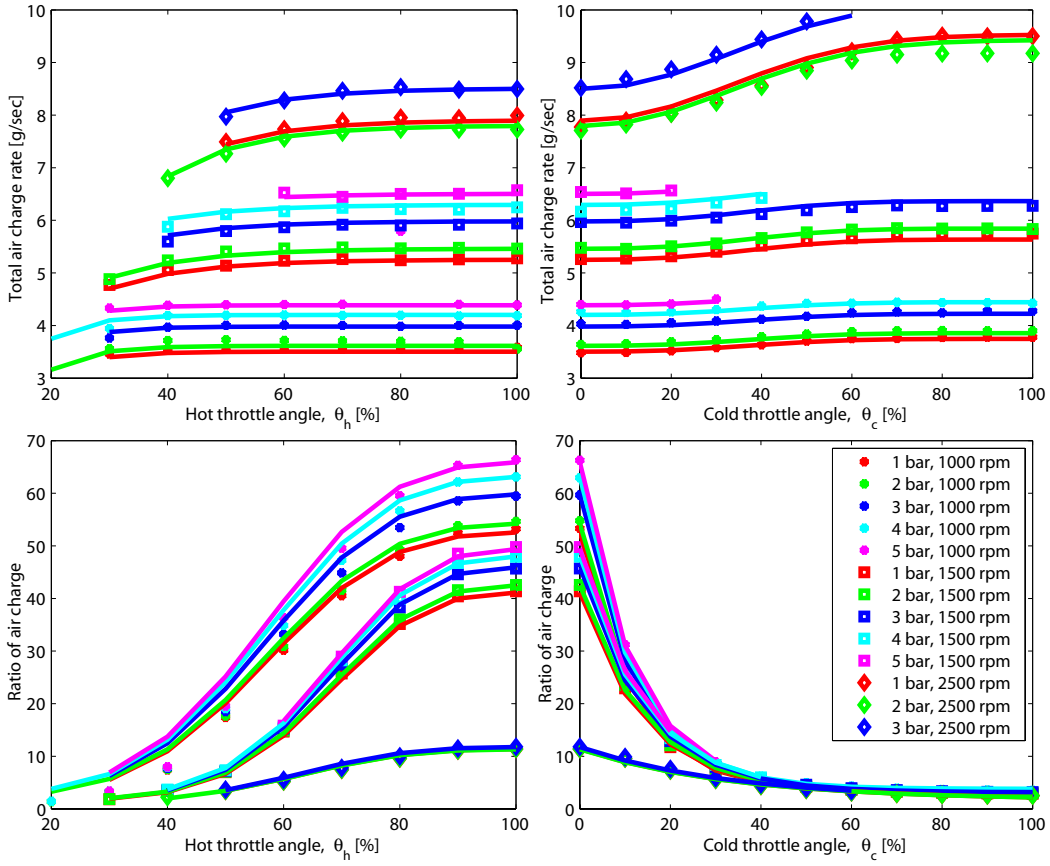

Figure 3.2 Comparison between crank-angle based HCCI engine simulation (dot points) and pumping flow map (solid lines) from (3.1) and (3.2).

integral used in the crank angle resolved model, predicted θ_{CA02} and $\Delta\theta_{comb}$ are computed based on polynomial equations based on the modeled T_{ivc} through (3.3) and m_f such that

$$\theta_{CA02} = f_{CA02}(T_{ivc}) = \gamma_1 T_{ivc} + \gamma_2, \tag{3.4}$$

$$\Delta\theta_{comb} = f_{comb}(\theta_{CA02}) = \zeta_1 \theta_{CA02} + \zeta_2, \tag{3.5}$$

where γ_i and ζ_i for $i = 1,2$ are determined as $\gamma_i = f_\gamma(m_f) = \gamma_{i1} m_f^2 + \gamma_{i2} m_f + \gamma_{i3}$ and $\zeta_i = f_\zeta(m_f) = \zeta_{i1} m_f^2 + \zeta_{i2} m_f + \zeta_{i3}$ using the measured θ_{CA02} and the modeled T_{ivc}. Fig. 3.3 shows the comparisons of θ_{CA02} and $\Delta\theta_{comb}$ between the steady state dynamometer HCCI engine test data and the estimated values using (3.4) and (3.5).

The crank angle of 50% fuel burned, θ_{CA50} can be approximated using a linear equation based on θ_{CA02} as suggested in [53] and shown in Fig. 3.4

$$\theta_{CA50} = f_{CA50}(\theta_{CA02}) = \eta_1 \theta_{CA02} + \eta_2. \tag{3.6}$$

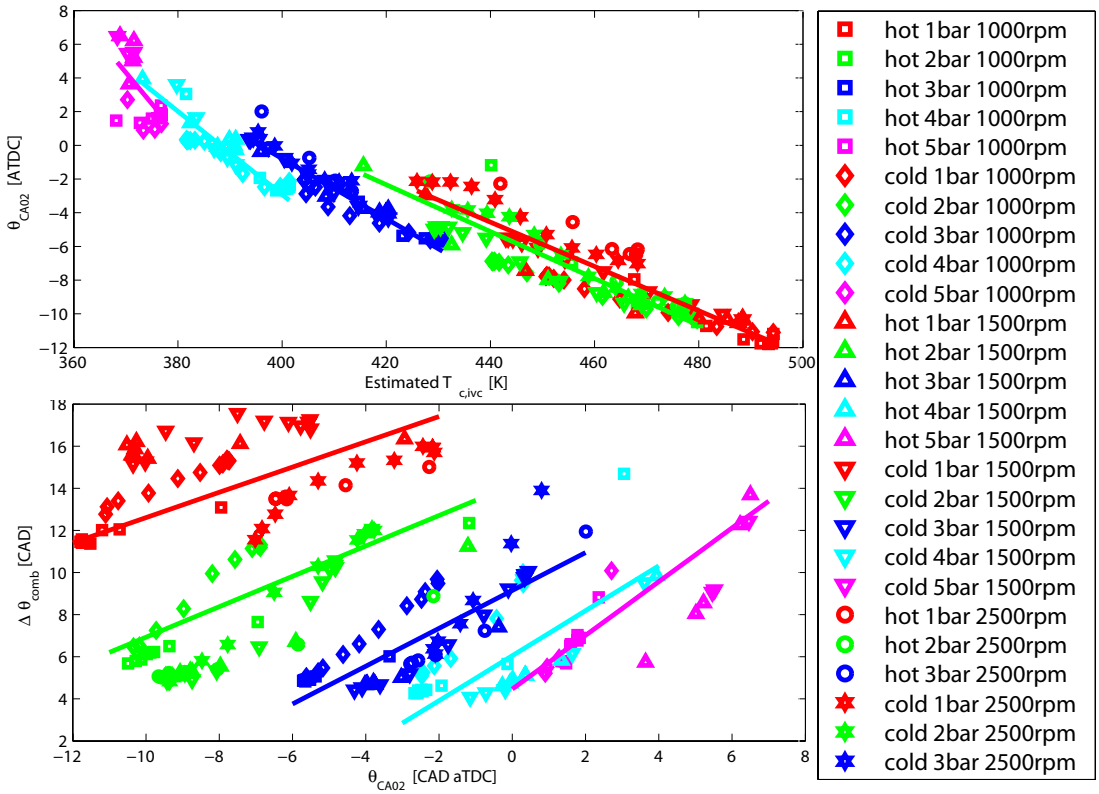

Figure 3.3 Comparison of θ_{CA02} and $\Delta\theta_{comb}$ from the steady state dynamometer test (dot points) and (3.4) and (3.5) (solid lines) for different operating conditions.

3.2.4 Exhaust Temperature

Modeling of exhaust temperature is critical in this HCCI engine to assess whether it contains sufficient heat energy to supply an appropriate heated inlet air temperature through a heat exchange device and, at the same time, to convert both HC and CO emissions in a conventional three-way catalytic converter. Exhaust temperature estimation is performed using a nonlinear equation, which is mainly function of m_f, T_{ivc}, and W_{ivc} such that

$$T_2 = (\sigma_1 m_f + \sigma_2) + \sigma_3 \Delta T_{ivc,0} + \sigma_4 \Delta W_{ivc,0}, \tag{3.7}$$

where $\Delta T_{ivc,0} = T_{ivc} - T_{ivc,ref}$ and $\Delta W_{ivc,0} = W_{ivc} - W_{ivc,ref}$. All the coefficients in (3.7) are determined as $\sigma_1 = \sigma_{11}N + \sigma_{12}$, $\sigma_3 = \sigma_{31}N + \sigma_{32}m_f + \sigma_{33}$ and $\sigma_4 = \sigma_{41}N + \sigma_{42}m_f + \sigma_{43}$. Note that $T_{ivc,ref}$ and $W_{ivc,ref}$ correspond the values for a operating condition with a wide open hot throttle ($\theta_h = 100\%$) and a completely closed cold throttle ($\theta_c = 0\%$) while other

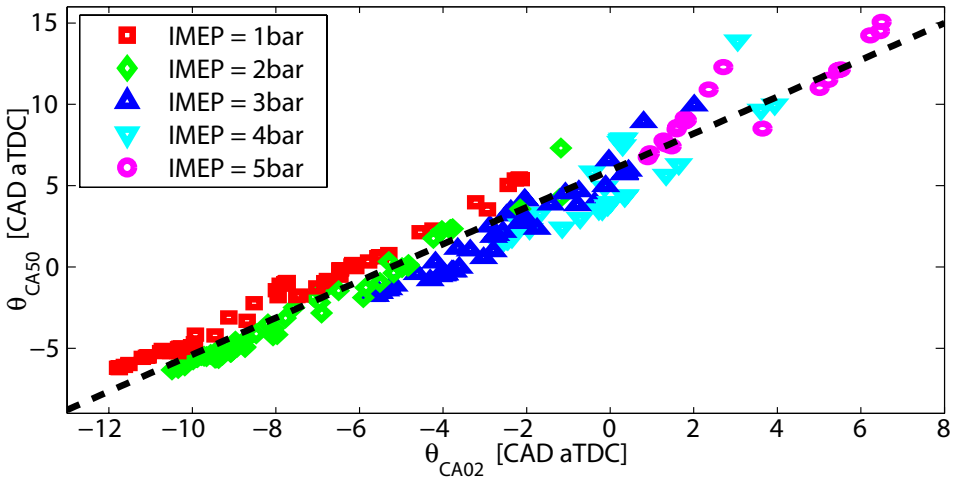

Figure 3.4 θ_{CA02} versus θ_{CA50} from dynamometer test.

engine inputs are identical.

3.2.5 Prediction Error with Steady State Data

The steady state HCCI dynamometer engine experiments were performed with several planned mapping points for given engine speed, load, hot air temperature, hot throttle angle and cold throttle angle. The fuel rate and the hot inlet temperature were altered simultaneously and judiciously up until operation was not feasible due to too fast combustion, misfires or high covariance of IMEP. The steady state HCCI engine test region for various load conditions at the engine speeds of 1000, 1500, and 2500 RPM is shown in table 3.1. Each test was performed with 1) hot throttle sweep while the cold throttle was completely closed and 2) cold throttle sweep while the hot throttle was wide open.

Table 3.2 presents the mean, μ, standard deviation, σ, minimum and maximum values of the prediction error, which is determined by the difference between the steady state dynamometer engine test data and estimation using HCCI MVM (i.e. $x_{dyno} - \hat{x}_{sim}$, where x is the output values for each engine operating condition). It indicates that, in general, the HCCI Mean Value Model (MVM) has good prediction capability and Fig. 3.6 represents the overall comparisons of the engine key outputs such as $IMEP$, AFR, θ_{CA02}, θ_{CA50} and T_2. Black solid and dashed line indicate the mean and standard deviation of prediction error, respectively. Note that ”hot” and ”cold” in the legend from Fig. 3.6 denote the experimental data for the hot and cold throttle sweep cases at each engine speed.

Table 3.1 Summary of steady-State HCCI dynamometer engine experiment with various cold and hot throttle angles.

Speed [RPM]	Steady State Operating Conditions				
1000	Fuel Rate [mg/cycle] (IMEP [bar])				
	6.4 (1.2)	8.6 (2)	11.8 (3)	15 (4)	18.2 (5)
	Hot Inlet Temperature [°C]				
	225	210	160	130	105
1500	Fuel Rate [mg/cycle] (IMEP [bar])				
	6.2 (1.2)	8.6 (2)	11.8 (3)	15 (4)	18.2 (5)
	Hot Inlet Temperature [°C]				
	220	200	150	120	100
2500	Fuel Rate [mg/cycle] (IMEP [bar])				
	6.4 (1.4)	8.6 (2)	11.8 (3)	15 (4)	18.2 (5)
	Hot Inlet Temperature [°C]				
	210	220	150	-	-

Table 3.2 Mean (μ), standard deviation (σ), Min and Max values of the model prediction error.

	Prediction Error			
	Mean (μ)	STD (σ)	Min	Max
$IMEP$ [bar]	0.00004	0.1565	-0.4651	0.3463
AFR	0.1322	0.7027	-2.0096	1.9828
θ_{CA02} [CAD aTDC]	0.2058	0.8414	-3.8908	3.7695
θ_{CA50} [CAD aTDC]	0.1923	1.6770	-4.5792	6.9796)
θ_{comb} [CAD aTDC]	0.2003	1.9232	-5.1117	7.3290)
T_2 [°C]	0.1280	10.2222	-37.6140	23.7234

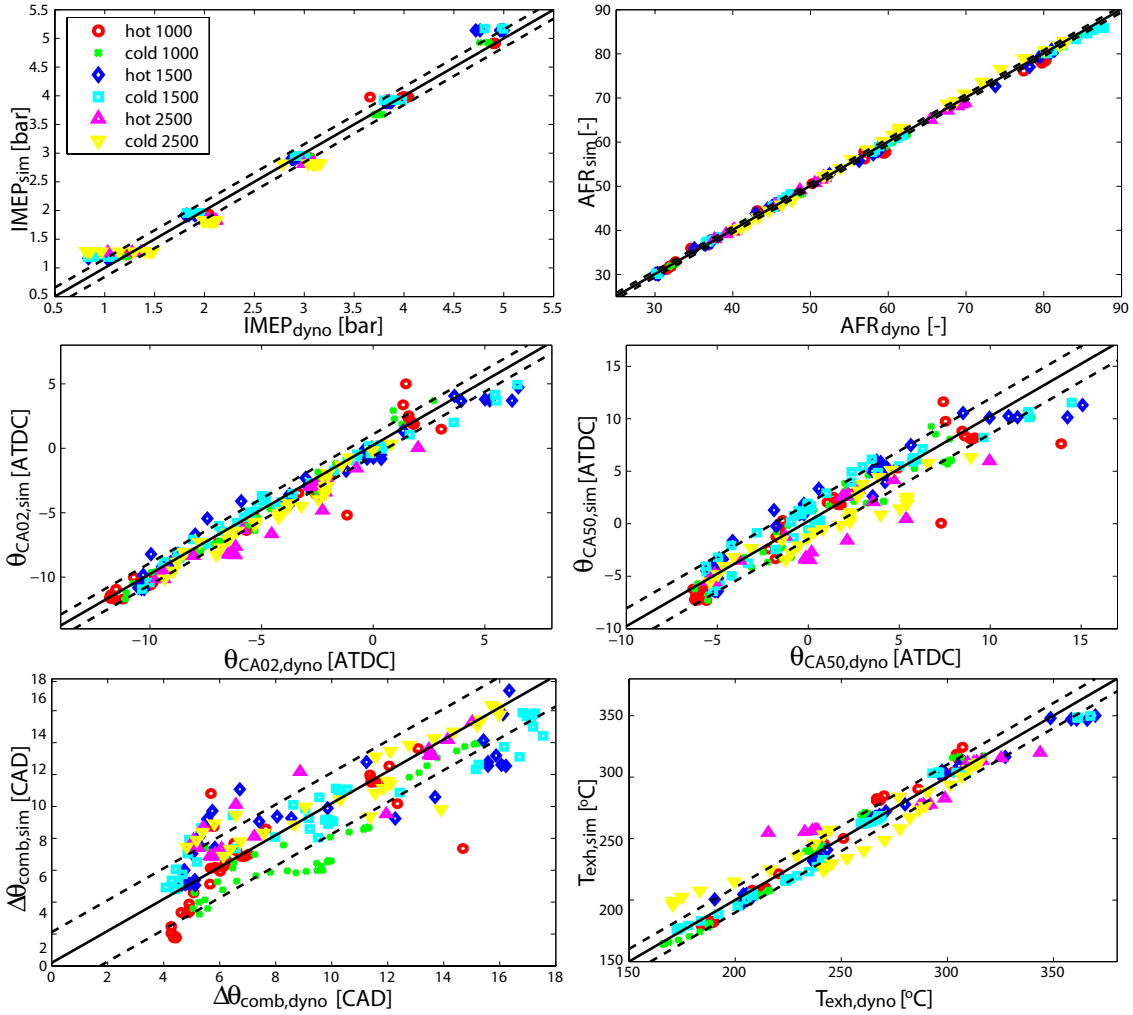

Figure 3.5 Comparison of $IMEP$, AFR, θ_{CA02}, θ_{CA50}, $\Delta\theta_{comb}$, and T_2 between the dynamometer engine test and the model simulation for different engine speeds, loads and throttle angles.

3.2.6 Validation with Transient Data

Three different transient tests were performed for the single cylinder HCCI engine: 1) load step changes (Fig. 3.6(a)), 2) hot throttle step changes (Fig. 3.6(b)), and 3) cold throttle step changes (Fig. 3.6(c)). Blue dashed lines show the dynamometer test data and red solid lines display the MVM simulation results. The HCCI MVM in general predicts the single cylinder engine variables with considerable accuracy. In IMEP comparison, for instance, the model captures the dynamometer engine performance with a maximum deviation of approximately 0.2 bar. Decreasing θ_h and increasing θ_c cause slight IMEP drops, which can be explained by $\Delta\theta_{comb}$ changes in the next section. Both measured and simulated θ_{CA50} match in both the magnitude and direction of changes with a maximum deviation

of 3 CAD. The model does not capture the observed lag of θ_{CA50} after fuel step applied in Fig. 3.6(a), which exhibits a first order response with a time constant of 1 second. We postulate that the cylinder wall thermal dynamics are also needed in the model to fully capture this behavior as shown in [73, 74, 29]. The cylinder wall temperature measurement, critical for the cylinder thermal dynamics, however, was not available for this heated-air inlet HCCI engine system. Unlike θ_{CA50} measurement, $\Delta\theta_{comb}$ from the dynamometer test has no lagged response for load step changes and captured by simulation. Note that the noise level of measured $\Delta\theta_{comb}$ differs for each experimental data sets since the cylinder pressure measurement had different measurement noise levels.

3.3 Combustion Duration Control

The control strategy in the heated air intake HCCI engine is to manage hot and cold throttles to achieve good combustion timing (high fuel efficiency and high combustion stability) while engine operating condition changes (i.e. engine speed and load changes). Combustion timing has been detected with some reference values, for instance, the location of in-cylinder peak pressure, $Loc\ p_{peak}$, and/or the crank angle of 50% fuel burned ,θ_{CA50}, which might vary for different engine speeds and loads. Therefore, the set point of combustion timing reference needs to be scheduled based on load (or fueling level) and speed to achieve the same objectives. The lift of a secondary opening of the exhaust valve, known as the rebreathing valve lift (RBL) was controlled to regulate θ_{CA50} [75]. The variable valve actuator (in specific, intake valve closing (IVC) and exhaust valve closing (EVC)) was managed to achieve a desired location of in-cylinder peak pressure $Loc\ p_{peak}$ and in-cylinder peak pressure p_{peak} [71]. The combustion phase θ_{CA50} was regulated by the intake valve closing (IVC) and the fast thermal management (FTM) system, which controls the intake manifold temperature using both the hot throttle actuator and the heater power [29]. A similar FTM method utilizing a cold throttle with fixed hot throttle actuator was also conducted to regulate θ_{CA50} on a multi-cylinder Variable Compression Ratio (VCR) engine [72]. In this section, we propose a new possible proxy of engine performance variable, $\Delta\theta_{comb}$, which can represent both combustion stability and fuel efficiency in terms of covariance of IMEP and ISFC.

The steady state dynamometer test of the HCCI engine shows that regulating $\Delta\theta_{comb}$ might be a better control objective than θ_{CA50} for the heated inlet air HCCI engine. Two plots of the first raw in Fig. 3.7 show the covariance of $IMEP$ and normalized $ISFC$ with respect to the combustion duration for various loads and engine speeds. These plots in-

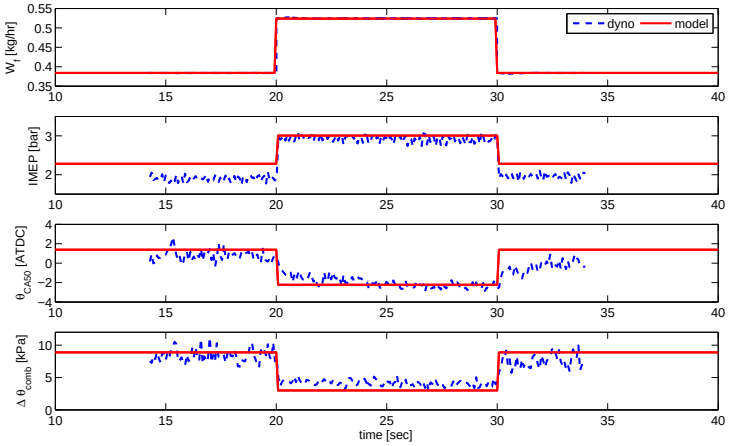

(a) Load step changes (θ_c = 0%, θ_h = 100%, T_0 = 39°C, T_h = 157°C, N = 1500 rpm).

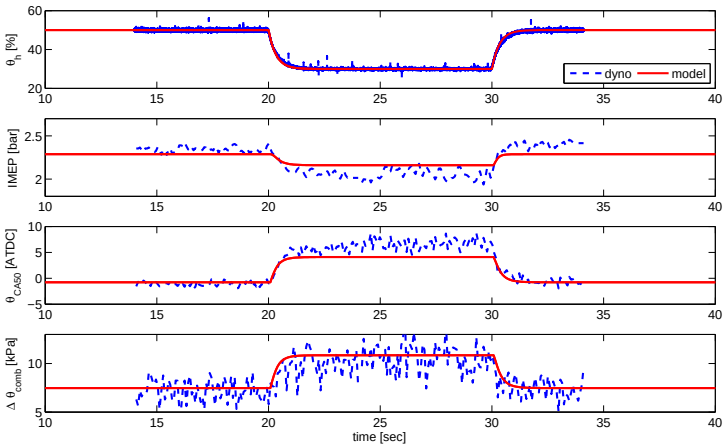

(b) Hot throttle step changes (θ_c = 0%, θ_h = 50% → 30% → 50%, T_0 = 43°C, T_h = 185°C, N = 1500 rpm).

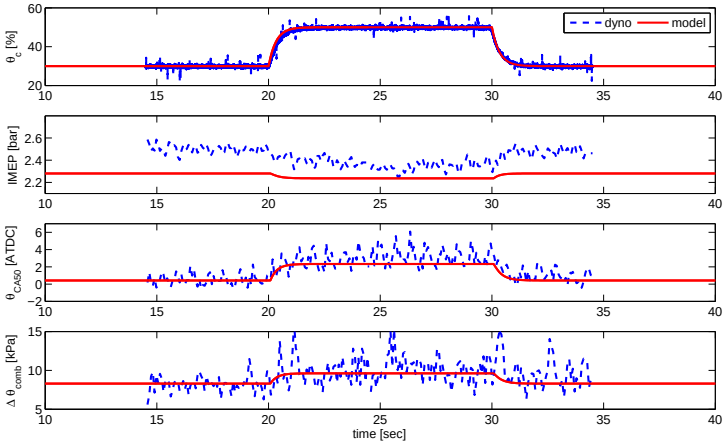

(c) Cold throttle step changes (θ_c = 30% → 50% → 30%, θ_h = 100%, T_0 = 34°C, T_h = 176°C, N = 1500 rpm).

Figure 3.6 Model validation with the load, hot and cold throttle step changes of the single cylinder HCCI engine at N = 1500 rpm.

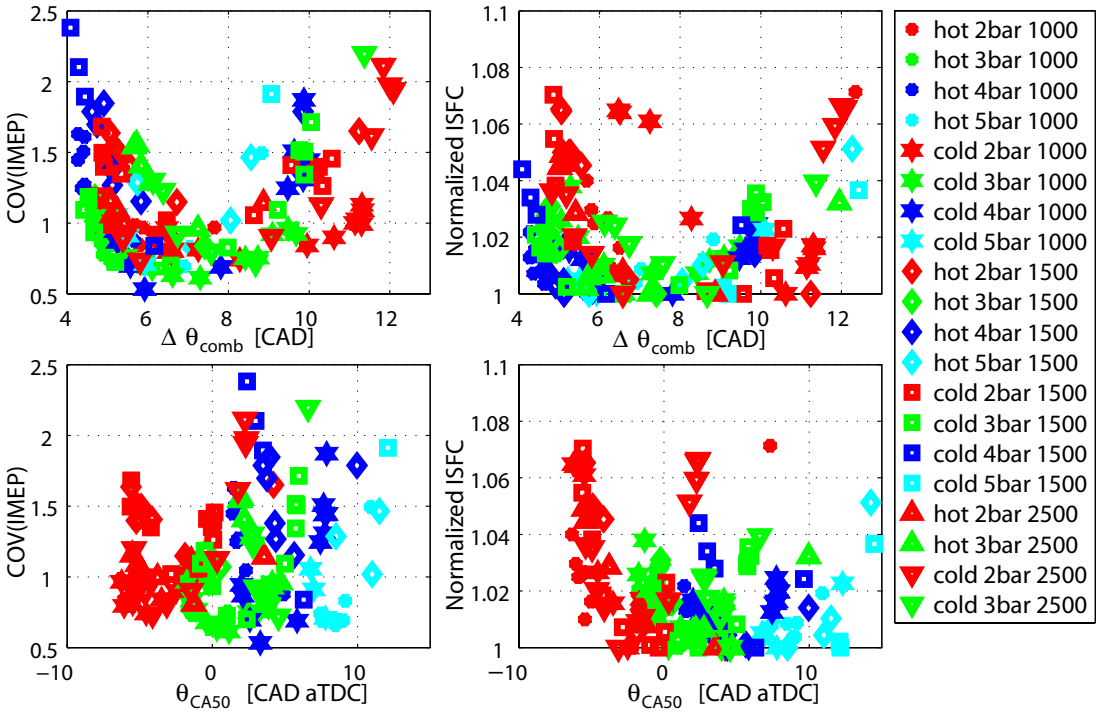

Figure 3.7 Comparison between $\Delta\theta_{comb}$ and θ_{CA50} with respect to covariance of IMEP and normalized ISFC.

dicate that the heated inlet HCCI engine, in general, is able to achieve both high engine combustion stability and high fuel efficiency if $\Delta\theta_{comb}$ is regulated at about 7.5 [CAD] for all different engine speeds and loads. On the other hand, the optimal θ_{CA50} varies mainly for different loads and changes for different speeds considerably as depicted in two plots of the second column in Fig. 3.7. For instance, θ_{CA50} has to be much lower than the typical 4 CAD target to get good covariance of IMEP and ISFC, even though the 4 CAD target begins to be acceptable as the load increases. Therefore, a set point map as a function of load and speed might be required to choose θ_{CA50} as the combustion timing reference values for both optimal fuel efficiency and combustion stability [19].

To account for this phenomenological behavior of IMEP and ISFC, a statistical function for the covariance of IMEP $COV(IMEP)$ and a equation for the combustion efficiency η_{comb} are derived based on the combustion duration $\Delta\theta_{comb}$ as following,

$$COV(IMEP) = f_{cov}(\Delta\theta_{comb}), \tag{3.8}$$

$$\eta_{comb} = f_{\eta}(\Delta\theta_{comb}), \tag{3.9}$$

where f_{cov} and f_{η} are second order polynomials, in specific, $f_{cov}(\Delta\theta_{comb}) = \xi_1\Delta\theta_{comb}^2 +$

$\xi_2 \Delta\theta_{comb} + \xi_3$ and $f_\eta(\Delta\theta_{comb}) = \varphi_1 \Delta\theta_{comb}^2 + \varphi_2 \Delta\theta_{comb} + \varphi_3$, respectively.

It seems to be physically reasonable that a certain level of $\Delta\theta_{comb}$ is desired for both fuel efficiency and combustion stability. For instance, if $\Delta\theta_{comb}$ increases, which leads to lower P_{peak} or misfire, then the engine start losing feasibility of combustion. On the other hand, if $\Delta\theta_{comb}$ becomes smaller, which induces higher P_{peak}, then the continuity of combustion decreases such that overall work capability gets smaller. More analysis of this combustion behavior under the inlet air heated conditions are necessary for more accurate explanation. Based on the observation here, we design a simple controller in the following section.

3.4 Control Analysis and Design

Due to two throttle actuators (cold and hot intake throttles) to regulate one control objective values ($\Delta\theta_{comb}$), this HCCI engine can be considered as an overactuated system (i.e. two-input and single-output (TISO) system). For instance, if a engine cycle needs more (or less) heat energy, then either hot throttle angle can be increased (or decreased) or cold throttle angle can be decreased (or increased). Overactuating the HCCI engine provides a certain amount of redundancy for closed-loop combustion control, however, a proper control allocation might be necessary to have a unique solution to an overactuated problem. One possible way to do this is the allocation process introduced in this section.

3.4.1 Desired Cold and Hot Throttle Settings

In overactuated system, many optimum values of actuators can be found to produce the same system output. In this engine, for instance, various combinations of cold and hot throttle angles (θ_c and θ_h) can be the optimum values to achieve a desired combustion duration $\Delta\theta_{comb}^{des}$. Based on the previous discussion, assume that the desired combustion duration is equal to 7.5 crank angle degrees (i.e. $\Delta\theta_{comb}^{des}$ = 7.5 CAD). Fig. 3.8 shows the optimal cold and hot throttle angles ($\theta_{c,opt}$ and $\theta_{h,opt}$) to achieve the combustion duration $\Delta\theta_{comb}^{des}$ equal to be 7.5 CAD for different loads and hot inlet air temperatures at the engine speed of 1500 RPM. Note that blue, green and red color lines indicate different hot inlet air temperatures with 140, 150 and 160 ^oC respectively. Upper triangular, lower triangular and square marked lines represent different fuel injection rates per cycle as depicted.

It can be observed in Fig. 3.8 that increasing hot inlet air temperature T_h allows more cold throttle angle open while hot throttle angle remains at the same levels to regulate the combustion duration for each load. Increasing load level decreases the optimal hot throttle

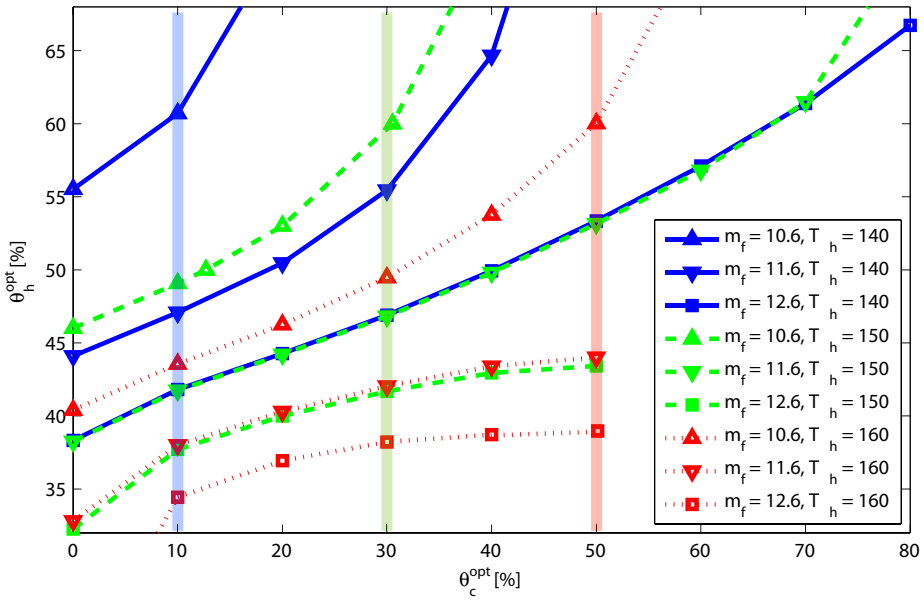

Figure 3.8 Optimal cold and hot throttle angles (θ_c^{opt} and θ_h^{opt}) to achieve a desirable combustion duration, $\Delta\theta_{comb}$ = 7.5 CAD, for different loads m_f [mg/cycle] and hot inlet temperatures T_h [^{o}C] at the engine speed of 1500 rpm.

angles for each hot inlet air temperature. Blue, green and red solid lines show possible cold throttle angles with hot throttle open from 35 to 60 %. Hence, wide open cold throttle condition can be allowed for higher load operating region with similar hot throttle actuator range. Note that HCCI engine can only run up to approximately 5 IMEP bars and mode switching to spark ignition (SI) is required beyond this load limit. At the boundary between HCCI and SI combustion mode, therefore, it might be preferred to have less hot throttle open and wide open cold throttle since SI combustion mode does not require heated inlet air.

3.4.2 SISO System and Linearization

If we assume that the hot inlet air temperature change is relatively slower than the load changes, the cold throttle actuator can be determined by a feedforward controller (or mapping) based on the heated inlet air temperature. This assumption allows us to have a single-input and single-output (SISO) system control problem, in which the system redundancy can be eliminated. There might be several control strategies and one standard method is introduced here, feedforward plus proportional and integral feedback controller. This controller is tuned using linear techniques. First of all, linearization is performed around a fueling level m_f = 11.6 mg/cycle, and nominal control inputs θ_c = 30 % and θ_h

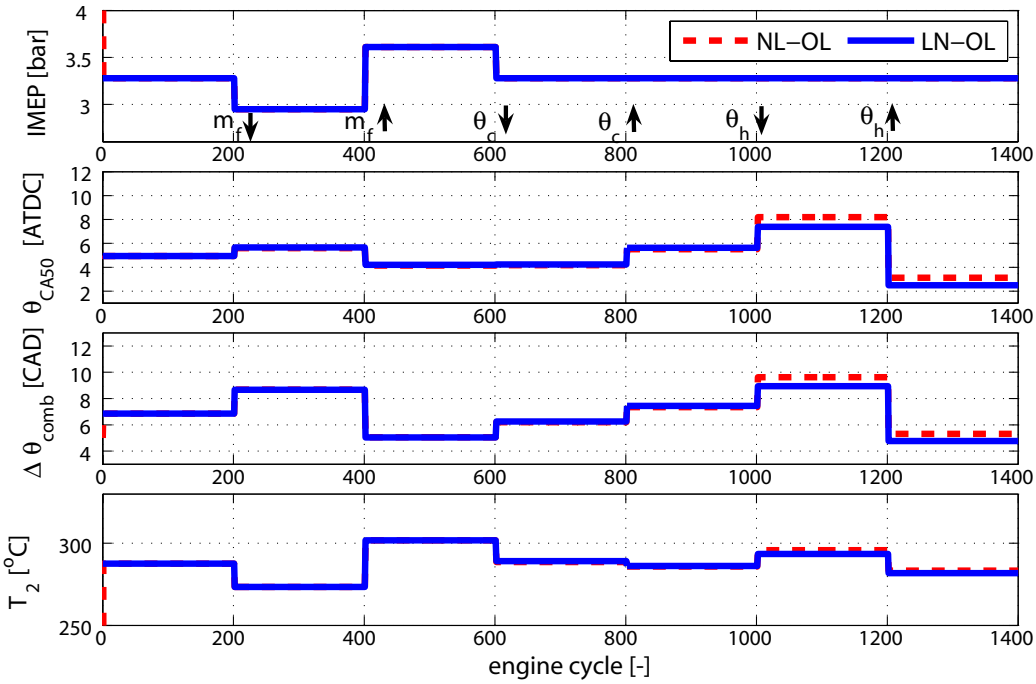

Figure 3.9 Open loop response of the linearized and nonlinear model during step changes of engine inputs.

= 47 % such that the desired combustion duration $\Delta\theta_{comb}$ = 7.5 CAD is achieved and a corresponding difference equation is realized as

$$\delta\Delta\theta_{comb}(k+1) = K_h\delta\theta_h(k) + K_c\delta\theta_c(k) + K_f\delta m_f(k) + K_t\delta T_h(k), \qquad (3.10)$$

where K_h, K_c, K_f, and K_t indicate constant numbers. Fig. 3.9 shows the open loop responses of the linearized and nonlinear model for fuel, θ_c and θ_h steps. The simulation shows the fuel steps m_f = 11.6 $\rightarrow$ 10.6 $\rightarrow$ 12.6 $\rightarrow$ 11.6 mg/cycle at 200, 400 and 600 engine cycle. Next, cold throttle steps θ_c = 30 $\rightarrow$ 20 $\rightarrow$ 40 $\rightarrow$ 30 % are applied at 600, 800 and 1000 engine cycle. Finally, hot throttle steps θ_h = 47 $\rightarrow$ 37 $\rightarrow$ 57 % are applied at 1000 and 1200 engine cycle. The step responses indicate that the linearized model can represent locally the nonlinear HCCI engine model. The hot throttle actuator has bigger dynamic control authority than the cold throttle actuator at the nominal values. Based on this linearized model, a feedforward compensator plus proportional and integral (PI) feedback controller is designed in the following section.

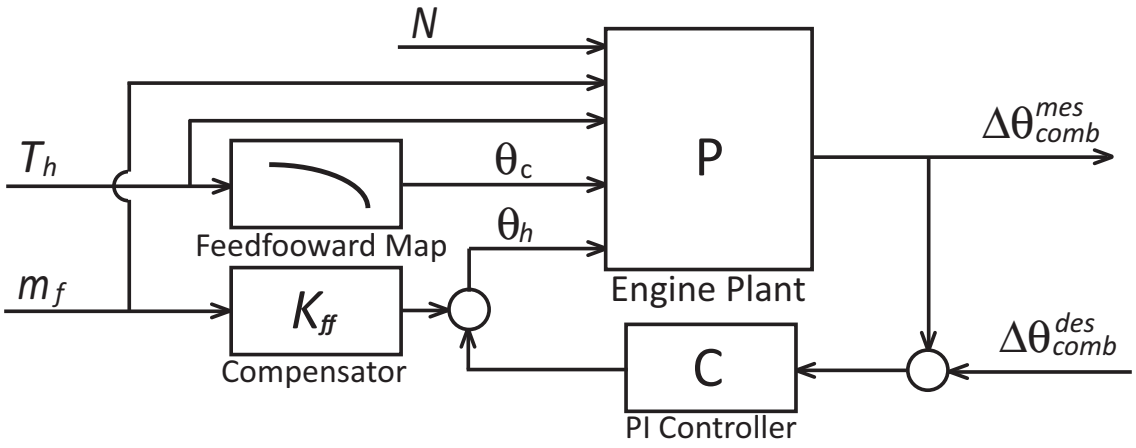

Figure 3.10 Block diagram of feedforward and PI feedback control system.

3.4.3 Feedforward plus PI Feedback Control

Fig. 3.10 shows the block diagram of SISO HCCI engine with a feedforward compensator and PI feedback controller. The control signal $u(k)$ is then determined as

$$u(k) = K_{ff}\delta m_f(k) - K_P\delta\Delta\theta_{comb}(k) - K_I\sum\delta\Delta\theta_{comb}(k), \tag{3.11}$$

where K_{ff}, K_P, and K_I presents feedforward, feedback proportional, and feedback integral controller gains. A cancelation feedforward controller can be derived from two system gains

$$K_{ff} = -K_h^{-1}K_f, \tag{3.12}$$

where K_h and K_f are from (3.10). Two feedback control gains K_P and K_I are selected based on linear quadratic regulator (LQR) method with an augmented integrator state. Fig. 3.11 shows the comparison of system response with and without control. Note that it is assumed, during this simulation, that there exists a uniformly distributed random measurement noise with a maximum of 2 CAD and a minimum of -2 CAD. Also, the heated inlet air temperature is fixed at T_h = 423K such that no cold throttle command is applied during this simulation (i.e. θ_c = 30%). From the bottom three plots in Fig. 3.11, we observe that the the feedforward and feedback controller improve the fuel efficiency and, at the same time, the covariance of IMEP gets slightly smaller than one without combustion duration regulation.

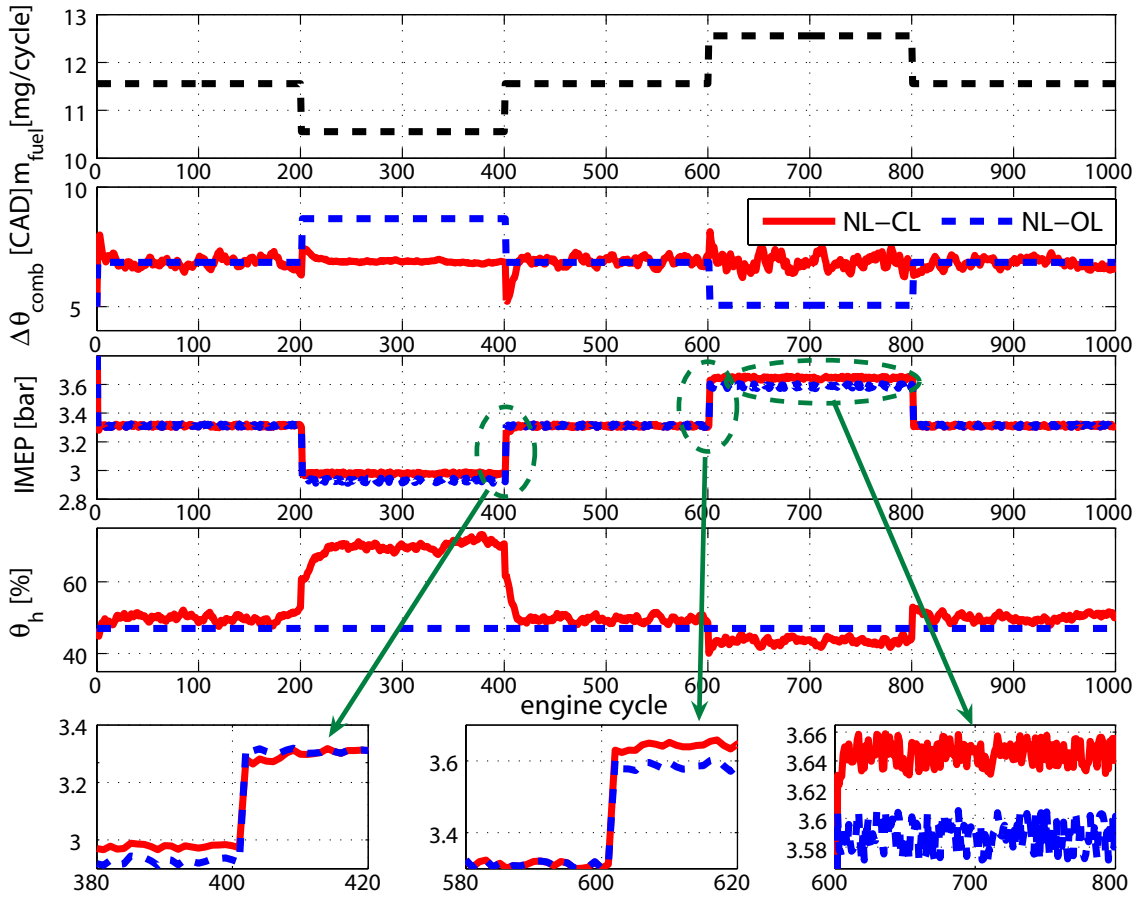

Figure 3.11 Comparison between nonlinear open loop (NL-OL) and closed loop (NL-CL) with Feedforward + Integral controller.

3.4.4 Heated Inlet Air Temperature Changes

We now consider a simple heat exchanger model, which affects the heated inlet air temperature as shown in Fig. 3.12. We assume that the heat exchanger effectiveness is about 0.47 and the heat capacity rates (i.e. mass flow rate multiplied by specific heat) for hot and cold air stream are same. A simple lag with a time constant of 4 seconds is assumed for the heat exchanger. An affine relation is implemented for the cold throttle actuator command such that the hot throttle moves around the same operating region with one used in Fig. 3.11. Note that this affine relation between heated inlet air temperature and cold throttle is necessary to be modified with a nonlinear map if we extend the fuel range to cover the entire potential HCCI load and speed range.

Fig. 3.13 compares the MVM responses for both hot throttle (feedforward and PI feedback) and cold throttle (feedforward) control with a heat exchanger (HEX) versus hot throttle (feedforward and PI feedback) control only with hot inlet air temperature fixed.

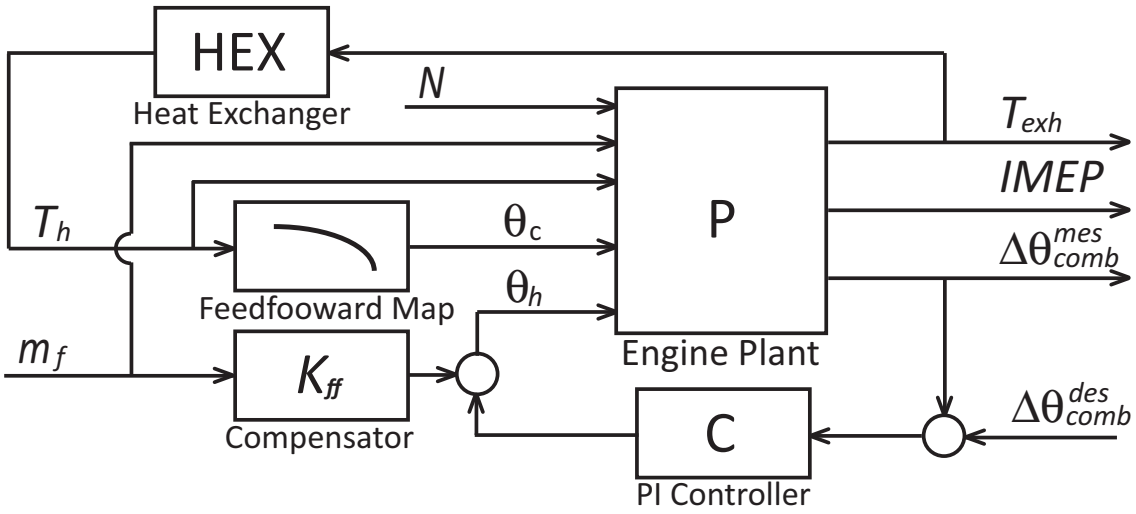

Figure 3.12 Block diagram of feedforward and PI feedback control system with a heat exchanger.

As can be expected from Fig. 3.8, hot throttle control inputs remains at the same operating range while cold throttle manages to compensate the heated inlet air temperature changes. Hence the decoupling methodology with the proposed actuator allocation seem to be promising. Similar comparison for the crank-angle resolved model [53] responses is shown in Fig. 3.14 with same control strategies.

3.5 Conclusion

In this chapter, we introduce a simple statistical physics based HCCI MVM including a cycle delay and validate the model with both steady state and transient test data sets. We then investigate an appropriate control objective, which represents engine performance, and find that the combustion duration, $\Delta\theta_{comb}$, might be a surrogate control objective for both combustion stability and fuel efficiency. Since the HCCI engine has two actuators (cold and hot throttles) and one control objective $\Delta\theta_{comb}$, the allocation of actuators is performed based on the assumption that the heated inlet air temperature varies slowly through a heat exchanger dynamics and the two actuators can be decoupled such that cold throttle manages slow hot inlet air temperature changes with a feedforward controller while hot throttle mainly manages the load disturbances using cycle-to-cycle combustion duration measurement.

Based on the allocation of two actuators, a simple model based controller using a linear control technique is designed to manage the hot throttle actuator to regulate the combustion duration at 7.5 CAD during load transients. Feedforward compensator and PI feedback

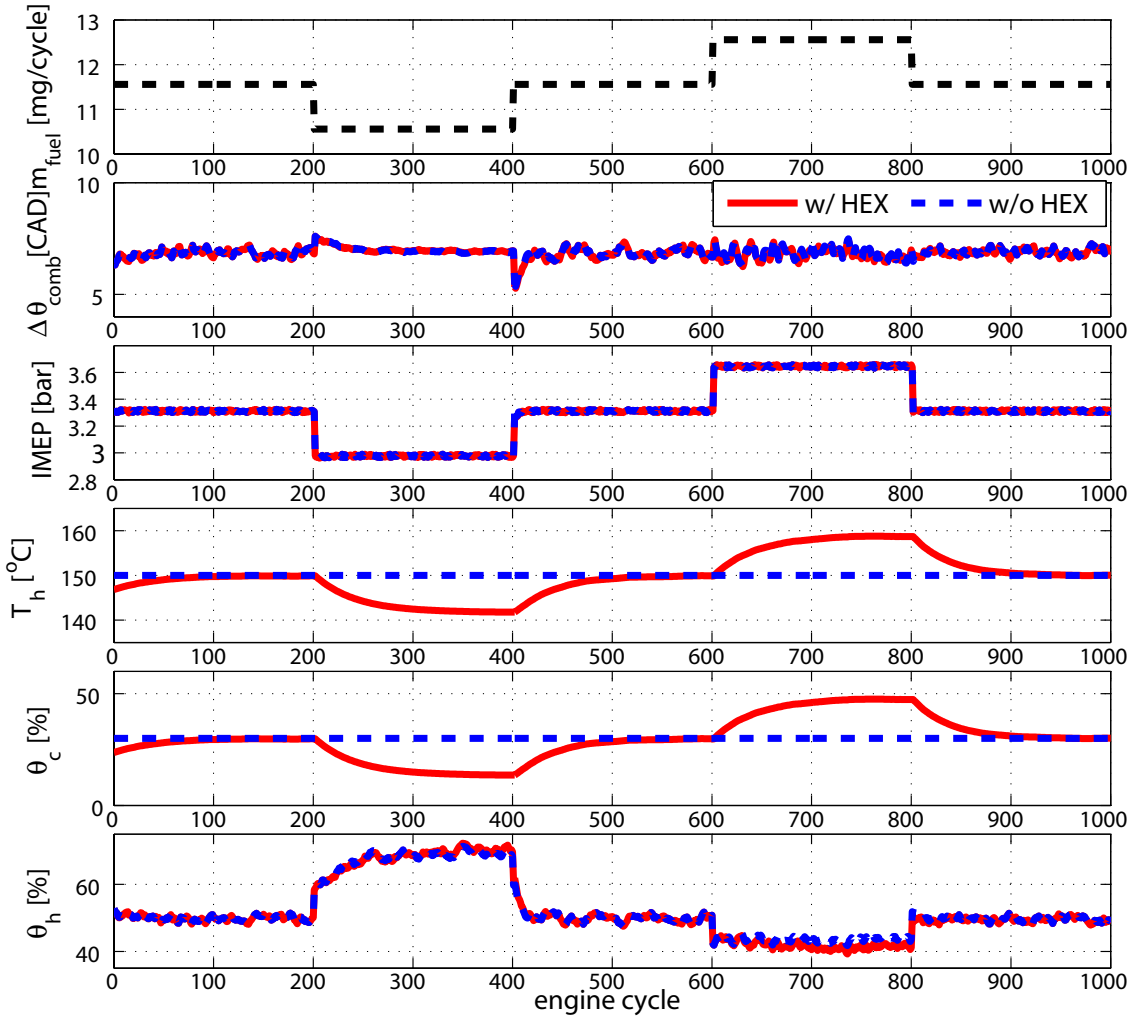

Figure 3.13 Mean value model responses with and without a heat exchanger model and cold throttle feedforward map.

controller together shows good regulation responses of $\Delta\theta_{comb}$ to achieve higher IMEP and smaller covariance of IMEP. A simple heat exchanger with the effectiveness of 0.47 and a lag is implemented and, from the simulation result, it can be verified that the proposed coordination of two actuators is appropriate.

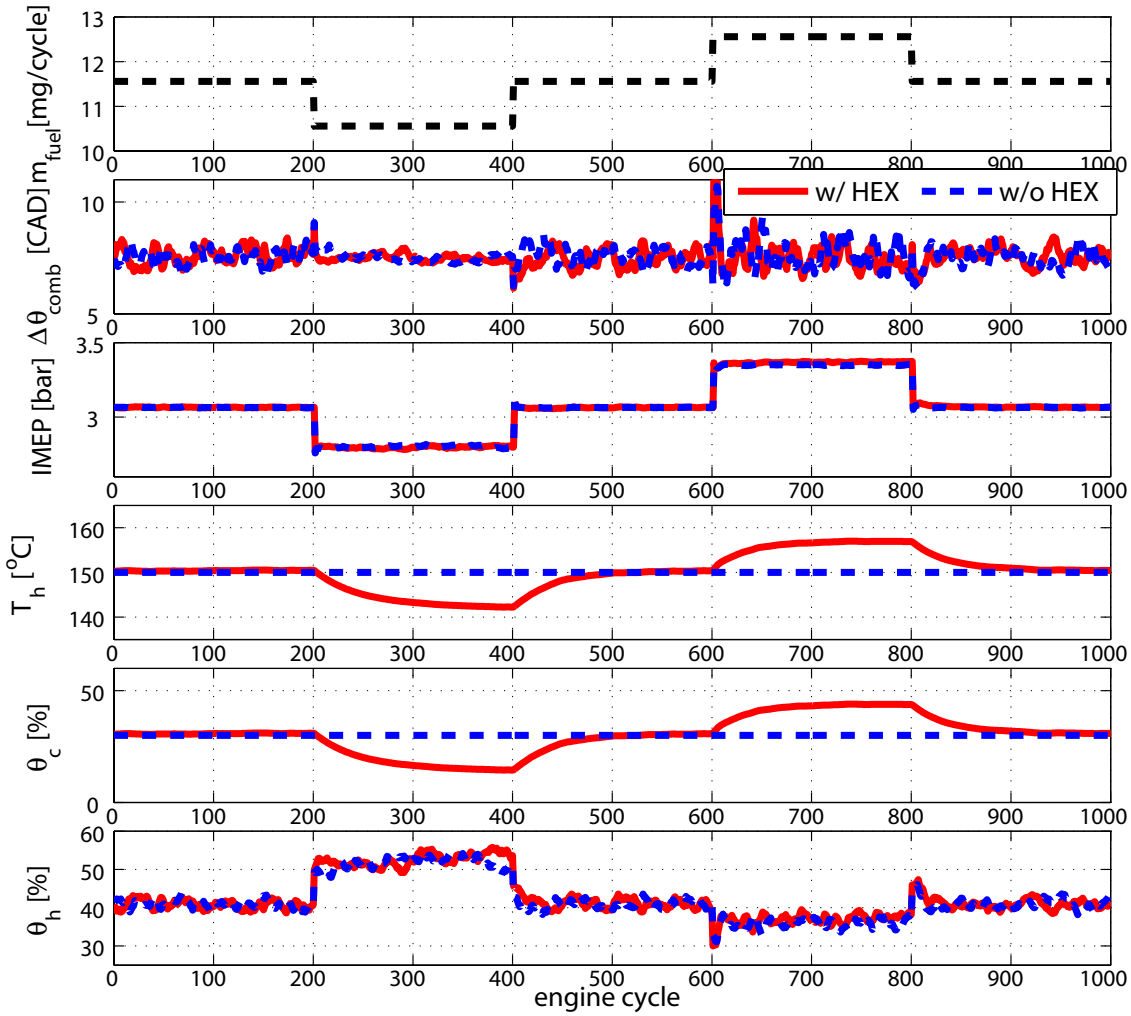

Figure 3.14 Crank-angle based model responses with and without a heat exchanger model and cold throttle feedforward map.

Chapter 4

Air Charge Control for Turbocharged Spark Ignition Engines with Internal Exhaust Gas Recirculation

4.1 Introduction

We present in this chapter an effort to minimize the detrimental effects of high levels of exhaust gas recirculation (EGR) in the drivability of a turbocharged Spark Ignition Direct Injection (SIDI) engine equipped with dual cam phasing capability. In such an engine platform, the throttle, the turbocharger wastegate, and the Variable Valve Timing (VVT) overlap system are three actuators in the air path system for the control of cylinder charge. The VVT system with variable camshafts allows flexible valve overlap, hence, enables high level of internal EGR (iEGR), which, if there is no combustion stability problem, typically reduces fuel and NOx emissions.

The selection of a performance variable is not as straightforward because one has to take into account its ability to represent the overall performance objectives (e.g., efficiency, emissions, drivability) and its ability to correlate with the available measurements. This chapter focuses on improving the transient response of cylinder charge flow rate during tip-ins and tip-outs via the use of a compensator added on the base throttle signal. This compensator, called valve compensator, minimizes the deleterious effects of valve overlap changes on cylinder air flow. Therefore, the work presented here can be applied over part-load and lightly boost operation conditions when the wastegate remains passive[1].

A control-oriented model for the target engine system is first developed and parameterized with dynamometer measurements collected over a wide range of operation conditions and various gasoline-ethanol fuel blends. Developed based on the model in [47], the en-

[1]The duty cycle of the turbocharger wastegate is set to zero so that its opening is govern by the spring force, exhaust gas back-pressure, and boost pressure.

gine model consists of a mean value model to simulate the cycle-average behavior of the air-path system and a discrete event model to capture the particular behavior during each stroke (i.e., intake, compression, combustion/expansion, exhaust). As presented in Section 4.2, the parameterized engine model is able to predict the dynamic engine behavior with gasoline and ethanol fuels up to E85 (85% ethanol and 15% gasoline in volume). The static VVT scheduling scheme that takes various engine performance variables (e.g., efficiency, emission, combustion stability) into consideration is described in Section 4.3. In Section 4.4, the dynamic interaction between the throttle and the valve overlap and their transient effects on the intake manifold pressure and cylinder charge is analyzed. Then, the valve compensator is designed to improve the transient behaviors of cylinder charge during tip-ins and tip-outs when the VVT system transits from one set-point position to other as commanded by the static VVT schedule. As shown in the simulation and experimental results, the use of feedforward throttle compensators can significantly improve the transient cylinder charge response. Finally, a summary is following in Section 4.6.

4.2 Control-Oriented Model and Validation

This work develops a model on the basis of the one presented in [47] that follows the principles of mass and energy conservation and the Newton's second law for turbocharger dynamics. The schematic in Fig. 4.1 shows the 7 states, namely, two states for the boost pressure p_b and temperature T_b; two states for the intake manifold pressure p_{im} and temperature T_{im}; two states for the exhaust manifold pressure p_{ex} and temperature T_{ex}; one state for the turbocharger connecting shaft rotational speed N_{tc}. In this section, only the modifications from the original model in [47] are discussed, which are the modeling of cylinder charge flow rate (also known as engine pumping rate) and the state reduction of exhaust manifold temperature following an isothermal assumption. For details of the model, please refer to [47].

Based on dynamometer measurements, the mass air flow rate into the cylinder W_{cyl} can be modeled as a function of intake manifold pressure p_{im}, engine speed N, and intake and exhaust valve overlap v

$$W_{cyl} = F(p_{im}, N, v) = \alpha_1(N, v)p_{im} + \alpha_2(N, v), \tag{4.1}$$

where α_1 and α_2 are polynomials in N and v. Fig. 4.2 shows that W_{cyl} can be modeled as a linear function of p_{im} while α_1 and α_2 depend on N and v. It should be noted that the behavior of the VVT system in this turbocharged engine is more complex than what has

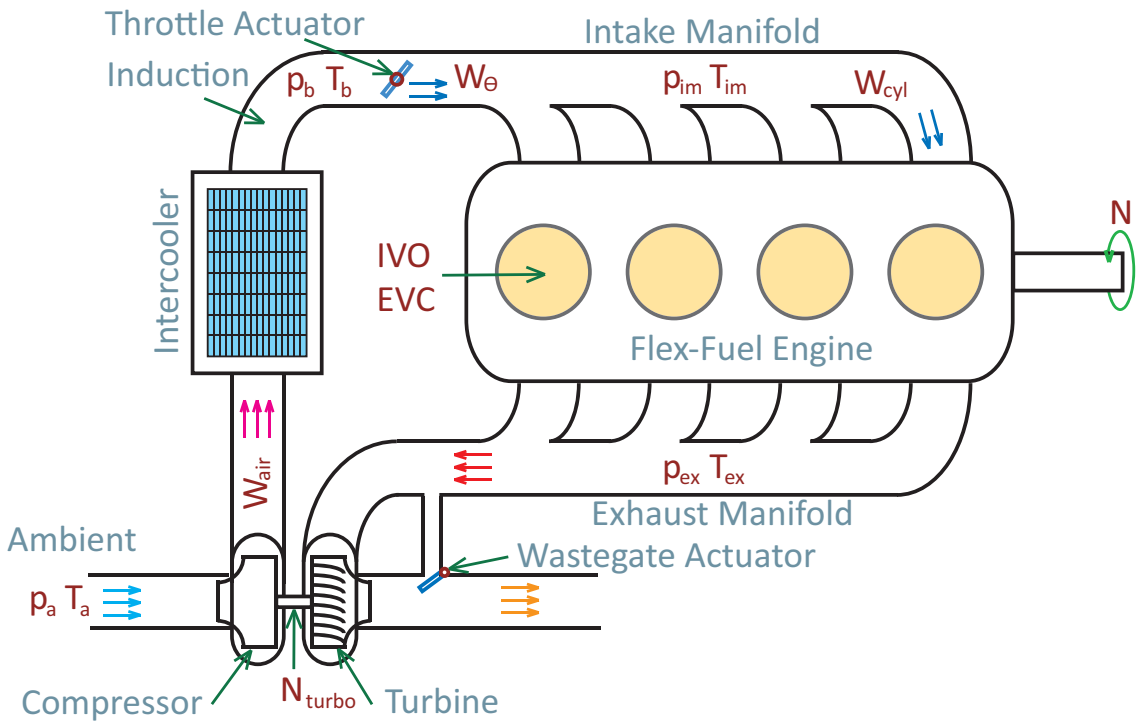

Figure 4.1 Schematic of turbocharged spark ignition direct injection engine equipped with variable intake and exhaust camshafts.

been observed and documented in the Naturally Aspirated (NA) Spark Ignition (SI) engine. As shown in Fig. 4.2, when the intake manifold pressure is lower than the atmosphere pressure (i.e., $p_{im} < 1 \ \ bar$), an increased valve overlap decreases the fresh charge flow rate in the cylinders, which has been observed in the conventional NA SI engine. However, when the intake manifold pressure is higher than the atmosphere pressure (i.e., $p_{im} > 1 \ \ bar$), an increased valve overlap increases the cylinder charge flow rate. Note that the tested engine used for the parameterized model in this chapter has a dual-independent VVT system, but we only consider a positive valve overlap associated with symmetric intake valve opening (IVO) and exhaust valve closing (EVC) with respect to top dead center (TDC).

Simulation results have suggested that the isothermal assumption is acceptable for the modeling of exhaust manifold dynamics

$$\frac{dp_{ex}}{dt} = \frac{RT_{ex}}{V_{ex}}(W_{in} - W_{out}), \tag{4.2}$$

where R and V_{ex} denote the ideal gas constant and the exhaust manifold volume, respectively. $T_{ex} = T_{bd}$ is the blowdown temperature which is modeled based on an ideal isochoric combustion of the injected fuel followed by an isentropic expansion. The heat generated

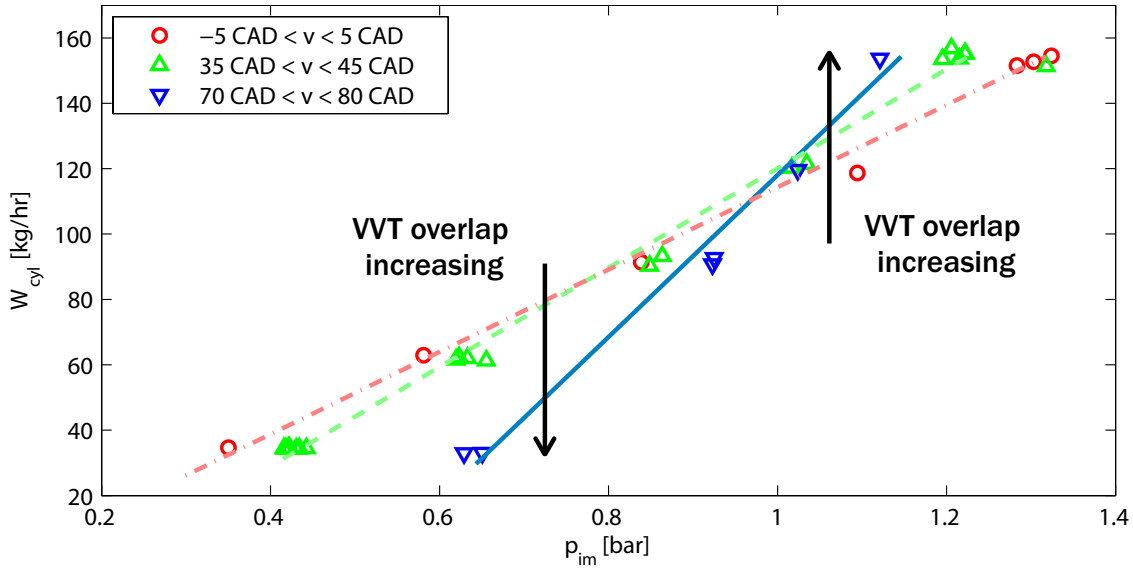

Figure 4.2 Cylinder pumping flow W_{cyl} versus intake manifold pressure p_{im} with various intake and exhaust valve overlaps v at N = 2000 RPM.

during combustion depends on the low heating value and quantity of the fuel [47].

The model has been parameterized using steady-state dynamometer measurements for gasoline fuel from 800 RPM up to 4500 RPM with various control set-points for throttle angle, wastegate duty cycle, fuel injection and spark angle, positions of IVO and EVC, and fuel rail pressure. The parameterized mean-value model captures the transients with reasonable accuracy for both fuels: gasoline (E0) and fuel with 85% volumetric ethanol content (E85). Validation of the transient behavior during a step change in the throttle angle is shown in Fig. 4.3 and 4.4 for E0 and E85, respectively.

Subplots of the first column in Fig. 4.3 and 4.4 show the engine model inputs, and those of the second column allow a direct comparison between the predicted (red solid lines) and measured engine outputs (blue dashed lines). At 2000 RPM for E0 both the measured and predicted outputs show undershoots in the boost pressure, p_b, and overshoot in the air flow rate through the compressor, W_{air}. As shown in Fig. 4.4, the model also captures the undershoot in boost pressure, p_b, caused by a throttle angle change at 2500 RPM for E85.

4.3 Static Schedule of VVT

In this section, a static schedule for the intake and exhaust valve overlap is proposed to achieve maximum iEGR at medium load, stable combustion at low load, and maximum

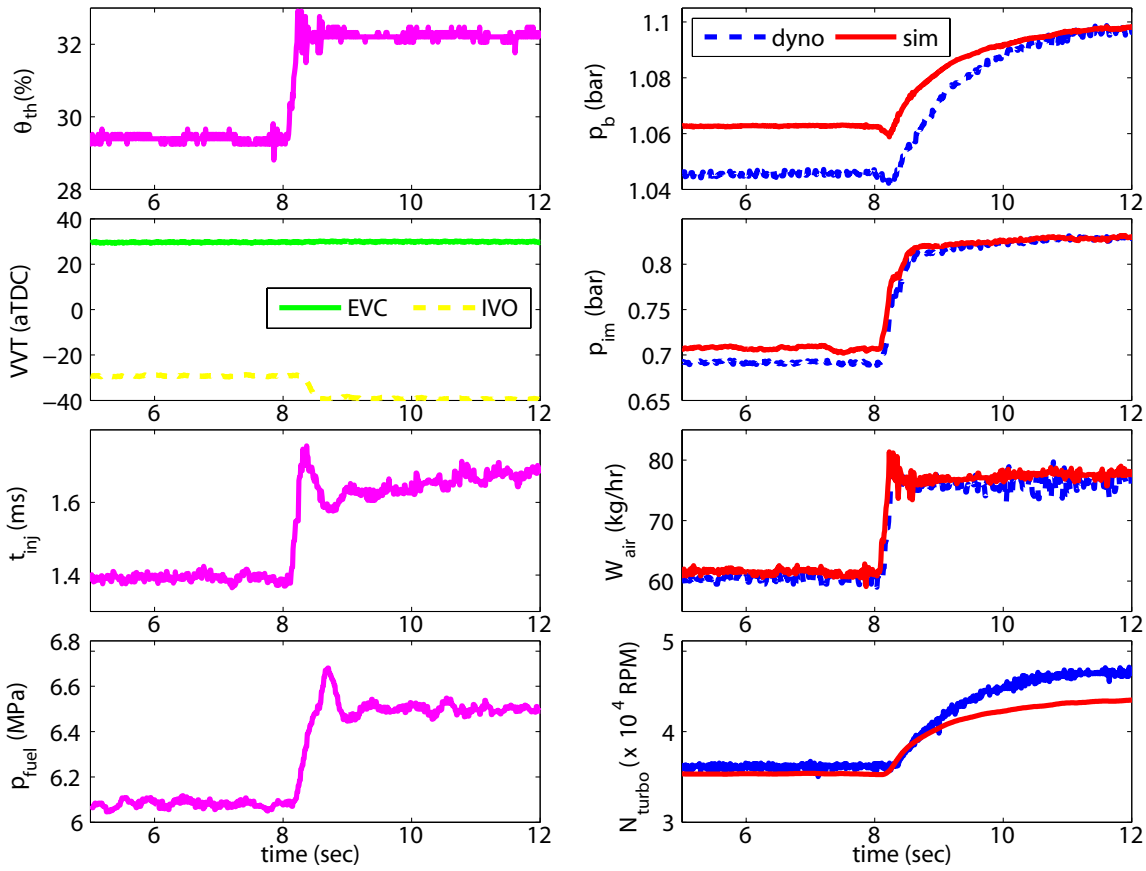

Figure 4.3 Comparison between dynamometer measurement and model simulation for throttle step change with E0 fuel and a fixed wastegate duty cycle at 0% at N = 2000 RPM; dynamometer engine inputs are presented in the first column and corresponding engine outputs (blue dashed lines) are compared with simulation results (red solid lines) in the second column.

torque at high load [40]. Since the electronic throttle is the actuator that has the most control authority over cylinder charge at part-load and lightly-boosted conditions, the static valve overlap is scheduled with respect to the throttle angle.

In Fig. 4.5, the plots of the first and second row show the steady-state cylinder charge flow rate, W_{cyl}, and intake manifold pressure, p_{im}, with respect to the throttle angle, θ_{th}, at three valve overlap values(i.e., v = 0, 40, 80 CAD). The cylinder charge flow rate at different valve overlap values are approximately same at low load with $\theta_{th} < 20\%$. At medium load with $20\% < \theta_{th} \leq 40\%$, the cylinder charge flow rate decreases with an increased valve overlap. At high load with $\theta_{th} > 40\%$, however, the cylinder charge flow rate increases with an increased valve overlap at a given throttle angle.

It is important to note that at low throttle valves, during small downstream-to-upstream pressure ratio p_{im}/p_b, when flow through the throttle body occurs at sonic conditions, over-

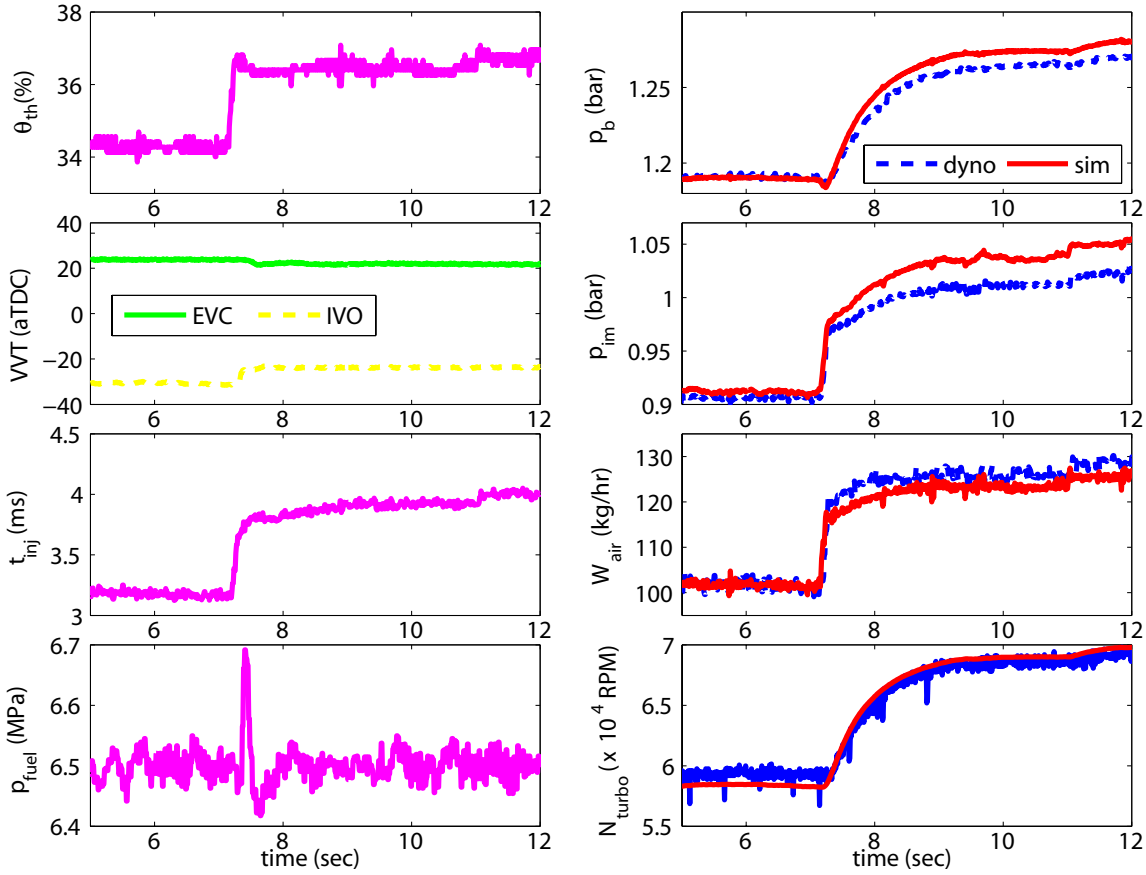

Figure 4.4 Comparison between dynamometer measurement and model simulation for throttle step change with E85 fuel and a fixed wastegate duty cycle at 0% at N = 2500 RPM; dynamometer engine inputs are presented in the first column and corresponding engine outputs (blue dashed lines) are compared with simulation results (red solid lines) in the second column.

lap does not affect the steady-state cylinder air flow but it has detrimental effect as can be seen in Fig. 4.6. This zero DC gain, yet strong transient influence of the overlap on flow arises from the inlet manifold filling dynamics with p_{im} adjusting to higher values as overlap increases as shown in Fig. 4.5 (second subplot).

Two overlap scheduling schemes, denoted as v_{egr} and v_{air}, are shown in the third subplot in Fig. 4.5. One scheduling scheme for v_{egr} is derived to achieve maximum iEGR level subject to stable combustion at low load and maximum torque at high load; 1) near idle engine conditions ($\theta_{th} < 20\%$), VVT overlap is scheduled to be zero for idle combustion stability 2) at high loads ($\theta_{th} \geq 40\%$) near WOT, the overlap is set to be 80 CAD such that W_{cyl} can be maximized, and 3) for part loads, overlap is selected to achieve the maximum iEGR with a smooth transition between v = 0 CAD and v = 80 CAD at the throttle range of $20\% \leq \theta_{th} < 40\%$. Apart from v_{egr}, a reference valve overlap defined as v_{air} in Fig. 4.5 is

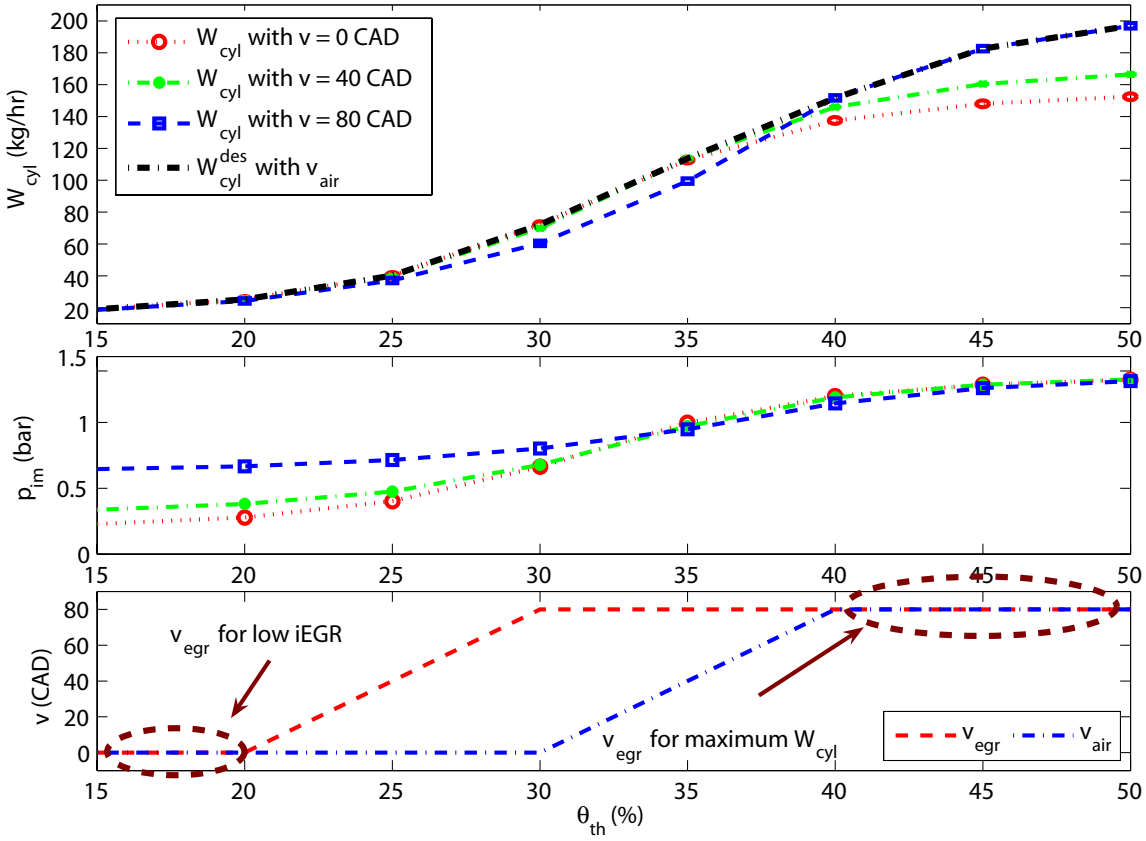

Figure 4.5 Cylinder pumping flow rate W_{cyl} and intake manifold pressure p_{im} with respect to throttle angles θ_{th} for various intake and exhaust valve overlaps v and corresponding VVT overlap scheduling scheme v at N = 2000 RPM.

determined to maximize cylinder air flow rate given throttle angle. This desired maximum cylinder flow rate W_{cyl}^{des} (black dashed line) is presented in the first plot in Fig. 4.5. Based on the two different overlap scheme, v_{egr} and v_{air}, a model-based throttle compensator that reduces the deleterious effect of overlap changes on cylinder air flow will be discussed in the next section.

4.4 Valve Compensator Design

A valve compensator with an electronic throttle for a NA throttled engine is designed in [41] to remove or reduce the effect of the VVT transients on the cylinder charge, in which θ_{th}^{*} is employed as a virtual actuator. The effects of step changes in valve overlap on the cylinder charge flow rate at throttle angles of 20% and 40% are simulated and illustrated in Fig. 4.6. The valve overlap increase at lightly boosted conditions when $p_{im} > 1$ *bar* and

$\theta_{th} = 40\%$ leads to the transition to an increased steady-state cylinder charge flow rate, as observed in Fig. 4.2. The same step change in valve overlap at part load conditions when $p_{im} < 1$ *bar* and $\theta_{th} = 20\%$, however, leads to the transitions with large overshoots and undershoots with no steady-state cylinder flow rate change. The valve compensator design, presented in [41] for a NA engine, is modified here to compensate for these deleterious valve overlap transients.

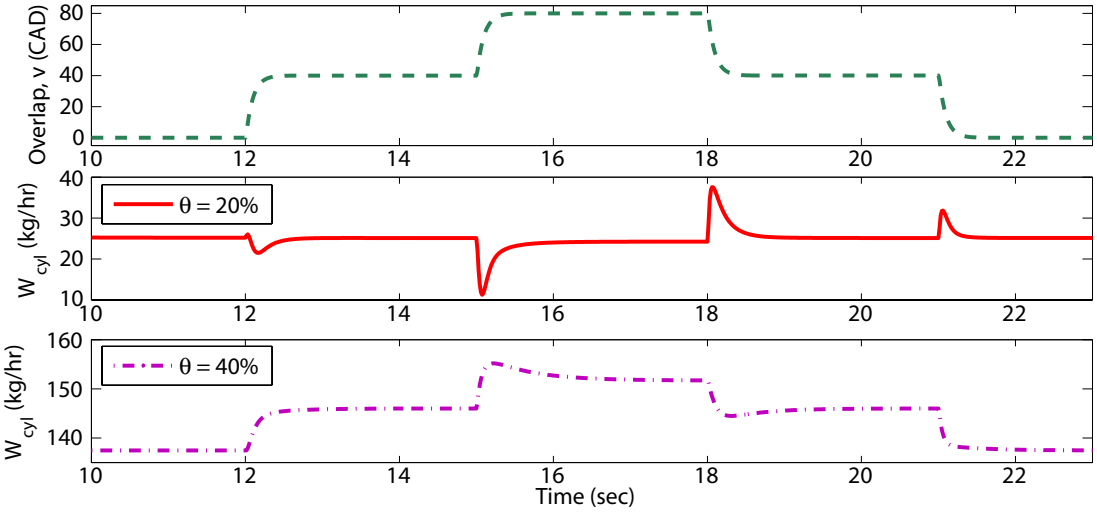

Figure 4.6 Cylinder air charge rate W_{cyl} response of the turbocharged engine on VVT overlap v step changes; engine speed is 2000 RPM and throttle is fixed at θ_{th} = 20% (second plot) and θ_{th} = 40% (third plot).

The compensator design also takes into account the fact that the boost pressure, p_b, varies at different engine speeds and loads in a turbocharged engine. Here, the intake manifold pressure p_{im}, boost pressure p_b, engine speed N, and overlap v are considered available from measurements. Moreover, to further simplify the engine model for the compensator design, the intake manifold is assumed to be isothermal so that the state of intake manifold temperature, T_{im}, can be eliminated.

$$\dot{p}_{im} = K_{im}\left(W_\theta - W_{cyl}\right), \tag{4.3}$$

such that first order dynamics can be used for the compensator design with the throttle air flow determined by

$$W_\theta = g_1(\theta_{th}, p_b) g_2(p_{im}/p_b), \tag{4.4}$$

$$\text{where } g_1 = A_e(\theta_{th})\frac{p_b}{\sqrt{RT_{im}}}$$

$$g_2 = \begin{cases} \sqrt{\frac{\gamma}{\gamma+1}\left(\frac{2}{\gamma+1}\right)^{\frac{1}{\gamma-1}}} & \text{if } \frac{p_{im}}{p_b} \le r_c \\ \sqrt{\frac{\gamma}{\gamma-1}\left(\left(\frac{p_{im}}{p_b}\right)^{\frac{2}{\gamma}} - \left(\frac{p_{im}}{p_b}\right)^{\frac{\gamma+1}{\gamma}}\right)} & \text{if } \frac{p_{im}}{p_b} > r_c \end{cases}$$

with $K_{im} = RT_{im}/V_{im}$, and T_{im} and V_{im} correspond to the intake manifold pressure and volume, respectively. $A_e(\theta_{th})$ indicates effective cross section area and $r_c = (2/(\gamma+1))^{\gamma/(\gamma-1)}$ denotes critical pressure ratio, which draws a distinction between sonic and subsonic flows. Additionally, the VVT actuator mechanism dynamics are modeled by

$$\dot{v}_{egr}^{act} = \frac{1}{\tau_{VVT}}\left(v_{egr} - v_{egr}^{act}\right), \quad \tau_{VVT} = 0.09sec. \tag{4.5}$$

Here, the time constant $\tau_{VVT} = 0.09$ *sec* is selected to capture the VVT system dynamics at an engine speed for 2000 RPM.

The throttle angle is the primary control variable in a turbocharged engine for accomplishing the torque demanded by the driver at part load and lightly boosted conditions. Here θ_{th} is defined as the base throttle signal issued in response to a driver's torque demand. Then, a compensation angle θ_{th}^* is introduced in addition to the base throttle signal θ_{th} in order to reduce the deleterious effects of valve overlap transitions on the cylinder charge flow rate. At a fixed or slowly varying engine speed, the compensation angle θ_{th}^* is selected so that the effects of the valve overlap transition on the cylinder charge flow rate change, $\dot{W}_{cyl}$, is compensated, and the associated cylinder charge flow rate, W_{cyl}, matches as much as possible the desired steady-state cylinder charge flow rate, W_{cyl}^{des}, as a result of the static valve overlap schedule v_{air} for maximum torque. From (4.1), we get $\dot{W}_{cyl} = \left(\frac{\partial \alpha_1}{\partial v} p_{im} + \frac{\partial \alpha_2}{\partial v}\right)\dot{v} + \alpha_1 \dot{p}_{im}$. Therefore, when the static valve overlap schedule for optimized iEGR, v_{egr}, is used, the rate of change of cylinder air flow $\dot{W}_{cyl}(N, v_{egr}^{act})$ is given by

$$\begin{aligned} \dot{W}_{cyl}\Big|_{v_{egr}} &= \alpha_1(N, v_{egr}) K_{im}\left(g_1(\theta_{th} + \theta_{th}^*, p_b) g_2(p_{im}/p_b) - W_{cyl}\right) \\ &\quad + \left(\frac{\partial \alpha_1}{\partial v}\Big|_{N, v_{egr}} p_{im} + \frac{\partial \alpha_2}{\partial v}\Big|_{N, v_{egr}}\right) \dot{v}_{egr}^{act}, \end{aligned} \tag{4.6}$$

For details of static VVT schedule v_{egr} and v_{air}, please refer to Section 4.3 and Fig. 4.5.

It is desirable to have the $\dot{W}_{cyl}\big|_{v_{egr}}$ follow the the rate of cylinder air flow rate associated to the "best torque" static v_{air} schedule $\dot{W}_{cyl}\big|_{v_{air}}$ when the overlap schedule is performed

infinitely slowly (v_{air}^{∞}) so that it does not have any impact on the transient torque responses

$$\dot{W}_{cyl}\Big|_{v_{air}^{\infty}} = \dot{W}_{cyl}^{des} = \alpha_1(N, v_{air}) K_{im} \left(g_1(\theta_{th}, p_b) g_2(\tilde{p}_{im}/p_b) - W_{cyl}^{des} \right), \tag{4.7}$$

where $\tilde{p}_{im}$ is a fictitious reference manifold pressure derived only with the throttle θ_{th} and engine speed N,

$$\dot{\tilde{p}}_{im} = K_{im}(g_1(\theta_{th}, p_b) g_2(\tilde{p}_{im}/p_b) - W_{cyl}). \tag{4.8}$$

Based on the assumption that $\frac{\partial W_{cyl}}{\partial p_{im}}\big|_{v_{egr}} \simeq \frac{\partial W_{cyl}}{\partial p_{im}}\big|_{v_{air}}$ which can be verified from Fig. 4.5, it follows that $\alpha_1(N, v_{egr}) \simeq \alpha_1(N, v_{air})$ and $\alpha_1(N, v_{egr}) W_{cyl}\big|_{v_{egr}} \simeq \alpha_1(N, v_{air}) W_{cyl}\big|_{v_{air}} = \alpha_1(N, v_{air}) W_{cyl}^{des}$. With these two approximations we can solve for θ_{th}^* using (4.6) = (4.7)

$$\theta_{th}^* = g_1^{-1}\left(C_1 \dot{v}_{egr}^{act} + C_2\right) - \theta_{th}, \tag{4.9}$$

$$\text{where } C_1 = -\frac{\frac{\partial \alpha_1(N, v_{egr}^{act})}{\partial v} p_{im} + \frac{\partial \alpha_2(N, v_{egr}^{act})}{\partial v}}{K_{im} \alpha_1(N, v_{egr}^{act}) g_2(p_{im}/p_b)} \text{ and}$$

$$C_2 = \frac{g_2(\tilde{p}_{im}/p_b)}{g_2(p_{im}/p_b)} g_1(\theta_{th}, p_b).$$

4.5 Simulation and Experiment during Tip-Ins and Tip-Outs

The valve compensator designed in the previous section has been tested for a engine mean-value model validated in Section 4.2 and also implemented in a 2.0 L 4 cylinder turbocharged vehicle engine with VVT. The block diagram for the throttle based compensator for the VVT turbocharged engine is illustrated in Fig. 4.7. Based on the measurement of the boost pressure p_b and intake manifold pressure p_{im} along with the engine speed N and base throttle angle θ_{th} (commanded through a pedal position by a driver), the valve overlap compensator block generates the throttle compensation signal θ_{th}^* to reduce a deleterious effect of the VVT transients on the cylinder pumping flow rate.

Valve overlap step changes have been applied to the mean-value model first for a fixed engine speed of 2000 RPM and a fixed throttle position of 20 % as shown in Fig. 4.8. Note that the first subplot shows the valve overlap step changes. Blue dashed lines and red solid lines from the second and third subplots indicate the cylinder pumping flow rate and throttle

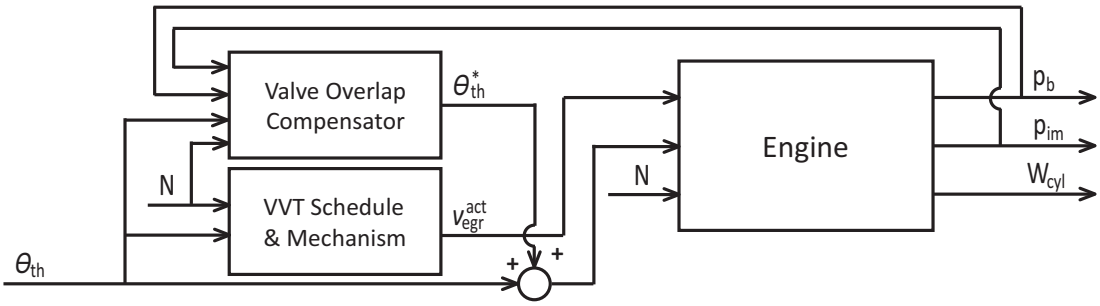

Figure 4.7 Schematic diagram of VVT turbocharged engine with valve compensator.

angle with and without the valve compensation signal θ^*_{th}, respectively. Overshoots (or undershoots) of the electronic throttle position generated by the valve compensator during the valve overlap step-ups (or step-downs) reduce the undesired undershoots (or overshoots) on the cylinder pumping flow rate.

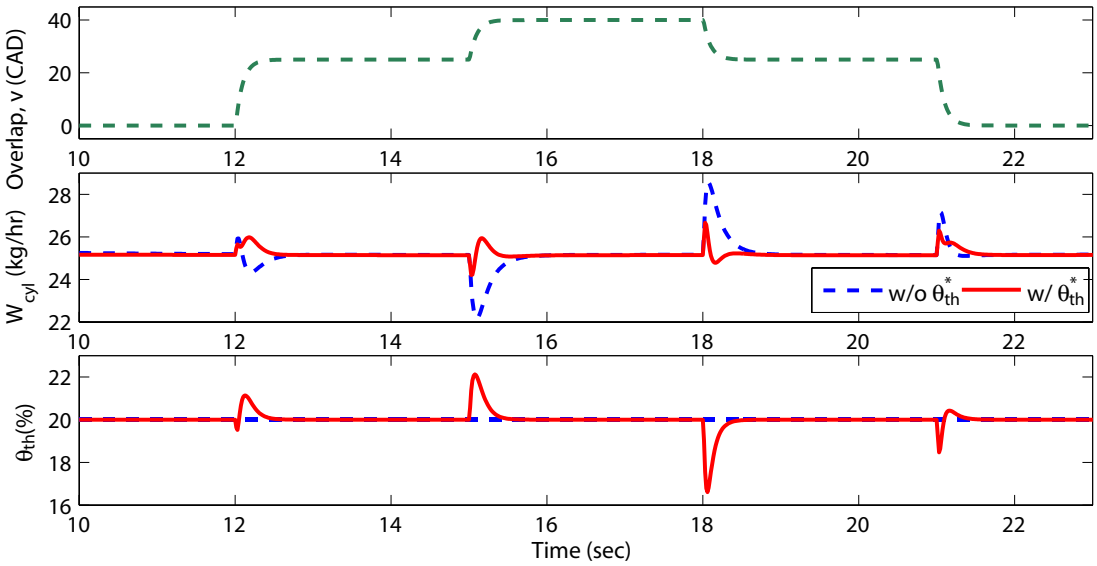

Figure 4.8 Comparison of the cylinder pumping flow during the valve overlap step changes with (red solid lines) and without (blue dashed lines) the valve compensator θ^*_{th} : both engine speed and base throttle position are fixed at N = 2000 RPM and θ_{th} = 20 %. (**Simulation**)

The algorithm was implemented in the engine control unit (ECU) of a a 4 cylinder turbocharged SI engine vehicle on a chassis dynamometer facility. Comparison of relative load (RL) is shown in Fig. 4.9. RL is normally defined in percentage as the estimated cylinder pumping flow and corresponding engine power output. The values over 100% in RL mean that the engine is running at wide-open throttle and that the air flow is being boosted by the turbocharger. Note that overlap step changes were applied from 20 to 40 CAD and 40 to 20 CAD at 12.5 seconds and 14.5 seconds, respectively, and the data shows similarity

with simulation.

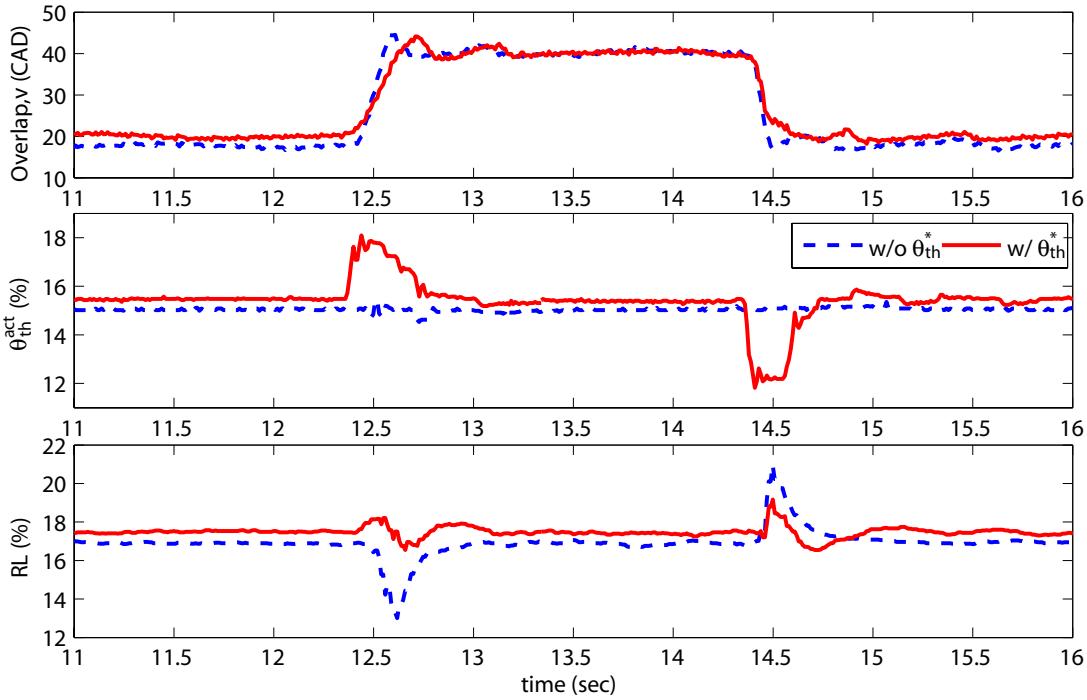

Figure 4.9 Comparison of relative road *RL* during the valve overlap step changes with (red solid lines) and without (blue dashed lines) the valve compensator θ_{th}^{*} : both engine speed and base throttle position are fixed at N = 2000 RPM and θ_{th} = 15 %. (**Experiment**)

The nonlinear engine model with the adiabatic inlet manifolds validated in Section 4.2 is used for a comparison of the cylinder air charge flow rate W_{cyl} in the VVT turbocharged engine with and without the compensation θ_{th}^{*} during throttle (load) step changes as shown in Fig. 4.10. All simulations are performed under the assumption that the fuel injectors and spark ignition are controlled properly such that the engine operates at stoichiometric AFR (14.6) and Maximum Brake Torque (MBT) conditions for a given cylinder charge flow rate. Throttle step changes are introduced while the engine speed N is fixed at 2000 RPM and the static VVT schedule v_{egr} is selected given throttle angle and engine speed. The compensated throttle input θ_{th}^{*} is shown in the second subplot of Fig. 4.10 as the difference between the blue dashed line and the red solid line. The use of the compensated throttle angle clearly improves the transient response of W_{cyl} during throttle step changes at low loads (i.e., θ_{th} = 20% $\rightarrow$ 22.5% $\rightarrow$ 25%) by accelerating the transition of cylinder charge flow rate to a new steady-state value.

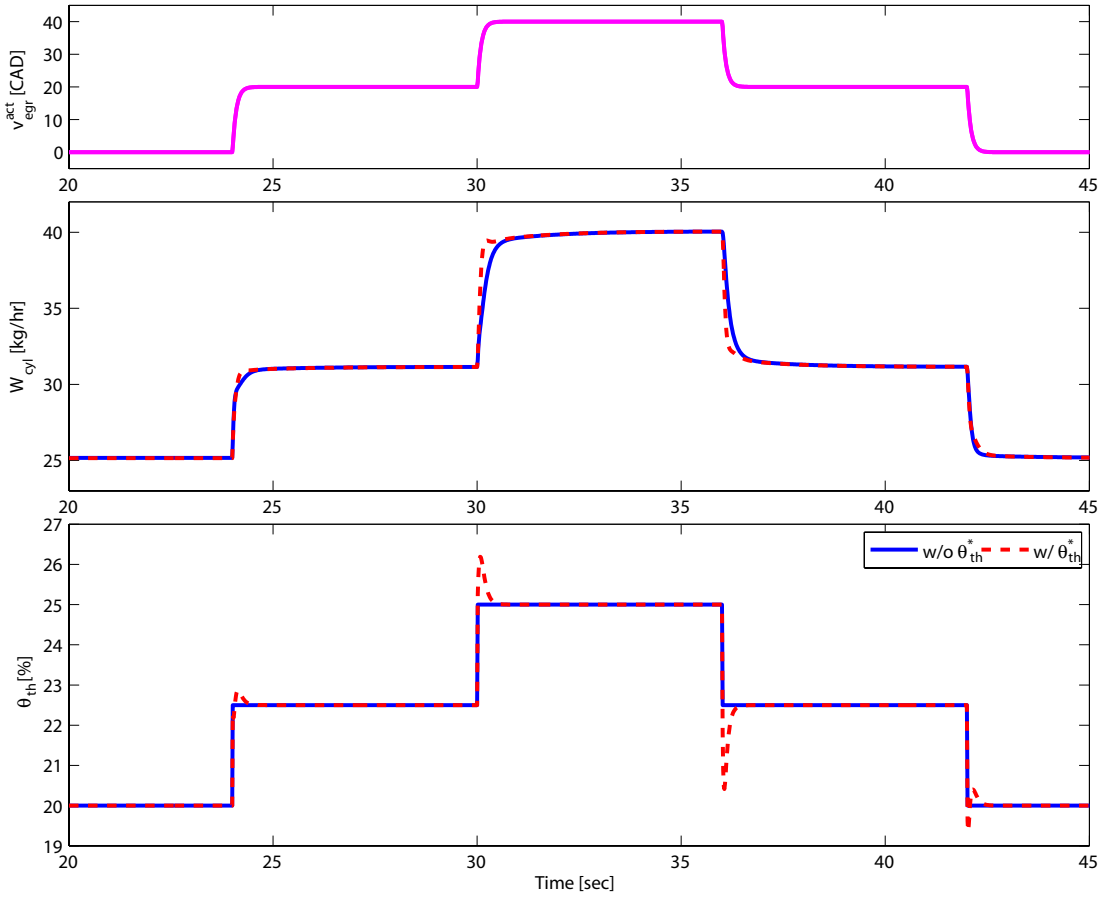

Figure 4.10 Comparison of the throttle step cylinder air charge flow rate W_{cyl} of VVT turbocharged engine without compensation θ_{th}^* (blue solid lines) and VVT turbocharged engine with compensation (red dashed lines); engine speed is 2000 RPM, throttle is stepped as θ_{th} = 20 $\rightarrow$ 22.5% $\rightarrow$ 25% $\rightarrow$ 22.5% $\rightarrow$ 20%. (**Simulation**)

4.6 Conclusion

This chapter presented a modification of the nonlinear mean value model [47] of a turbocharged spark ignition flex-fuel engine equipped with variable camshafts and electronic throttle. Two static valve overlap schedules were derived for "best torque" and "best iEGR" requirements. To improve the transient behaviors of the cylinder charge air flow rate (or torque) during throttle step changes, the valve compensator has been introduced in the air-path control loop. To reduce the disturbance of the VVT change on cylinder charge flow rate, a nonlinear model-based valve compensator was designed in addition to the base throttle controller for the turbocharged engine. This compensator improves the transient behavior of cylinder charge flow rate, especially at low load. The valve compensator was tested using both a mean-value model and a vehicle engine. The valve compensator showed

a considerable improvement in the regulation of cylinder charge flow rate W_{cyl} while the valve overlap v changes.

The proposed valve compensator can be used to conduct an on-board calibration such as an extremum seeking (ES) control algorithm [56] and introduced in Fig. 5.13 in the next chapter. As more control parameters are introduced by the turbocharger, variable valve timing and direct fuel injection, an increased amount of calibration efforts are required to determine the optimal control set-points for engine performance and emissions. To supplement this calibration burden and take into account of all the influencing factors such as fuel properties and engine aging, the on-board calibration scheme searches the optimal VVT and spark ignition through the evaluation of engine performances while VVT and spark timing are perturbed. The valve compensator can moderate the cylinder charge disturbance from this VVT perturbation.

Chapter 5

Extremum Seeking of Variable Valve Timing and Spark Timing for On-Board Calibration

5.1 Introduction

Most of the current engine controls are implemented based on look-up tables with its values calibrated for various operating conditions, typically the engine speed and load, during the development of a new vehicle. The control parameters introduced by the turbocharger, variable valvetrain, and direct fuel injection, increase the amount of calibration effort required to determine the optimum control set-points for engine performance and emissions. Even if feasible and required, this initial calibration can not take into account of all the influencing factors such as fuel properties, engine component aging and environmental changes. Therefore, we present in this chapter a method to help reduce or optimize engine calibration effort for a turbocharged spark ignition direct injection engine by employing an extremum seeking (ES) controller to optimize VVT position and spark timing via in-cylinder pressure sensing of combustion phasing.

To analyze, develop, and verify the ES optimization scheme for VVT and spark it is important that we take into account the cycle-to-cycle combustion variability, especially at high level of internal residuals. It is known that the internal exhaust gas recirculation (iEGR) could reduce NOx emissions and heat losses to the cylinder walls as a result of the lower combustion temperature, and reduce pumping loss with a higher intake manifold pressure. However, high charge dilution via iEGR introduces high cycle-to-cycle combustion variations. Poor combustion (very advanced or retarded combustion phasing) deteriorates overall combustion efficiency. Therefore, there exist an optimum set of VVT positions at each engine operating point to achieve the maximum combustion efficiency. For optimum VVT setting there is an optimum spark setting.

The model developed predicts the combustion phasing (i.e. crank angle of 50% fuel burned, θ_{CA50}) and mean effective pressure (MEP) at various engine speeds and loads in order to tune and test the ES under realistic conditions for VVT and spark. Although ES is not a model-based algorithm, reduced models are developed in this chapter. A simple Gaussian stochastic representation of the cycle to cycle variability is then used and its variance is tuned to predict the cycle-to-cycle combustion variations at different iEGR levels. An ES controller is then designed to determine the optimum VVT position and spark timing for minimum net specific fuel consumption (NSFC) at given engine operating point.

5.2 Combustion Model

5.2.1 Combustion Phase

Combustion duration $\Delta\theta_{comb}$ defined in the spark ignition (SI) engines as the crank angle degrees between spark timing θ_σ and 90% fuel burned θ_{CA90} is modeled as following [76, 77]:

$$\theta_{CA90} = \theta_\sigma + \Delta\theta_{comb}, \tag{5.1a}$$

$$\text{where} \quad \Delta\theta_{comb} = kT_{cyl}(\theta_\sigma)^{-2/3}T_m^{1/3}exp\left(\frac{E_c}{3R_cT_m}\right) \tag{5.1b}$$

$$T_m = T_{cyl}(\theta_\sigma) + e(1-x_{RG})\Delta T \tag{5.1c}$$

$$\Delta T = \frac{Q_{LHV}m_{fuel}}{c_v m_c}, \tag{5.1d}$$

where $T_{cyl}(\theta_\sigma)$ is the cylinder temperature at spark timing, R_c is the ideal gas constant, x_{RG} represents residual gas fraction, and E_c is the activation energy emulating for the effective threshold at which the combustion reaction occurs. Q_{LHV} and m_{fuel} are the lower heating values of fuel and the injected fuel amount per each engine cycle, respectively. c_v is a specific heat of cylinder mixture during combustion and m_c represents the cylinder charge mixture mass at the intake valve close. The values of e and k are subject to be parameterized as a function of θ_σ so that the predicted combustion duration from (5.1b) matches the experimentally observed values at different operating conditions:

$$k(\theta_\sigma) = \alpha_0 + \alpha_1\theta_\sigma + \alpha_2\theta_\sigma^2 \tag{5.2a}$$

$$e(\theta_\sigma) = \beta_0 + \beta_1\theta_\sigma + \beta_2\theta_\sigma^2. \tag{5.2b}$$

Parameterized values for e and k are shown in Fig. 5.1 as a function of θ_σ using spark sweep data[1] for throttle position θ_{th} from 30% to 35% at the engine speed N = 2000 and 3000 RPM. The data show and the model is tuned so that combustion duration increases

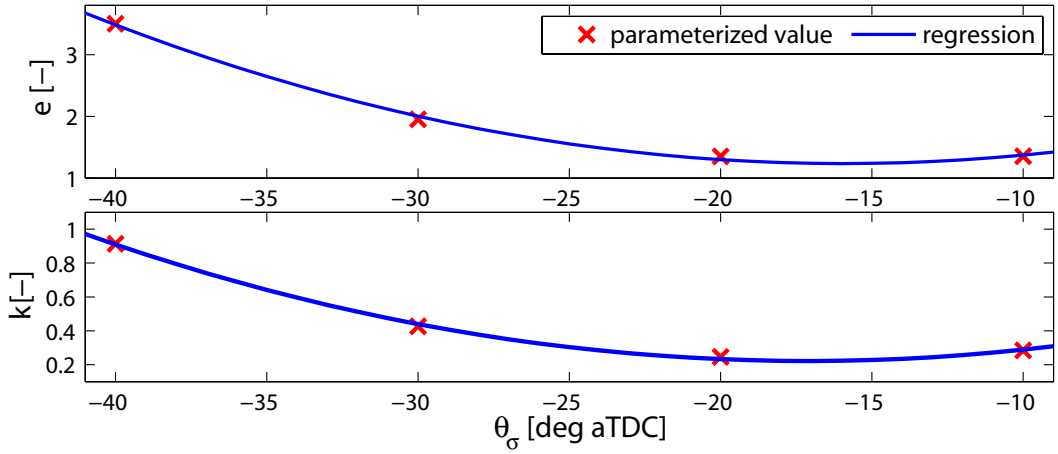

Figure 5.1 Parameterized values of e and k as a function of θ_σ using Ricardo DoE data at N = 2000 and 3000 RPM.

with retarded spark timing (i.e. close to the top dead center (TDC)). In the model from (5.1) with same retarded spark timing, the term $T_{cyl}(\theta_\sigma)^{-2/3}$ from (5.1b) decreases due to rising $T_{cyl}(\theta_\sigma)$ given other engine input variables fixed. Lower value of the parameter e associated with retarded spark timing represents less amount of fuel energy converted during the combustion, and it increases the exponential term $exp(E_c/3R_cT_m)$ in (5.1b) to compensate for the lower $T_{cyl}(\theta_\sigma)^{-2/3}$. High iEGR level with other engine variables fixed lengthens the combustion duration $\Delta\theta_{comb}$, which can be predicted from (5.1). Higher iEGR also decreases T_m which increases $\Delta\theta_{comb}$ by exponentially reducing the term $exp(E_c/3R_cT_m)$. The crank angle of 50% fuel burned θ_{CA50} is then estimated with $\theta_{CA50} = \theta_\sigma + 0.76\Delta\theta_{comb}$. Comparisons between engine measurement and model estimation for θ_{CA50} and θ_{CA90} are shown in Fig. 5.2. Normalized root mean squared deviation (NRMSD) values of θ_{CA50} and θ_{CA90} are 0.1065 and 0.1125, respectively. The data shown in Fig. 5.2 correspond to the most frequently visited operating conditions based on typical driving cycles.

5.2.2 Mean Effective Pressure

Indicated mean effective pressure (IMEP) is predicted as the indicated work divided by engine cylinder displacement volume V_d, where the indicated work is defined as the integral of cylinder pressure with respect to cylinder volume from bottom dead center (BDC)

[1]Data has been provided by Robert BOSCH LLC based on experiments performed at Ricardo using a commercial 4 cylinder 2 L turbocharged direct injection engine with VVT.

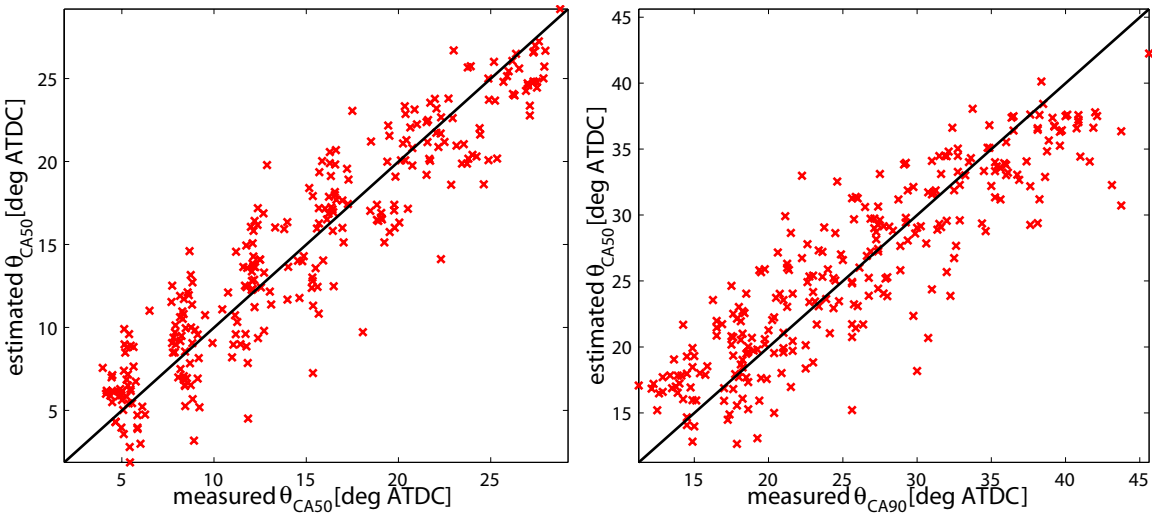

Figure 5.2 Comparison between engine measurement and estimated crank angle of 50% and 90% fuel burned, θ_{CA50} and θ_{CA90} (left and right subplots, respectively), for throttle angle θ_{th} from 30% to 35% open at N = 2000 and 3000 RPM.

of the compression stroke to BDC of the expansion stroke (area A plus C enclosed by a path $a \to b \to c \to d$ in Fig. 5.3). A mean-value model from [47] is able to capture the cylinder pressures at four different combustion timings; i.e. intake valve close (IVC), before combustion p_b, after combustion p_c and exhaust valve open (EVO). The pressure p_a and p_b are calculated based on polytropic compression with an exponent γ_c and a model of the pressure at IVC, p_{ivc}. Note that p_{ivc} is determined by a linear function of the intake manifold pressure p_{im}, $p_{ivc} = c_1 p_{im} + c_0$. The pressure after the combustion is calculated assuming instantaneous heat release at the top dead center (TDC). Finally the pressure p_d is calculated using a polytropic expansion with a tuned but fixed value for the expansion exponent, γ_e.

In this chapter, IMEP estimation relies on the combustion phase and we use $\theta^*_{CA50} = 6-9$ degrees after top dead center (deg aTDC) as a proxy of MBT combustion where IMEP_{MBT} is achieved ([78]). If the combustion phasing is excessively advanced, it results in the instantaneous heat release during the compression stroke. This early combustion can be depicted as a combustion path, $a \to b' \to c' \to c \to d$ in Fig. 5.3. On the other hand, if the combustion phasing is excessively retarded, the instantaneous heat release takes place during expansion stroke. This late combustion can be represented as a combustion path, $a \to b \to b' \to c' \to d$. Therefore, IMEP estimation with a combustion phase of θ_{CA50} is

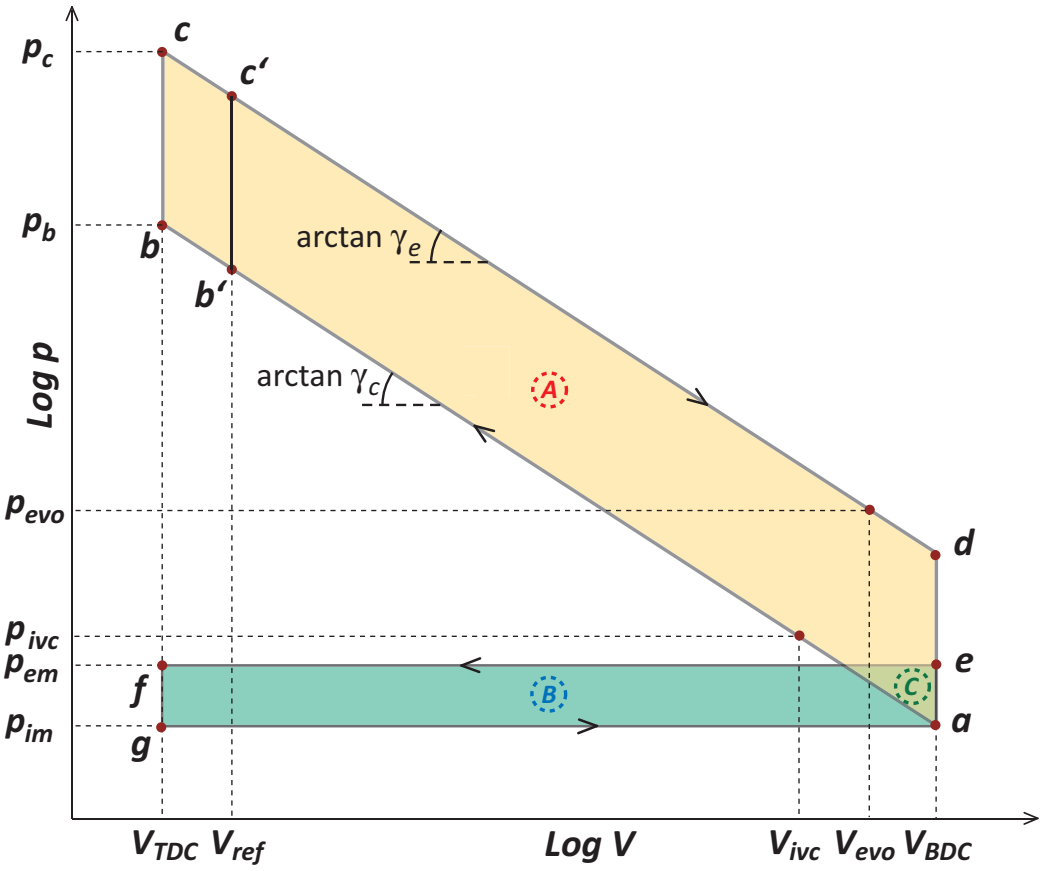

Figure 5.3 *Log p* versus *Log V* diagram of in-cylinder pressure and IMEP estimation.

conducted using:

$$
\begin{aligned}
IMEP &= \frac{\int_a^{b'} p\, dV + \int_{c'}^{d} p\, dV}{V_d} \\
&= \left(\frac{p_{ivc} V_{ivc}^{\gamma_c}}{1-\gamma_c}\right)\left(V_{ref}^{1-\gamma_c} - V_{BDC}^{1-\gamma_c}\right) \\
&+ \left(\frac{p_c V_{TDC}^{\gamma_e}}{1-\gamma_e}\right)\left(V_{BDC}^{1-\gamma_e} - V_{ref}^{1-\gamma_e}\right), \qquad \text{(5.3a)}
\end{aligned}
$$

$$
\text{where } V_{ref} = V\left(\theta_{CA50} - \theta^*_{CA50}\right). \qquad \text{(5.3b)}
$$

Note that the cylinder volume of V_{ref} at b' (or c') is defined as the cylinder volume at the crank angle of $\left(\theta_{CA50} - \theta^*_{CA50}\right)$ deg aTDC and the function $V(\theta)$ denotes the cylinder volume at the crank angle of θ deg aTDC. With either earlier or later combustion than θ^*_{CA50} (V_{ref} increases for both cases), therefore, IMEP decreases.

If we assume that the cylinder pressures during the exhaust and intake stroke are approximately equal to exhaust and intake manifold pressures, p_{im} and p_{em}, respectively, the

pumping mean effective pressure (PMEP) is estimated through the area B and C together in Fig. 5.3:

$$PMEP = \frac{\int_e^f p\, dV + \int_g^a p\, dV}{V_d} = p_{em} - p_{im}. \tag{5.4}$$

The net mean effective pressure NMEP is the net work per displacement volume, where the net work is the integral of cylinder pressure with respect to volume over the full 720 ^{o} engine cycle; i.e. $NMEP$ = $IMEP$ - $PMEP$ = $(\text{area } A + \text{area } C) - (\text{area } B + \text{area } C) =$ area A – area C.

Based on the air path characteristic (i.e. engine pumping flow, equation (1) from [55], turbocharger mapping and orifice equations, and equations (28) - (39) from [47]), increasing valve overlap increases the residual gas fraction x_{RG}, which also decreases PMEP and, hence, increases NMEP by increasing intake manifold pressure p_{im}. The engine system efficiency improvement by increasing x_{RG}, however, is bounded at a certain level of x_{RG} due to a tradeoff between PMEP benefit and combustion efficiency [79]. To account for similar behavior in the engine model, we modify the combustion efficiency η^o_{comb} from the equation (11) from [47] using:

$$\eta_{comb} = \frac{1}{1 + l_1 e^{l_2 x_{RG}}} \eta^o_{comb}, \tag{5.5}$$

which is shown in Fig. 5.4 as seen in experimental data and suggested by [79]. The combustion and mean effective pressure (MEP) model structure are shown in Fig. 5.5. Combustion model includes (5.1) and (5.2) along with the equations (7) - (13) from [47], and MEP model as defined in (5.3) and (5.4).

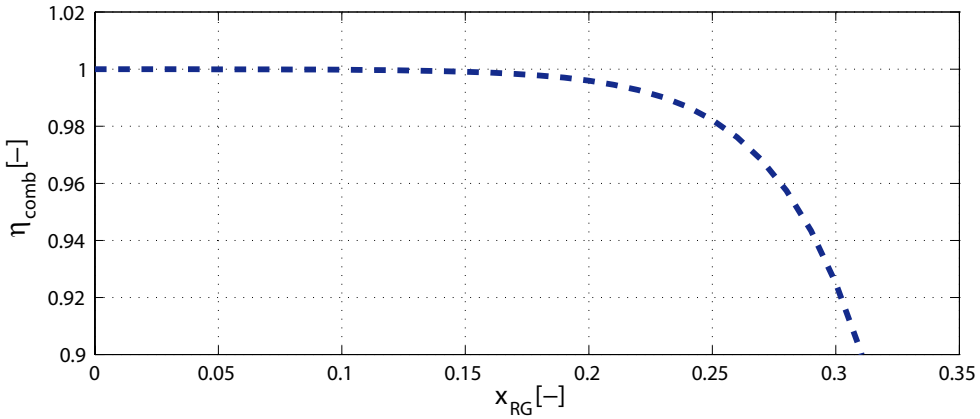

Figure 5.4 Combustion efficiency, η_{comb}, as a function of residual gas fraction x_{RG}.

Fig. 5.6 and 5.7 show the comparisons between dynamometer engine test data and model simulation data for indolene (E0) and 85% ethanol mixture fuel (E85), respectively, with spark sweeps at θ_{th} = 32 $\sim$ 34% and N = 2000 RPM. The two top rows in these

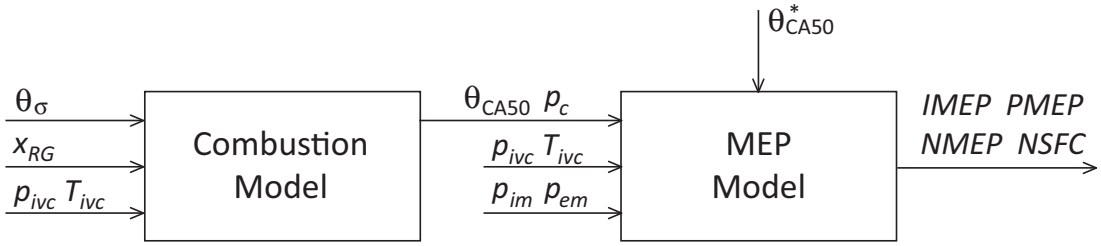

Figure 5.5 Combustion and mean effective pressure (MEP) model structure.

figures show the input variables for both tested dynamometer engine and engine model, while subplots in the bottom three rows compare measured and predicted important engine output variables such as air mass flow rate W_{air}, intake and exhaust manifold pressures p_{im} and p_{em}, combustion phase θ_{CA50}, IMEP and specific fuel consumption (SFC). From the comparison in Fig. 5.6 the engine mean-value model is shown capable to capture all important engine output variables both quantitatively and qualitatively. IMEP from both dynamometer engine and simulation model decreases when θ_{CA50} is retarded from approximately 6 deg aTDC. A mismatch in the measured and predicted air flow is probably due to the measurement error. A mismatch is also observed in IMEP.

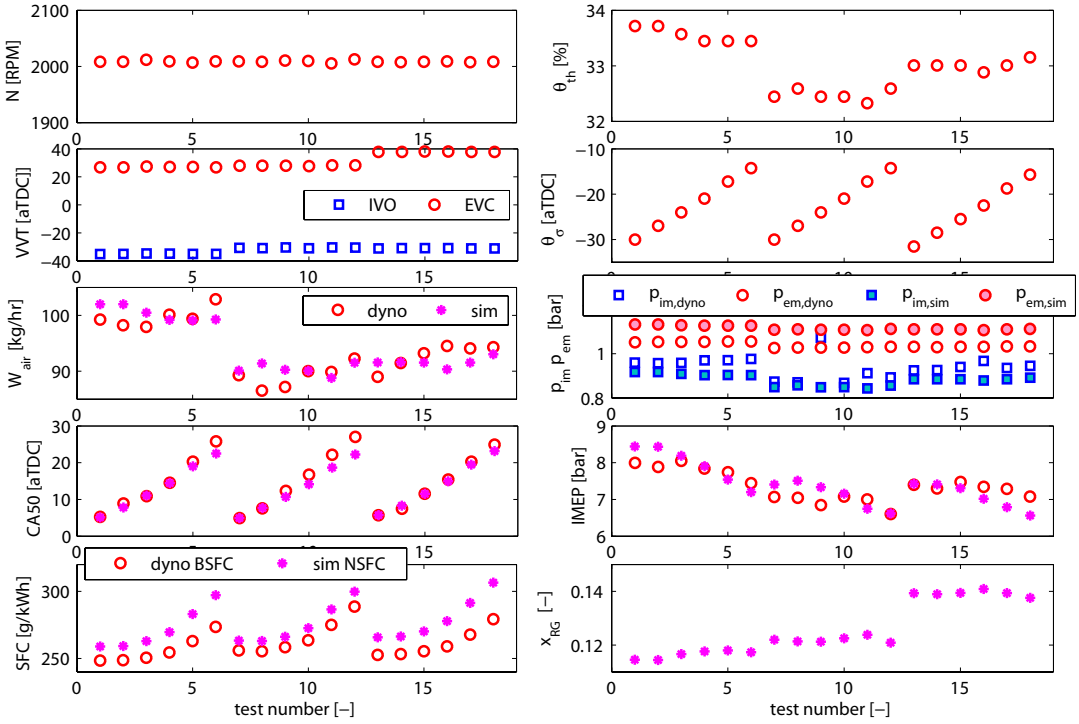

Figure 5.6 Comparison between engine data and model simulation for E0 fuel.

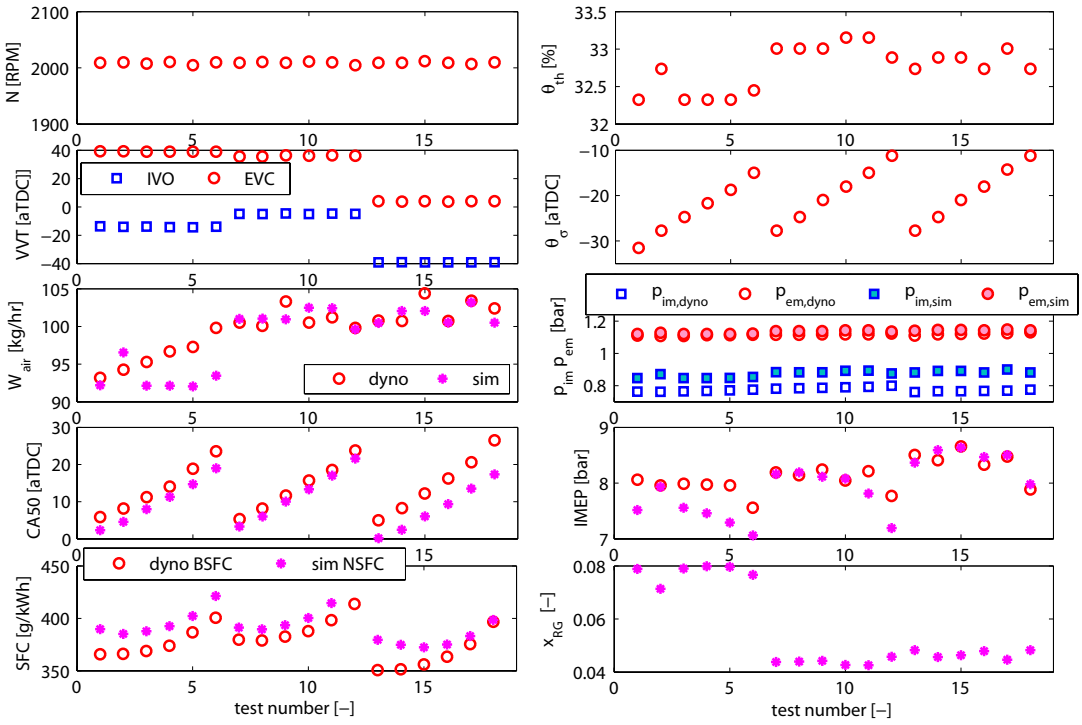

Figure 5.7 Comparison between engine data and model simulation for E85 fuel.

5.2.3 Global Engine Conditions vs. Variable Valve Timing

The model developed in the previous section will be used later to test the valve optimization scheme using ES algorithm, therefore, it is important to capture the global engine behavior as x_{RG} changes. Hence, we show in this paragraph that the engine model achieves the maximum NMEP at a specific VVT position and θ_{CA50} setting. To do this, we plot NMEP and NSFC as a function of VVT positions and θ_{CA50} in Fig. 5.8 with engine speed N and mass air flow rate fixed. In specific, the exhaust valve closing (EVC) and intake valve opening (IVO) are symmetrically changed by 5 crank angle degrees (CAD) from TDC and θ_{CA50} is regulated from -6 to 18 deg aTDC with increments of 3 CAD. Fig. 5.8 shows the simulation results with a fixed air mass flow rate of W_{air} = 100 kg/hr and engine speed N = 2000 RPM. Note that combustion phase of MBT operation (i.e. θ^*_{CA50}) was assumed to be 6 deg aTDC and it is indeed the optimum θ_{CA50}.

The optimal engine operation with respect to both NMEP and NSFC is also achieved with the valve overlap of 56 CAD (i.e. IVO $\approx$ -28 and EVC $\approx$ 28 deg aTDC). These optimal values mainly depend on (5.5), and are expected to vary not only for different engine speeds and loads but also for unknown factors which affect the performance of the engine system. These unknown factors may come from engine system aging, wear, and/or other uncontrollable environmental factors such as outside temperature and humidity. This

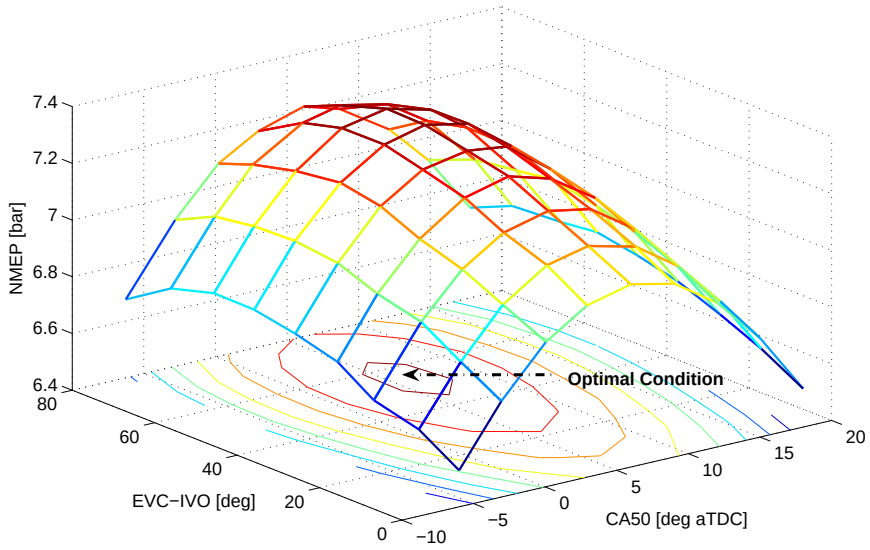

(a) NMEP vs. VVT vs. θ_{CA50}

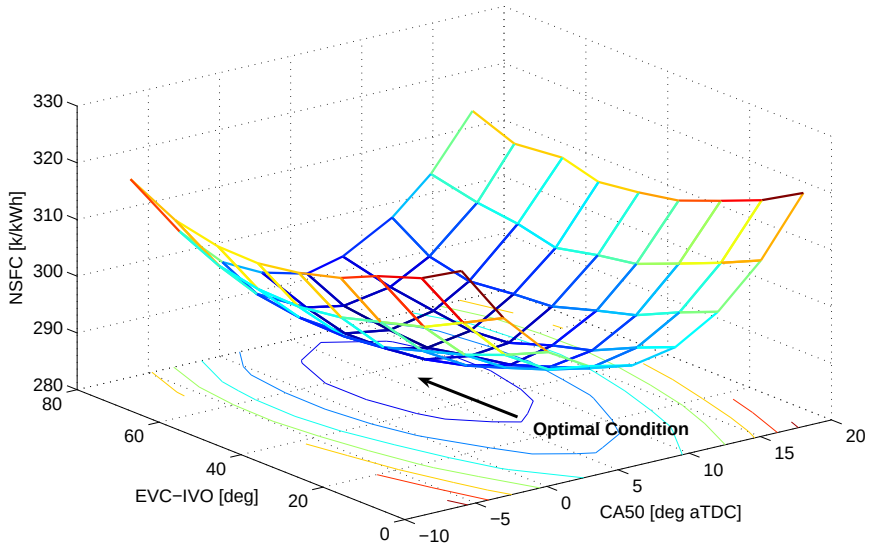

(b) NSFC vs. VVT vs. θ_{CA50}

Figure 5.8 Estimated NMEP and NSFC of the engine model for various VVT positions and combustion phase of θ_{CA50} with W_{air} = 100 kg/hr at the engine speed of 2000 RPM.

uncertainty justifies the development of an on-line optimization scheme for the on-board calibration to automatically seek the optimum operating point of VVT and θ^*_{CA50}, which will be discussed in section 5.3.

5.2.4 Combustion Statistics

The mean-value engine model presented previously captures the combustion phase, θ_{CA50}, and IMEP in the sense of engine cycle-averaged values. In this part, the model is modified to capture the cyclic variation of θ_{CA50} and IMEP observed in the experiments. The left subplot in Fig. 5.9 shows the histogram of θ_{CA50} within 100 consecutive steady-state engine cycles for the mass air flow of 130 kg/hr at 2000 RPM with other engine inputs fixed, while the right subplot represents the correlation between θ_{CA50} and IMEP for each cycle. In the histogram of θ_{CA50} at this steady-state engine operation, θ_{CA50} can be approximated by a Gaussian distribution with the standard deviation of θ_{CA50}, σ_{CA50} = 1.785 in this case. The IMEP model described in (5.3) as a function of θ_{CA50} predicts the same trend as the measured IMEP since IMEP decreases as the combustion phase, θ_{CA50}, is retarded from MBT position (θ^*_{CA50} is approximately 8 deg aTDC in this condition). Note that other steady-state engine experiments with different engine speeds and loads show similar statistical combustion behavior.

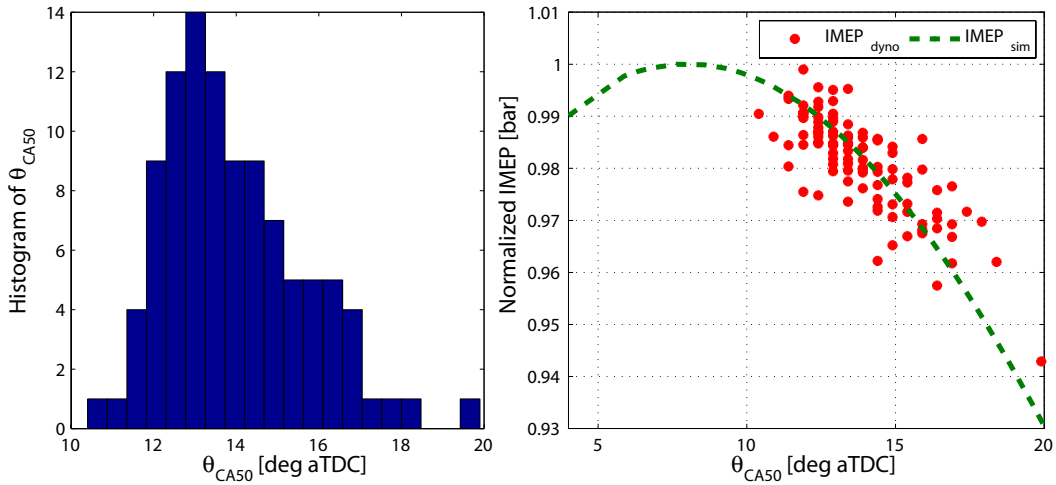

Figure 5.9 Correlation between combustion phase θ_{CA50} and IMEP (right) and histogram of θ_{CA50} (left) for 100 consecutive engine cycles with W_{air} = 100 kg/hr at N = 2000 RPM.

Engine experimental data show that increasing the fraction of residual gas x_{RG} through internal exhaust gas recirculation (iEGR) increases the covariance of IMEP $Cov(\text{IMEP})$, and this engine behavior is modeled using the standard deviation of θ_{CA50}, σ_{CA50} as:

$$\begin{aligned} \theta_{CA50} &= \theta^0_{CA50} + \sigma_{CA50} N(0,1), \\ \text{where} \quad \sigma_{CA50} &= e^{k_1 x_{RG}} + k_2, \end{aligned} \tag{5.6}$$

where $N(0,1)$ denotes a zero-mean, unit-variance Gaussian distribution, which explains a random cyclic combustion variation. Fig. 5.10 shows an example of σ_{CA50} supported by

the engine experimental data. The parameters, k_1 and k_2 in (5.6) can vary for different engine operating conditions. Fig. 5.11 shows the model structure including the statistical combustion phase characteristics.

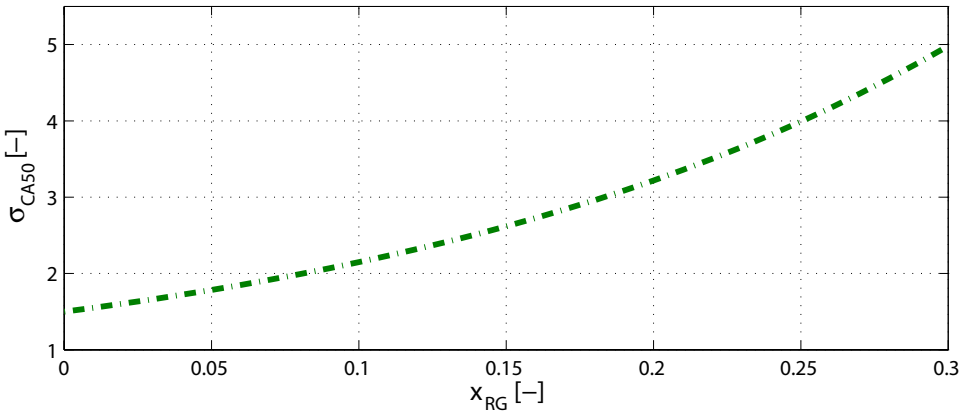

Figure 5.10 Standard deviation of θ_{CA50}, σ_{CA50}, as a function of residual gas fraction x_{RG}.

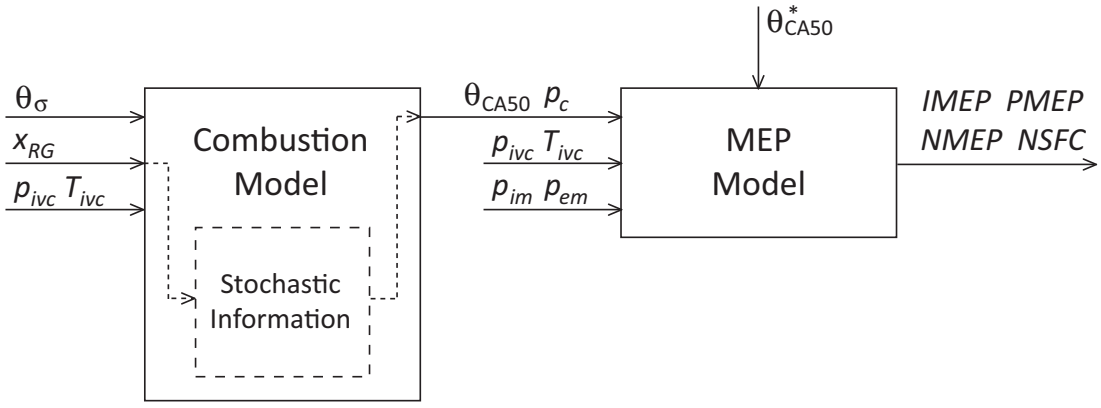

Figure 5.11 Combustion and mean effective pressure (MEP) model structure with stochastic combustion phase information.

Fig. 5.12 shows the measured and simulated outputs for the throttle step changes, in which the transient behavior of the parameterized engine model is validated. In this case, the engine was operated at the engine speed of 2500 RPM and intake air mass flow rate of 100 kg/hr for E0 fuel. The four subplots in the first column show the dynamometer engine and simulation model inputs, while the rest of them compare engine and simulation outputs. In the comparison of θ_{CA50}, the variance from both measured and simulated θ_{CA50} before throttle step change is slightly greater than after the step change. Note that the model exhibits larger variance in θ_{CA50} before the step change due to larger x_{RG} as shown in the last subplot of the 3rd column. Simulated IMEP is also comparable to the measured engine IMEP both quantitatively and qualitatively.

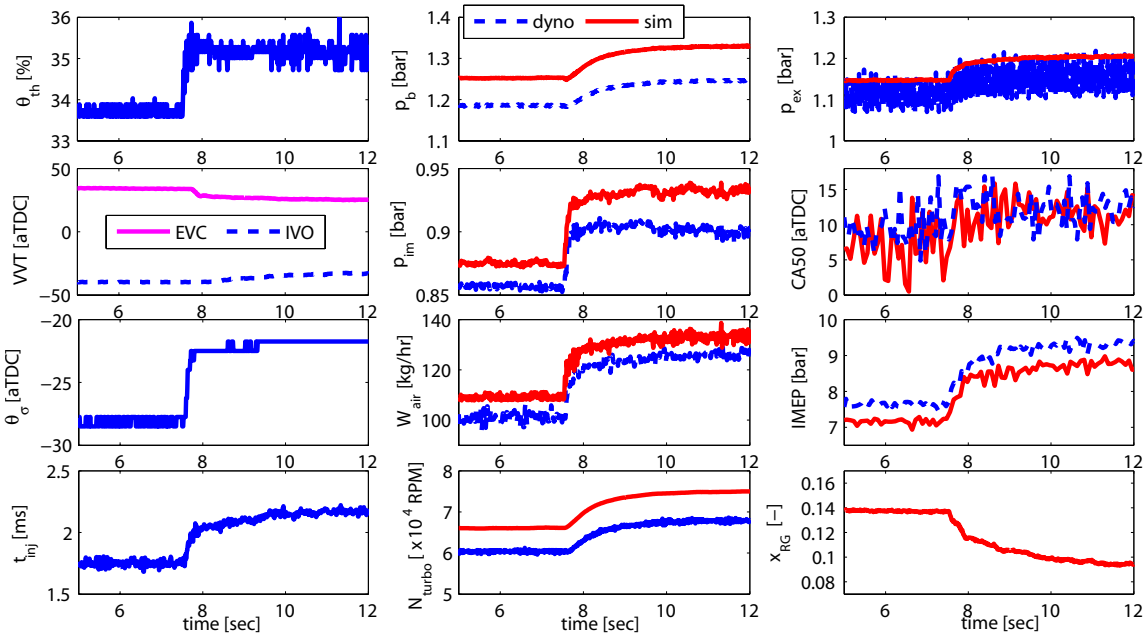

Figure 5.12 Simulated and measured engine outputs for the throttle step changes with fuel E0 at N = 2500 RPM.

5.3 On-Board Calibration Scheme

A non-model based optimization scheme such as the extremum seeking (ES) control is an iterative optimization process performed in real time on a physical system [80, 81]. The function being optimized is the steady-state relationship between the system's input parameters and its performance output. Since the response function, denoted here by NSFC, is not known (otherwise, it could be optimized in a computer), ES algorithms rely only on its measurements to search for the optimum. Starting from some initial parameter values (VVT and spark timing), such an algorithm iteratively perturbs the parameters, monitors the NSFC response, and adjusts the parameters toward improved NSFC. This process runs usually as long as improvement is being produced.

The ES control unfortunately takes time to converge, hence are typically employed only at steady-state operating points [82]. In passenger vehicles the operating conditions frequently visited and for long duration (long enough for the real-time optimization) are the idle and cruise conditions. Hence, we propose here to use ES to optimize the engine inputs at cruise and idle, and attempt to use these optimal inputs to adapt the entire input mapping as indicated in Fig. 5.13. Even if the entire map does not get adapted, the gain from optimizing engine efficiency at idle and cruise could be substantial as these idle and cruise conditions are frequently visited in a realistic urban driving cycle. To achieve maximum fuel efficiency given specific engine operating conditions (i.e. given engine speed N

and NMEP), both the optimal combustion phase θ_{CA50}, and VVT position are required and will be derived in this section.

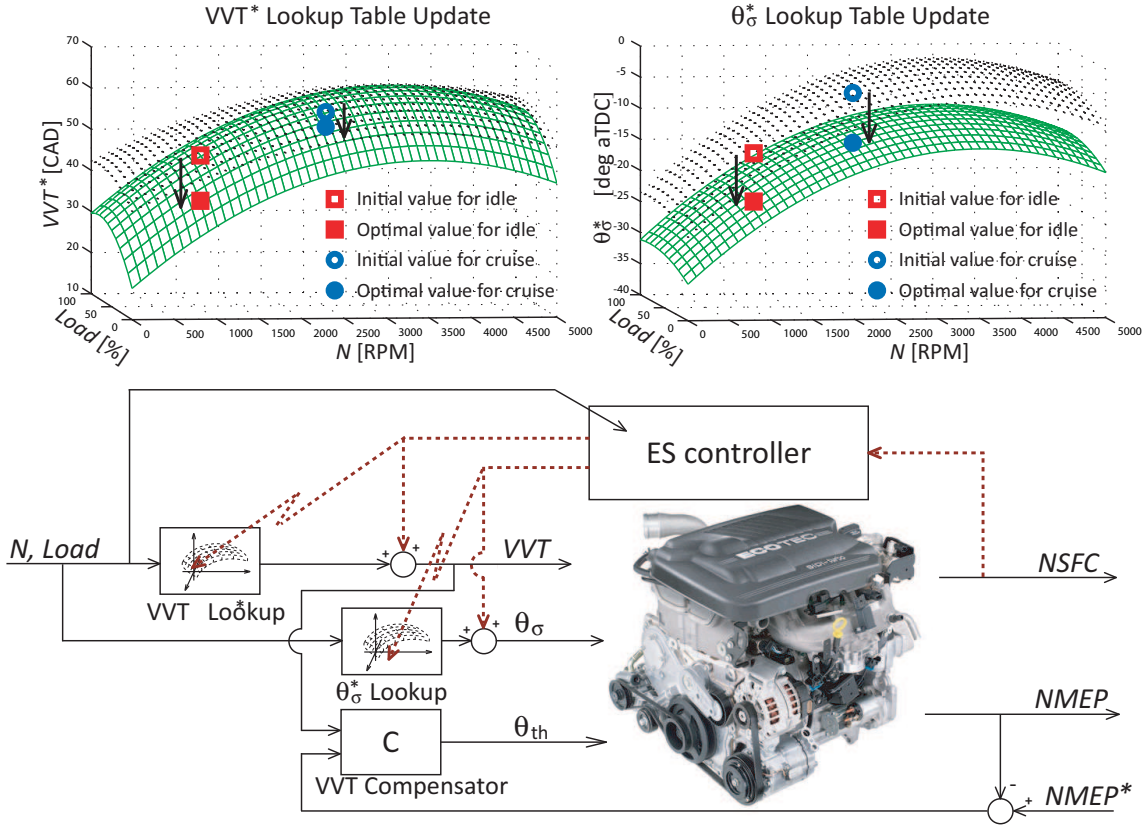

Figure 5.13 Structure of an on-board calibration scheme with adaptation of the production maps based on the engine input conditions.

The engine on a vehicle is run by the pre-defined engine maps for VVT and θ_σ^* based on the engine speed and driver's load command through the throttle pedal position. Once the engine visits either the idle or cruise condition the on-line optimization controller is turned on and it starts searching for the optimal VVT and θ_σ. Notice that the load disturbance can be introduced while the VVT excitation is commanded during the ES as presented in the previous chapter. Therefore, the demanded load is regulated through the proposed VVT compensator derived in (4.9) via the electronic throttle assuming the driver needs a specific torque (or NMEP) output.

5.3.1 Extremum Seeking Control

The model developed so far can imitate well the real engine performance around its optimal operating points of VVT and θ_{CA50} along with the practical noise levels of the engine performance variables. Therefore it can provide a meaningful testing platform before the

implementation of the ES controller directly on the vehicle. Moreover the model can assist in tuning the ES algorithm especially for the calibration of the bandwidth and amplitude of the excitation. Appropriate gains of the on-line optimization scheme, therefore, can be designed based on this valuable information provided by the simple statistical combustion model derived in section 5.2.

The ES controller presented in this chapter uses sinusoidal excitations to select the values of the VVT position and θ_σ which minimize the cost function NSFC while θ_{th} is regulated through the VVT compensator from Chapter 4 to achieve desired NMEP [83, 84, 85]. By minimizing the NSFC the optimal VVT position and θ_{CA50} with the highest fuel efficiency is also achieved for a given NMEP. A block diagram of the ES controller shown in Fig. 5.13 is detailed in Fig. 5.14. The basic dynamics of the discrete ES controller and the values of $\Delta\theta_\sigma$ and ΔVVT at the kth iteration are introduced in (5.7) below.

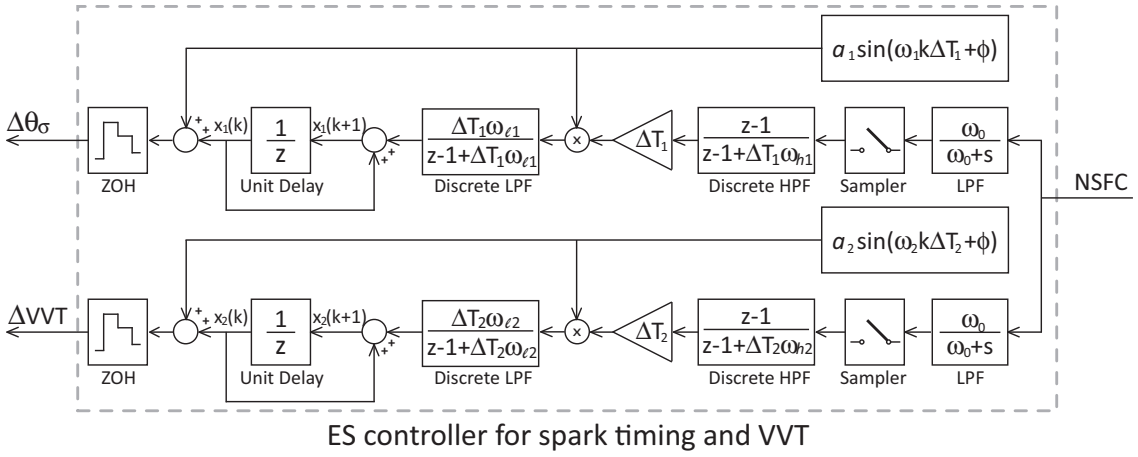

Figure 5.14 Extremum seeking control for optimal θ_σ and VVT.

$$x_1[k+1] = x_1[k] + \Delta T_1 a_1 \sin(\omega_1 k \Delta T_1 + \phi)\, NSFC[k], \tag{5.7a}$$

$$\Delta\theta_\sigma[k] = x_1[k] + a_1 \sin(\omega_1 k \Delta T_1 + \phi), \tag{5.7b}$$

$$x_2[k+1] = x_2[k] + \Delta T_2 a_2 \sin(\omega_2 k \Delta T_2 + \phi)\, NSFC[k], \tag{5.7c}$$

$$\Delta VVT[k] = x_2[k] + a_2 \sin(\omega_2 k \Delta T_2 + \phi), \tag{5.7d}$$

where $\omega_i = \pi/\Delta T_i$ rad/sec for i = 1 and 2 and $\phi = \pi/2$. Note that $VVT[k]$ denotes the valve overlap between IVO and EVC, and we assume that IVO and EVC are symmetrically changed from TDC similar to the duel-equal VVT system. In the future, the VVT can be split into two variables (i.e. IVO and EVC), for which three variables are tuned through the ES controller with slower convergence as shown by [86].

Measured NSFC is first filtered through a low-pass filter with a cut-off frequency of ω_0 = 2 Hz (equivalent time constant of 0.5 second or $\frac{100}{12}$ engine cycles at N = 2000 RPM)

and, then, discretized at a sampling rate equal to the $n_i = \frac{\Delta T_i}{120} N$ engine cycles for i = 1 and 2, respectively, at a given engine speed N (i.e. 30 and 60 engine cycles for i = 1 and 2 at N = 2000 RPM). The choice of the sampling rate must ensure that NMEP reaches the steady-state values after each VVT and spark excitation such that the engine system with the VVT compensator may be considered as a static nonlinearity function. The discrete high-pass filter then eliminates the DC component of NSFC (de-trending) to provide the gradient information of NSFC at the current spark timing and VVT position. The filtered signal from the high-pass filter is multiplied by the perturbation signal $a_i \sin(\omega_i k \Delta T_i + \phi)$, and the resulting signal passes through the low-pass filter to extract the DC component of the perturbation signal. For details of formal discussions including stability proofs and design guidelines on multivariable ES, please refer to [85]. Note that the discrete high- and low-pass filters together in the ES control algorithm eliminate another design parameters φ and $NSFC_{des}$ typically needed to formulate an objective function, for instance, $Q[k] = \varphi\,(NSFC_{des} - NSFC[k])^2$. The nominal NSFC levels vary significantly for different fuels between gasoline (E0) and a blend of up to 85% ethanol (E85) since the required fuel injection amount for E85 is approximately 1.6 times larger than E0 to produce the same engine torque.

5.3.2 Extremum Seeking Parameter Selection

Cautious and proper selections of the ES controller design parameters are required prior to the ES implementation. The ES parameters are the perturbation frequencies, ω_i, the amplitudes of each perturbation, a_i, and the filter cut-off frequencies, ω_0, ω_{hi}, and ω_{li} for i = 1 and 2. First, the perturbation frequencies ω_1 and ω_2 must be slower than the plant dynamics to ensure the plant to be treated as a static nonlinear function such that, at the engine speed N = 2000 RPM, we have $\omega_1 = \frac{1}{\Delta T_1} = 0.56$ Hz and $\omega_2 = \frac{1}{\Delta T_2} = 0.28$ Hz, respectively. Next, the amplitudes of the spark and VVT perturbations a_1 and a_2 are related to the ES convergence speed to the optimum and, in general, increasing a_1 and a_2 accelerates the convergence speed. Beyond permissible ranges, however, large values of a_1 and a_2 also introduce undesired engine torque changes especially for the VVT perturbation a_2 as shown in Chapter 4 and we selected a_1 = 1.5 CAD and a_2 = 2.5 CAD.

The cut-off frequency of the low-pass filter ω_0 in Fig. 5.14 is selected to be slow enough so that the low-pass filter removes the cycle-to-cycle NSFC measurement noise to determine the nominal value of NSFC for given spark timing and VVT. At the same time, the low-pass filter frequency needs to be faster than the ES sampling frequencies $1/\Delta T_1$ and $1/\Delta T_2$ and we select ω_0 = 2 Hz, approximately twice of $1/\Delta T_1$ = 1.11 Hz and four times

of $1/\Delta T_2$ = 0.56 Hz at N = 2000 RPM. The simulated response in the NSFC signal of the engine model to a step change in spark timing and VVT is presented in Fig. 5.15. It can be observed that in approximately 1 second after the spark and VVT step changes, the filtered NSFC approaches its steady state value. Therefore, the sampling rates, ΔT_1 = 1.8 and ΔT_2 = 3.6 seconds, in the ES controller at N = 2000 RPM are appropriate.

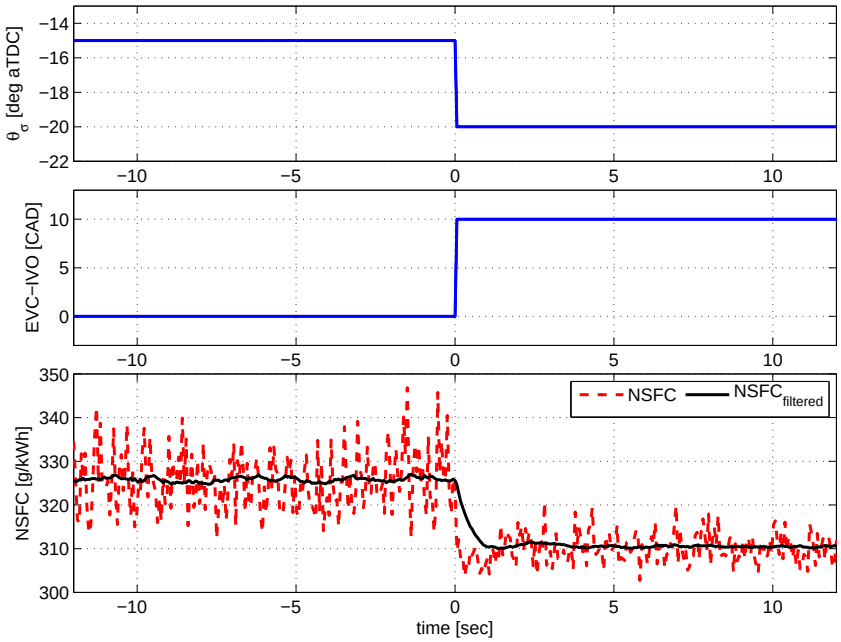

Figure 5.15 Simulation response in the NSFC signal of the engine model to a step change in spark timing from -15 to -20 CAD aTDC and VVT (i.e. EVC - IVO) from 0 to 10 CAD valve overlap.

The two discrete low- and high-pass filter cut-off frequencies ω_{hi} and ω_{li} for i = 1 and 2 must be designed in coordination with the perturbation frequency ω_1 and ω_2, respectively. For instance, the discrete high-pass filter frequency ω_{hi} must allow the perturbation frequency ω_i to pass through while the discrete low-pass filter frequency ω_{li} is required to attenuate the perturbation frequency ω_i for i = 1 and 2. Given the engine speed of N = 2000 RPM, we select $\omega_{h1} = 0.22 < \omega_1$ and $\omega_{l1} = 0.37 < \omega_1$ Hz for the spark ES control algorithm and $\omega_{h2} = 0.11 < \omega_2$ and $\omega_{l2} = 0.185 < \omega_2$ Hz. Note that all these gains are selected based on the engine cycle time domain and, therefore, the presented absolute values change for different engine speed. Fig. 5.16 shows Bode plots of the discrete filters from the spark ES controller (top subplot) and the VVT ES controller (bottom subplot). The Black dashed-dot lines indicate the perturbation frequencies ω_1 and ω_2.

The guideline for the ES control parameters explained in this section does not always guarantee the best ES closed-loop performance and an additional tuning process might be required. However, this valuable information can give us the starting point for the effective parameter calibration of the ES control algorithm. Based on the selected ES parameters the

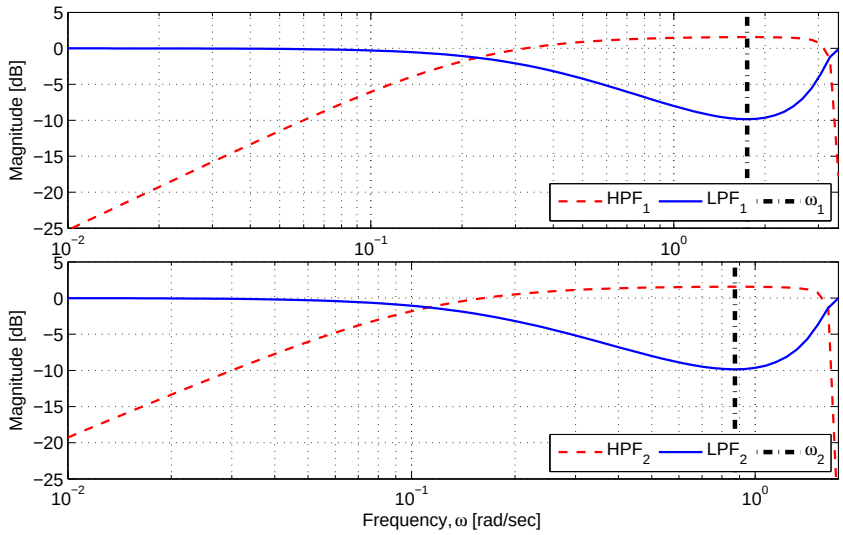

Figure 5.16 Bode plots of the discrete low- (red dashed line) and high-pass (blue solid line) filters from the spark ES controller (top) and the VVT ES controller (bottom).

closed-loop ES performance with the engine model is shown in the following section.

5.3.3 Simulation Verification

We first test the ES control algorithm shown in Fig. 5.14 for the spark timing and VVT separately at the engine speed of 2000 RPM using the ES parameters calibrated previously and the simulation results are shown in Fig. 5.17. The spark timing ES control performance is shown in Fig. 5.17(a) with the initial spark timing $\theta_\sigma[0]$ = -15 CAD and a fixed VVT of 48 CAD overlap. Fig. 5.17(b) shows the VVT ES performance starting from no valve overlap (i.e. VVT(0) = 0 CAD) while the spark timing is fixed at $\theta_\sigma[0]$ = -28 CAD aTDC during the simulation.

The first row in Fig. 5.17(a) shows the spark timing θ_σ and associated combustion phase θ_{CA50}. The filter signals from the discrete low- and high-pass filters of the spark ES are presented in the second row, while throttle feedback signal to regulate NMEP at 5 bar and the engine NSFC are shown in the third, respectively. The first row in Fig. 5.17(b) shows the VVT and its corresponding internal residual gas fraction x_{RG} and the others in the second and third row are same as ones in Fig. 5.17(a). For the spark ES control case, in approximately 20 seconds, the spark timing converges to the optimum θ_σ^* = -28 CAD aTDC. The converging time for the VVT ES control, on the other hand, takes about 45 seconds, twice of the spark ES only simulation. The numbers of perturbations for both spark and VVT to converge to their optimums, however, are similar with 12 spark excitations (Fig. 5.17(a))

and 13 VVT excitations (Fig. 5.17(b)). The longer convergence time from the VVT ES simulation is mainly from the sampling frequency difference (i.e. ΔT_1 = 1.8 and ΔT_2 = 3.6 seconds). Once the ES control variables converge to the optimum value, the filtered signal fluctuations from the low- and high-pass filters become stable due to no significant NSFC change.

The two ES controller for the spark timing and VVT are then combined and tested together using the engine model and the same values of the ES control parameters as the ones above are utilized for this combined ES control simulation. Two different VVT positions are chosen as initial values away from the optimal VVT position; one with no valve overlap (VVT[0] = 0 CAD) and the other with larger valve overlap than the optimal value (VVT[0] = 70 CAD), while the initial spark timing is retarded from the optimum (θ_σ = -15 deg aTDC) for both VVT[0]. The states of the discrete ES controller $x_i[k]$ for i = 1 and 2 are initialized at the initial spark timing and overlap values for each simulation when the ES is turned on. The evolution of θ_σ, VVT overlap (EVC - IVO) and the throttle feedback signal θ_{th} are shown on the left column in Fig. 5.18. The right column shows the corresponding engine performance variables such as θ_{CA50}, x_{RG} and NSFC. The corresponding trajectories of the two state dynamics, $x_1[k+1]$ and $x_2[k+1]$, and excited $\theta_\sigma[k]$ and $VVT[k]$ for two different initial conditions are shown in Fig. 5.19.

After approximately 30 excitations of θ_σ (corresponding to 54 seconds) and 15 excitations of VVT (54 seconds) with the initial variables of $\theta_\sigma[0]$ = - 15 deg aTDC and VVT[0] = 0 CAD, both ES variables converge to the optimal values of θ_σ^{opt} = -27.5 deg aTDC and VVT^{opt} = 48 CAD. In the case with $\theta_\sigma[0]$ = - 15 deg aTDC and VVT[0] = 70 CAD, the ES controller takes similar time to find both optimal θ_σ and VVT values but it undershoots.

5.4 Conclusion

This chapter presents a phenomenological combustion model which accounts for the cyclic combustion variability with the combustion phase θ_{CA50} variance as a function of the iEGR. The mean effective pressure model is then determined based on θ_{CA50} and intake and exhaust manifold pressure measurements. Along with the θ_{CA50} variation the combustion efficiency was also modeled as a function of iEGR level. The engine model can demonstrate the optimal engine operating condition with respect to spark timing and VVT in addition to the realistic noise level of important engine performance outputs such as θ_{CA50}, IMEP, NMEP and NSFC. Experimental implementation will be pursued in the next chapter.

The model detailed in the first part of the chapter allows us to tune and test the on-line

optimization scheme such as the extremum seeking controller to search the optimum of engine inputs for the idle and cruise conditions. The ES algorithm can be used to optimize any other operating conditions with long residence time since the current ES algorithm will converge and is enabled only at steady-state driving conditions. The on-line optimization scheme can alleviate the heavy calibration burden required especially for the engines equipped with many control actuators and hence many degrees of freedom. The designed extremum seeking algorithm shows that both spark timing θ_σ and VVT values can converge to the optimum within 60 seconds even though this convergence rate may be engine and vehicle specific.

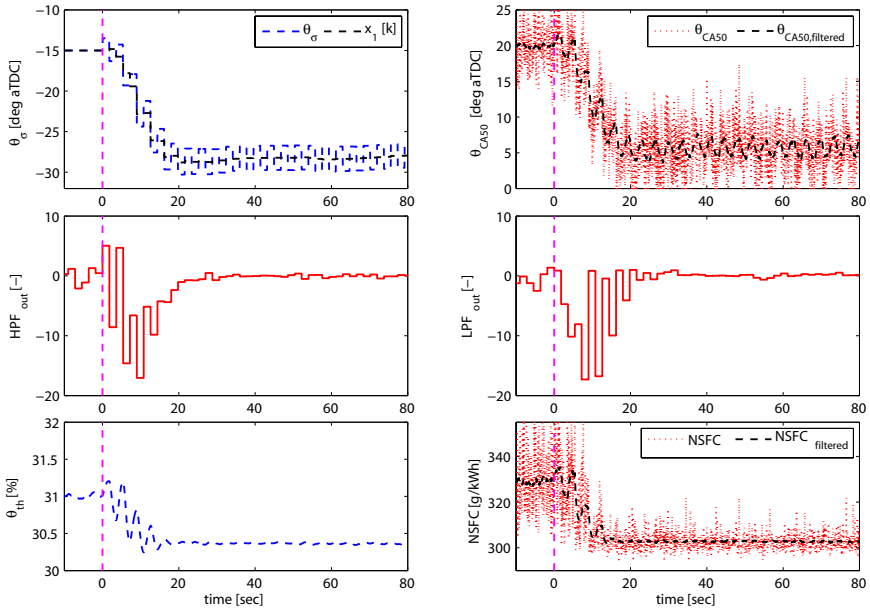

(a) Extremum seeking of spark timing only with the initial $\theta_\sigma(0)$ = - 15 CAD aTDC with a fixed VVT = 48 CAD

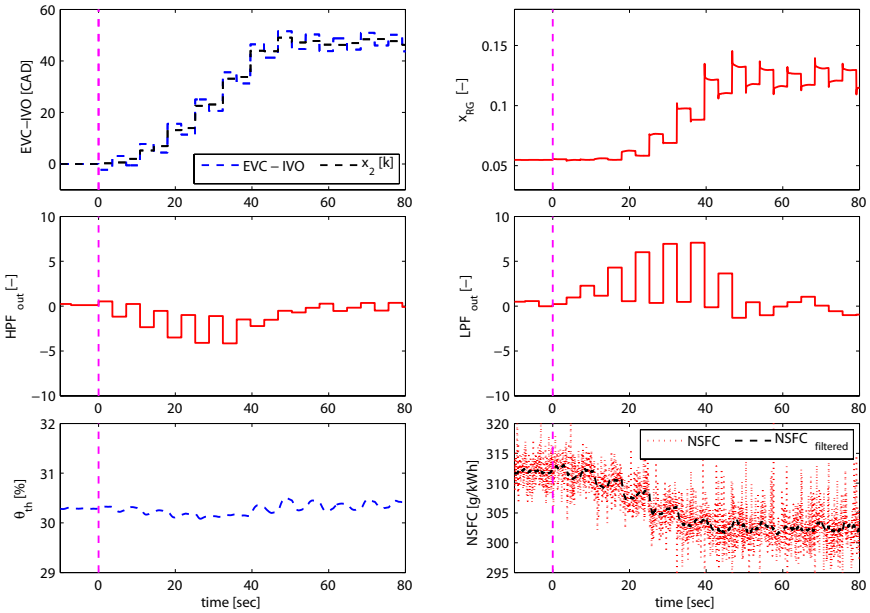

(b) Extremum seeking of VVT only with the initial VVT(0) = 0 CAD with a fixed θ_σ = -28 CAD aTDC

Figure 5.17 The simulation of ES convergence to the optimum of θ_σ and valve overlap (i.e. EVC - IVO) was tested separately and the internal signals of the ES controller such as load- and high-pass filters are presented in the second row.

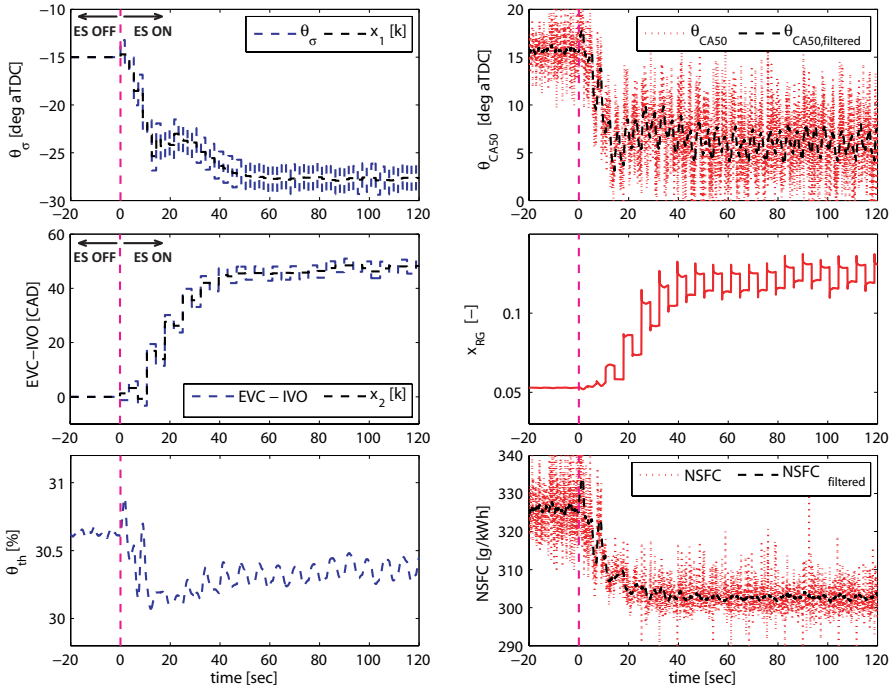

(a) Extremum seeking with the initial variables of VVT(0) = 0 CAD and $\theta_\sigma(0)$ = -15 deg aTDC

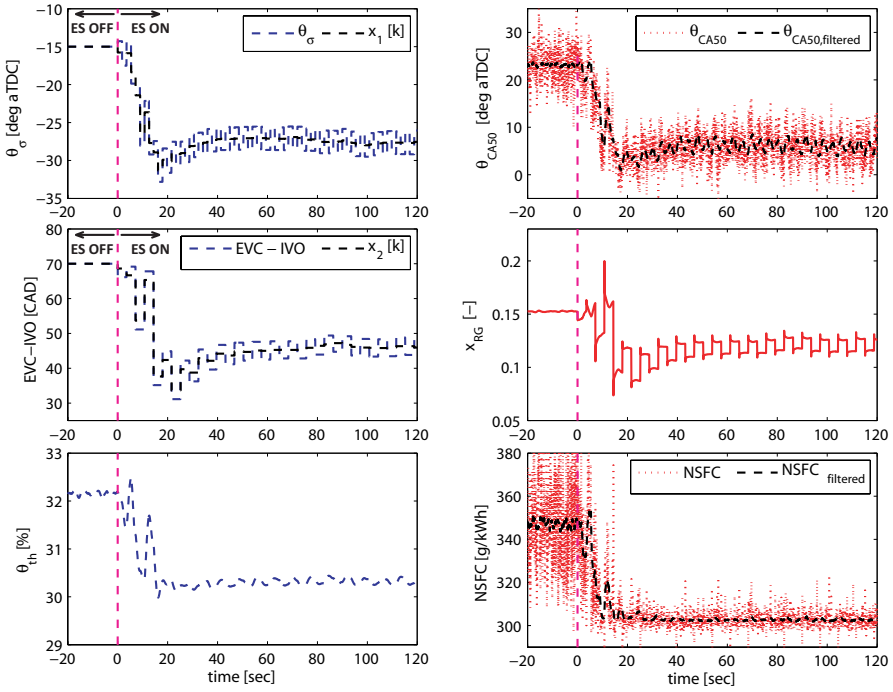

(b) Extremum seeking with the initial variables of VVT(0) = 70 CAD and $\theta_\sigma(0)$ = -15 deg aTDC

Figure 5.18 The ES convergence to the optimum of θ_σ and the valve overlap (i.e. EVC - IVO) for two different initial values along with the feedback signal of throttle angle θ_{th} are shown on the left column and the corresponding engine performance of θ_{CA50}, x_{RG} and NSFC are plotted on the right column.

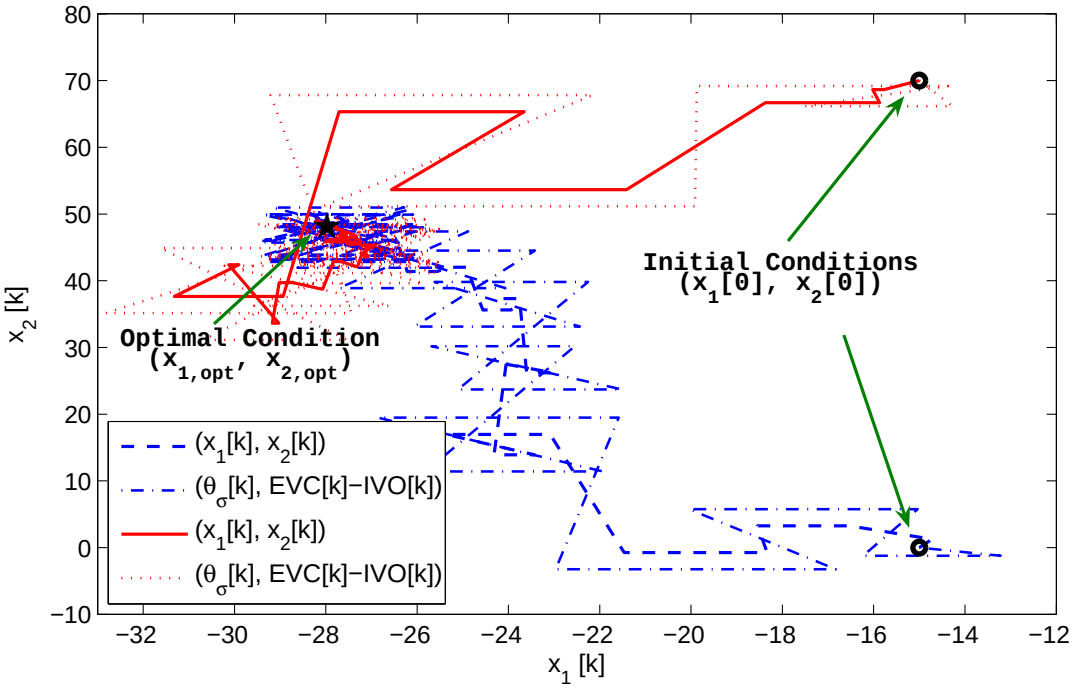

Figure 5.19 Extremum seeking control trajectory.

Chapter 6

Implementation of Extremum Seeking Control for Spark Timing

6.1 Introduction

An extremum seeking (ES) control algorithm for both spark timing and variable valve timing (VVT) has been proposed in the previous chapter and tested with an engine mean value model (MVM) to better understand the closed-loop engine system response. Based on the engine MVM characteristic, the parameters in the ES algorithm have been designed and tested. To verify the ES algorithm before implemented in a real vehicle, we implemented the ES algorithm in a dynamometer engine, which allows us to have more controllable test conditions than a real vehicle.

This chapter focuses on the implementation and verification of the ES control algorithm in a dynamometer engine. First, the engine characteristics of a modified new engine are introduced and analyzed and the experimental setup of a dynamometer facility used for the ES control algorithm verification is following. The ES algorithm test is conducted at various engine conditions, i.e. different engine speeds and loads. Both the steady-state and transient conditions are test. Transient load inputs with a sinusoidal form are applied to demonstrate the ES algorithm under non-steady driving conditions resembling a real driving profile.

6.2 Experimental Setup

The turbo charged (TC) spark ignition direct injection (SIDI) engine with VVT has been modified from the engine modeled in Chapter 5 primarily to have a higher compression ratio and different variable valve cam profile. The modifications in the engine hardware were part of a parallel efforts to better utilize the positive properties of E85 without com-

promising E0 performance. The cylinder compression ratio has been changed from 9.25 to 10.8 while intake valve open duration was increased from 230 to 264 crank angle degree (CAD). Therefore, in this section, we present spark ignition timing and variable valve timing effects on net specific fuel consumption (NSFC). The ES control algorithm proposed initially in Chapter 5 is slightly modified to be implemented into a dynamometer engine.

6.2.1 Engine Characteristics

In this section, the effects of two actuators, the spark timing and VVT, on NSFC are introduced and discussed. Two different tests were conducted to understand how the spark timing and variable valve timing affect engine combustion performance:

- various spark timings have been applied with other engine inputs fixed such as variable valve timing (VVT), throttle angle θ_{th} and air-to-fuel ratio (AFR) and
- intake valve cam timing has been changed with other engine inputs fixed such as spark timing θ_{σ}, throttle angle θ_{th} and AFR.

Spark sweep from -27 to - 11 CAD aTDC has been conducted at the relative load (RL[1]) of 50% and engine speed of 2000 RPM as shown in Fig. 6.1. Top two subplots show NMEP and NSFC for different spark timings while the two in the bottom present NMEP and NSFC for corresponding combustion phases θ_{CA50}. At the same engine operating condition, the intake valve open timing sweep from -8 to -32 CAD aTDC has been also applied as shown in Fig. 6.2. Notice that only the intake valve cam timing has been changed with fixed exhaust cam position (exhaust valve close at 20 CAD aTDC) since it has more dominant effect on internal residual gas recirculation (iEGR) due to longer valve open duration. The two plots in the top show NMEP and NSFC for various intake valve openings (IVO) and the two in the bottom show combustion phase θ_{CA50} and load changes for the same IVO range. The error bars in these two figures indicate standard deviation of each variable.

For different spark timing sweep, NMEP and NSFC curves follow a parabolic shape with the maximum fuel efficiency at θ_{CA50} between 5 and 10 CAD aTDC, which, in turn, allows us to apply the extremum seeking algorithm. For instance, we can increase approximately 3% fuel efficiency if spark timing θ_{σ} is advanced by 5 CAD from -17.5 to -22.5 CAD aTDC (i.e. θ_{CA50} from -15 to -10 CAD aTDC). Fuel efficiency improvement rate increases exponentially as the corrected spark timing angle increases. There exists a relatively flat area in both NMEP and NSFC curves around maximum fuel efficiency area at spark timing θ_{σ} between -27 and -22.5 CAD aTDC (θ_{CA50} between 5 and 10 CAD aTDC).

[1]Relative Load (RL) in SI engines is generally defined as the actual torque (or actual cylinder air charge) divided by the maximum possible torque (or maximum air charge) without the turbo boost.

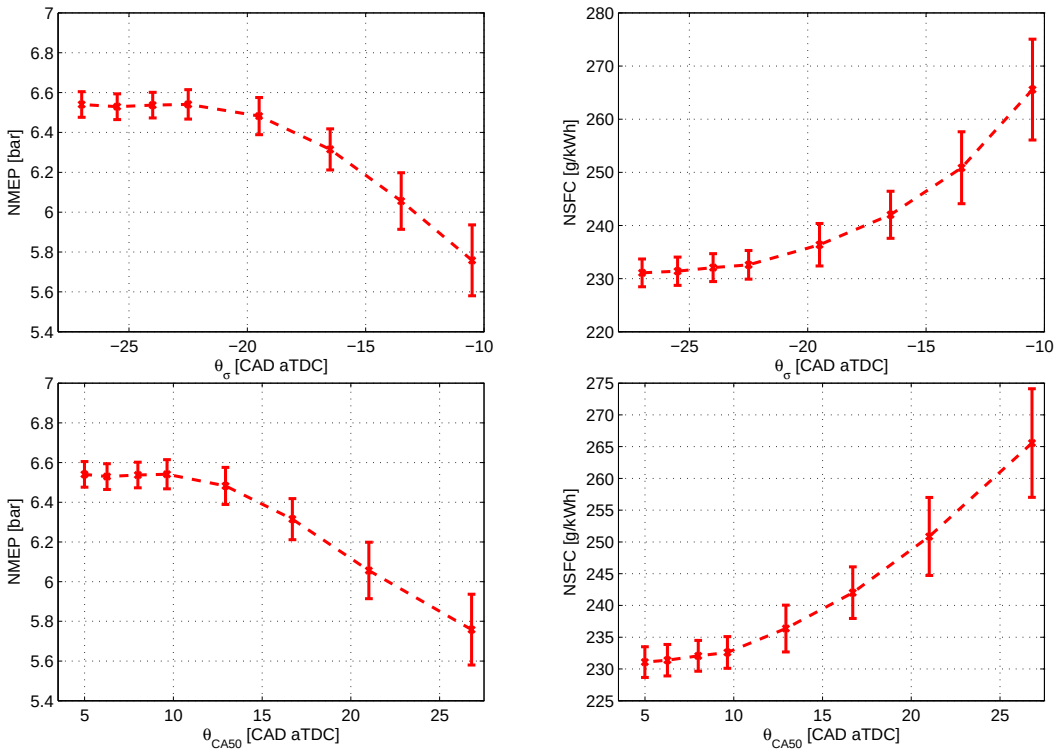

Figure 6.1 NMEP and NSFC for various spark timing and corresponding combustion phase (θ_{CA50}) at N = 2000 RPM and Relative Load = 50%

Change of intake valve open timing affects the combustion behavior of the new engine which is used for the experimental verification as previously explained in (5.1). Advanced IVO introduces longer valve overlap (the portion of the operating cycle of engines when both the intake and exhaust valves are open) and higher iEGR. In Fig. 6.2, for instance, once IVO is advanced from -8 to -32 CAD aTDC, combustion duration increases due to increased iEGR and, hence, θ_{CA50} is retarded from 9 to 14 CAD aTDC. Spark timing during this IVO sweep was fixed such that each combustion for different IVO does not correspond to the maximum brake torque (MBT) condition. If we assume that the optimal combustion phase θ_{CA50} is identical at around 6 - 7 CAD aTDC for each IVO position, NSFC of 241 g/KWh at IVO = -32 CAD aTDC can be improved by approximately 7 g/kWh based on the relationship between θ_{CA50} and NSFC in Fig. 6.1 (the second subplot in the bottom). Hence, there is no significant engine combustion efficiency improvement through IVO despite the original expectations.

Engines with a higher compression ratio and longer intake valve open duration could potentially gain in combustion efficiency by VVT. In general, for the experimental engine considered, the internal residual gas recirculation (iEGR) changes through VVT seems to be insensitive for most of engine operating conditions except at very low load close to

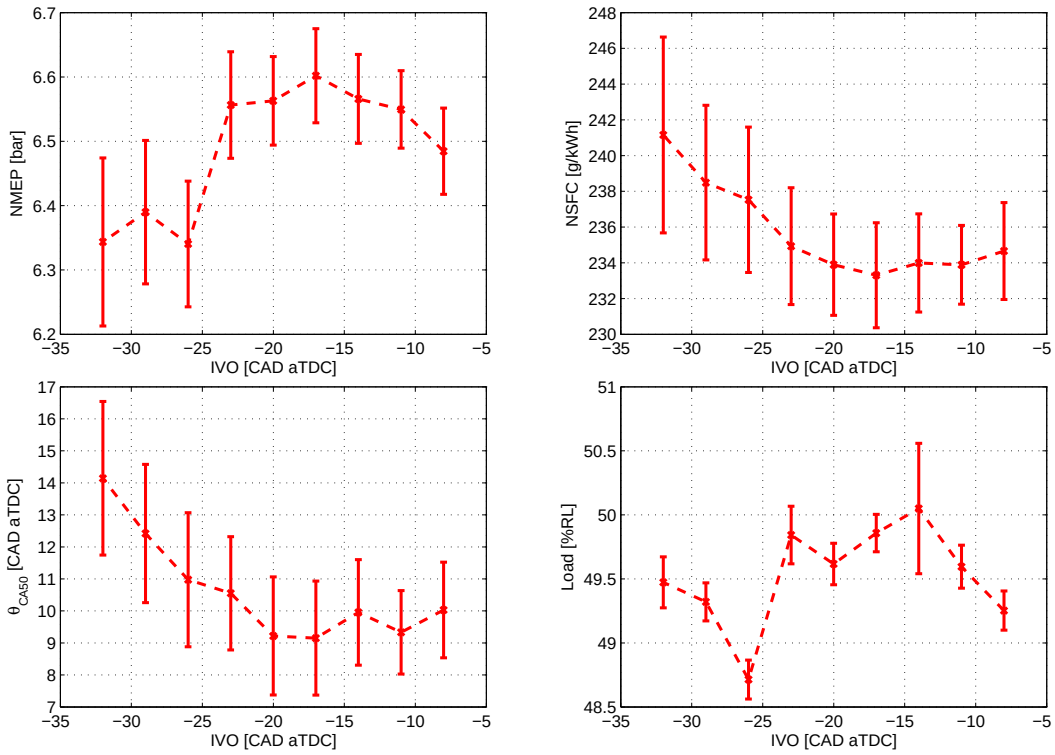

Figure 6.2 NMEP, NSFC, combustion phase (θ_{CA50}) and load for various intake valve open timing at N = 2000 RPM and Relative Load = 50%

idle. Finally, due to the limitation of in-cylinder pressure analyzer capability, the engine in-cylinder pressure is measured only for the engine compression and expansion strokes, and is not available for the intake and exhaust strokes. Hence, the computation of pumping mean effective pressure (PMEP) was not viable and, instead, estimated using (5.4) from the measured intake p_{im} and exhaust p_{em} manifold pressures. The associated estimation error propagates into NMEP and NSFC calculation and would lower the confidence level of them. For these two reasons and due to the time and budget limitations associated with the dynamometer verification, a decision was made to concentrate and validate the ES control for the spark timing only.

6.2.2 Software and Communication Setup

For the experiment, a 2 L 4 cylinder turbocharged SIDI flex-fuel engine with VVT was used and the specifications of the engine is summarized in Table 6.1. The experimental setup at the engine dynamometer, as illustrated in Fig. 6.3, consists of the Bosch MED17.3.2 ECU for engine controls, ETAS ES1000 VME for rapid prototyping, and A&D Redline CAS II System for real-time combustion analysis. The ETAS ES1000 VME rapid prototyping

Table 6.1 Specifications for the optimized FFV engine

Description	Value
Cylinder chamber volume	551.0 mm^3
Cylinder chamber displacement volume	500.0 mm^3
Cylinder chamber clearance volume	51.0 mm^3
Compression ratio	10.8:1
Valve timing (all angles at 0.25 mm lift)	
Intake valve open duration	264 CAD
Exhaust valve open duration	221 CAD

system communicates with the ECU and a computer via Controller-Area Network (CAN) and Ethernet respectively.

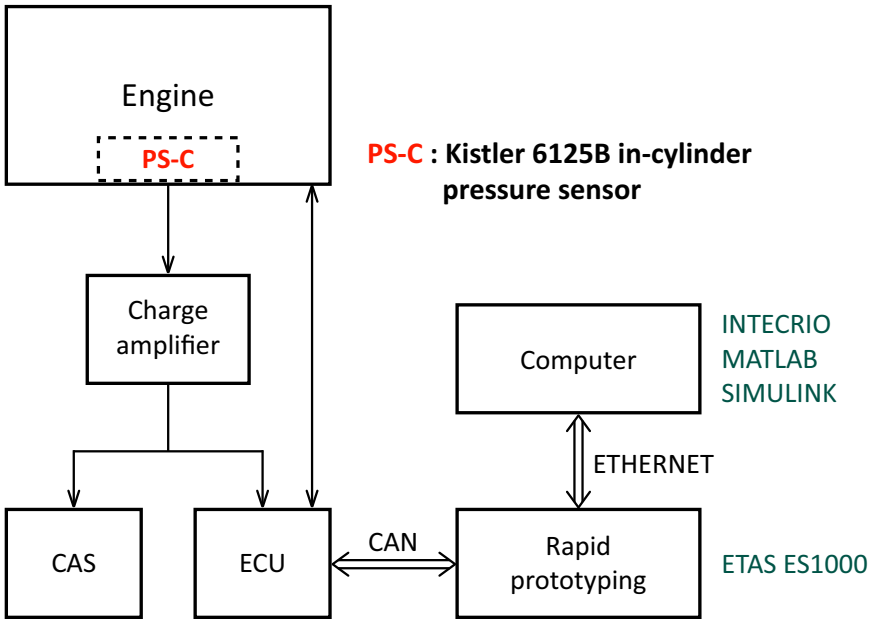

Figure 6.3 Experimental setup at the engine dynamometer.

With the cylinder pressure sensing capability integrated, the Bosch MED17.3.2. ECU is able to acquire the cylinder pressure measurements and conduct real-time calculation of various key combustion features such as the crank angle at 50% mass fraction burn θ_{CA50} and indicated mean effective pressure (IMEP). In this study, Kistler 6125B cylinder pressure sensors are installed in each cylinder, whose outputs are converted into voltage signals via an external charge amplifier for the engine control unit (ECU) and combustion analysis system (CAS).

The rapid prototyping environment in Fig. 6.4 is set up to verify and validate new control and diagnostic functions under target operation conditions on a PC or experimentation system [87]. The proposed virtual prototyping environment includes the following software and hardware components.

- INTECRIO: an open environment that enables the integration of AUTOSAR software components as well as MATLAB®/Simulink® and ASCET models plus C code modules,
- ASCET software components: ASCET-MD for modeling and design, ASCET-SE for software engineering, ASCET-RP for rapid prototyping,
- MATLAB®/Simulink® with Real-Time Workshop® and Embedded Coder,
- ES1000 VME boards and housing: scalable rapid prototyping module that combines real-time calculation power with all relevant ECU bus interfaces, real-time analog and digital I/O to connect sensors and actuators, as well as customizable rapid prototyping boards.

In the integrated algorithm test, the spark ES controller was implemented through the rapid prototyping. The measured combustion phases and IMEP were calculated in the ECU using the in-cylinder pressure measurements and provided to the rapid prototyping for the ES control algorithm.

6.3 Extremum Seeking Control Verification

The implemented extremum seeking (ES) control structure in a dynamometer engine is shown in Fig.5.14, which excludes the VVT ES control part from Fig. 6.5. The proposed spark timing ES control algorithm is validated using both a mean-value engine model simulation and a experimental engine test in a dynamometer facility. Simulated ES performance is first introduced using the calibrated engine model based on the new engine specification in Table 6.1. And the ES control experimental results from the dynamometer test are discussed in the followings. Note that, for both simulation and experiment verifications, some minor modifications are also introduced such as the ES turn-on/off strategy with engine load and speed ranges and the sinusoidal excitation signal turn-off criteria at steady-state after the ES convergence occurs.

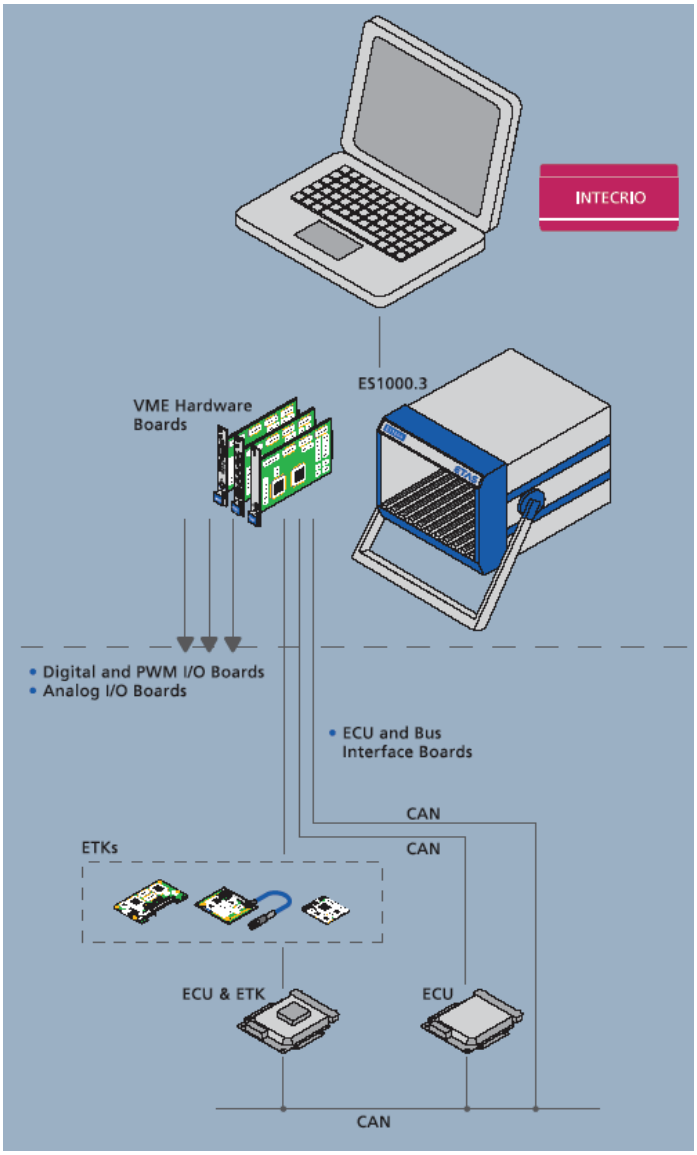

Figure 6.4 Proposed rapid prototyping scheme with ES1000 VME [87].

6.3.1 Simulation Verification

A retarded spark timing with 12 CAD (i.e. $\Delta\theta_{\sigma,0}$ = 12 CAD) is chosen as an initial value away from the nominal (pre-calibrated) optimum. The extremum seeking controller performance using the mean-value model is shown in Fig. 6.6. The first column presents a commanded engine relative load profile *RL*, spark timing θ_σ and corresponding combustion phase θ_{CA50}. The second column shows the ES trigger, compensated spark timing $\Delta\theta_\sigma$ and the resulting net specific fuel consumption (NSFC) which drives the ES controller. The engine operating conditions for this simulation are selected as an engine speed of 2000 RPM and a relative load (RL) of 70%.

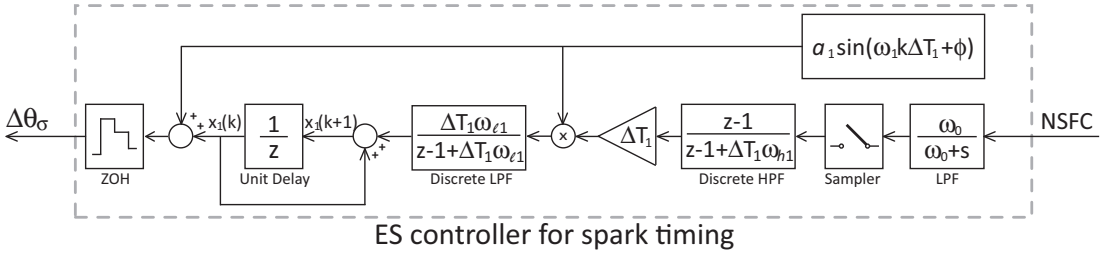

Figure 6.5 Extremum seeking control for the optimal spark timing θ_σ.

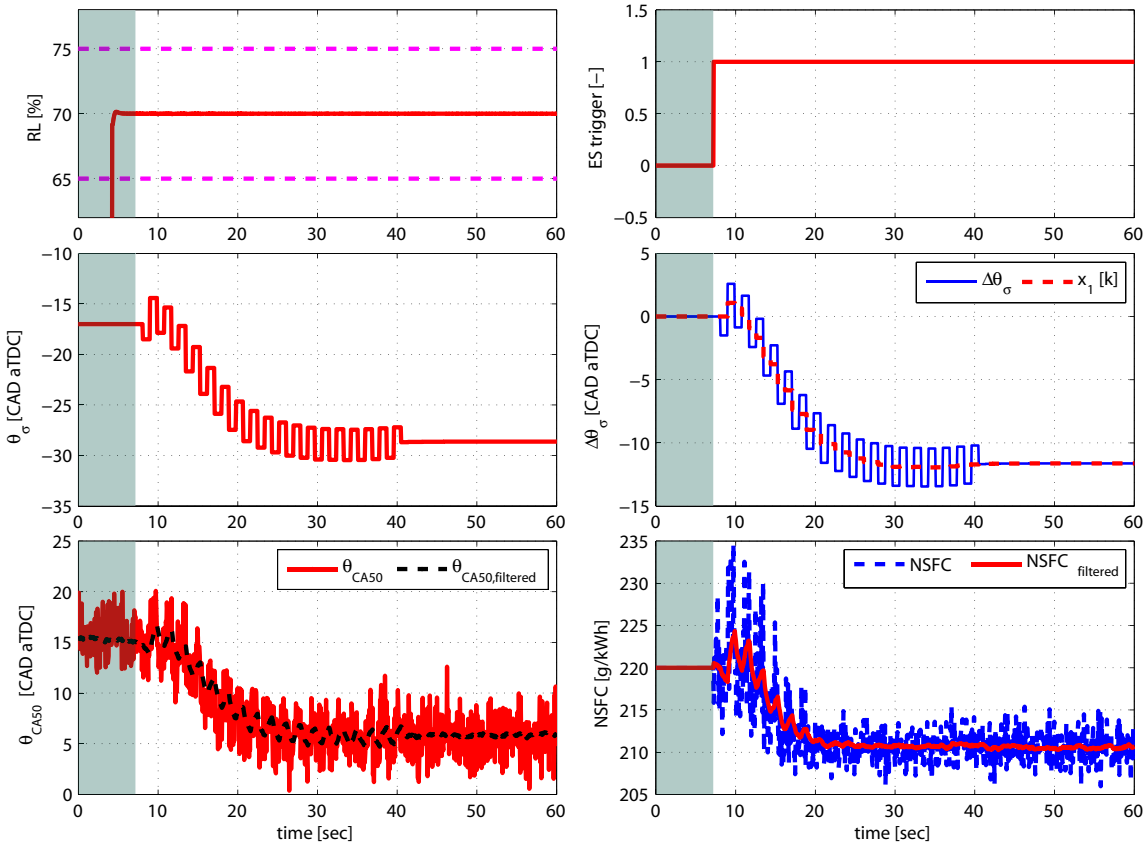

Figure 6.6 Extremum seeking control test result : N = 2000 RPM, Relative load = 70%, $\Delta\theta_{\sigma,0}$ = 12 CAD, fuel = E0.

We defined the ES target region as [65%, 75%] load with magenta dashed lines in the first subplot of the first column. The ES target area corresponds to the load range where the ES has been tuned. Once the engine visits the ES target area, the ES controller is turned on by the ES trigger and starts searching the optimum. The state of the discrete ES controller dynamics x_1 is initialized at zero so that it can be used to update the spark timing map in the ECU after searching for the optimal spark timing. In the simulation results, the ES algorithm drives the combustion phase θ_{CA50} to move from 16 to 6 CAD aTDC while NSFC decreases from 223 to 211 g/kWh (approximately 5.4% efficiency improvement). It

takes about 20 seconds to reach the optimum θ_σ = 28 CAD aTDC. After converging to the optimal spark position with a small variation of x_1 less than a threshold value x_{min} for a certain number of the spark excitations n_σ, the ES spark excitation stopped at 40 seconds during the simulation.

6.3.2 Overview of Experiments

The same ES control algorithm for spark timing has been implemented and conducted in a dynamometer facility. It has been tested for two different engine speeds, N = 1500 and 2000 RPM. The associated relative load at N = 1500 RPM is 50% and the relative loads for N = 2000 RPM are 50% and 70%, respectively. For each engine speed and load condition, the nominal spark timing θ_σ values were perturbed with three different offsets (i.e. +12, +9 and +6 CAD) from the pre-defined ECU map[2] values to demonstrate the ES controller's ability to converge to the optimum. The reason for applying these offsets in the experiment is to fictitiously introduce different ECU spark timing bias from the optimum. Table 6.2 shows the engine operating conditions for the spark timing ES control test at fixed loads.

Table 6.2 Engine operating conditions for extremum seeking (ES) control test with fixed loads.

Engine speed N [RPM]	Relative Load [%]	Spark timing offset $\Delta\theta_{\sigma,0}$ [CAD]	Fuel [-]
1500	50	+6, +9, +12	E70
2000	50	+12, +9, +6	E85
	70	+12, +9, +6	E70

ES control algorithm is triggered to start seeking the optimum spark timing from the fictitiously perturbed spark timing once the engine visits the ES target engine speed and load. If the state $x_1[k]$ in the ES controller does not vary for a n_σ spark excitation period, the sinusoidal excitation signal is then turned off. The engine load is shifted to leave the ES target region for a while. To test the ES control repeatability the engine load is commanded to revisit the ES target region to restart searching the optimum from the spark timing converged to previously. The ES control scheme explained above has been five times and the convergence occurs for each test. Notice that the ES tested controller holds and freezes its state variables when the engine departs from the ES target region, and reutilizes them once the engine revisits the same target range. This allows the ES controller to restart searching

[2]The spark timing values stored in the ECU map were determined prior to the ES test with a conventional calibration analysis such as the Design of Experiment (DoE) method.

for the optimum from where it leaves.

Long steady-state driving duration in a vehicle are rarely accomplished even in a cruise condition due to unexpected torque disturbances such as curves and altitude changes in the load. To be implemented in a real vehicle, therefore, the ES control algorithm needs to be feasible even under small variations in both engine load and speed. Since the optimal spark timing is more sensitive to engine load than engine speed, ES control tests have been conducted under various sinusoidal load conditions. At the engine speed of 2000 RPM and mean relative load of 50%, for instance, sinusoidal load inputs with two different amplitudes A_{RL} were commanded to produce a load variation. For each sinusoidal amplitude, the frequency f_{RL} has been increased from 0.01 to 0.15 Hz as shown in Table 6.3. Note that initial spark timing was perturbed by +12 CAD from the optimum value stored in a ECU map.

Table 6.3 Engine operating conditions for extremum seeking (ES) control test with sinusoidal loads.

Spark timing offset $\Delta\theta_{\sigma,0}$ [CAD]	A_{RL} [%]	f_{RL} [-]	Fuel [-]
+12	3	0.01, 0.05, 0.10, 0.15	E85
+12	5	0.01, 0.05, 0.10	E85

Nominal engine speed N = 2000 RPM, relative load RL = 50%.

Similar to the ES test with fixed loads, the ES controller starts searching for the optimal spark timing once the engine visits the target range of engine speed and load. To check the repeatability of the ES solution given a sinusoidal load, the engine nominal condition is shifted for a moment after the ES convergence occurs. Similarly to the steady-state experiments the resetting and ES test has been repeated five times.

6.3.3 ES Verification under Fixed Load

Some of dynamometer engine test results with fixed load conditions are shown in Fig. 6.7 through 6.9. The first column of each figure shows relative load (RL), spark timing θ_σ and associated crank angle of 50% fuel burned θ_{CA50} from top to bottom. The second column represents ES control trigger signal, compensated spark timing from the nominal spark value stored in the ECU map $\Delta\theta_\sigma$ and net specific fuel consumption (NSFC) measurement.

Fig. 6.7 emulates steady-state driving conditions at N = 2000 RPM and RL = 70%. At this condition, the nominal spark timing in the ECU map has been identified through the

conventional calibration process as θ_{σ}^{*} = -19 CAD aTDC with resulting combustion phase θ_{CA50} = 10 CAD aTDC. The target range of the ES control is [1900 RPM, 2100 RPM] engine speed and [65%, 75%] relative load. The first test in Fig. 6.7 is initiated by retarding the spark from the ECU value by 12 CAD (from -19 to -7 CAD). The load is perturbed at the time of 45, 75, 105 and 140 seconds to exit the target load range for a few seconds before returning to the target range. For five iterations of the ES test, the ES controller converges to the minimum NSFC = 196 g/kWh. The determined optimal spark timings are -23.5, -22.75, -23.5, -21.25 and -22.75 CAD aTDC with an average of -22.75 CAD aTDC, which causes a combustion phase θ_{CA50} at 6 CAD aTDC.

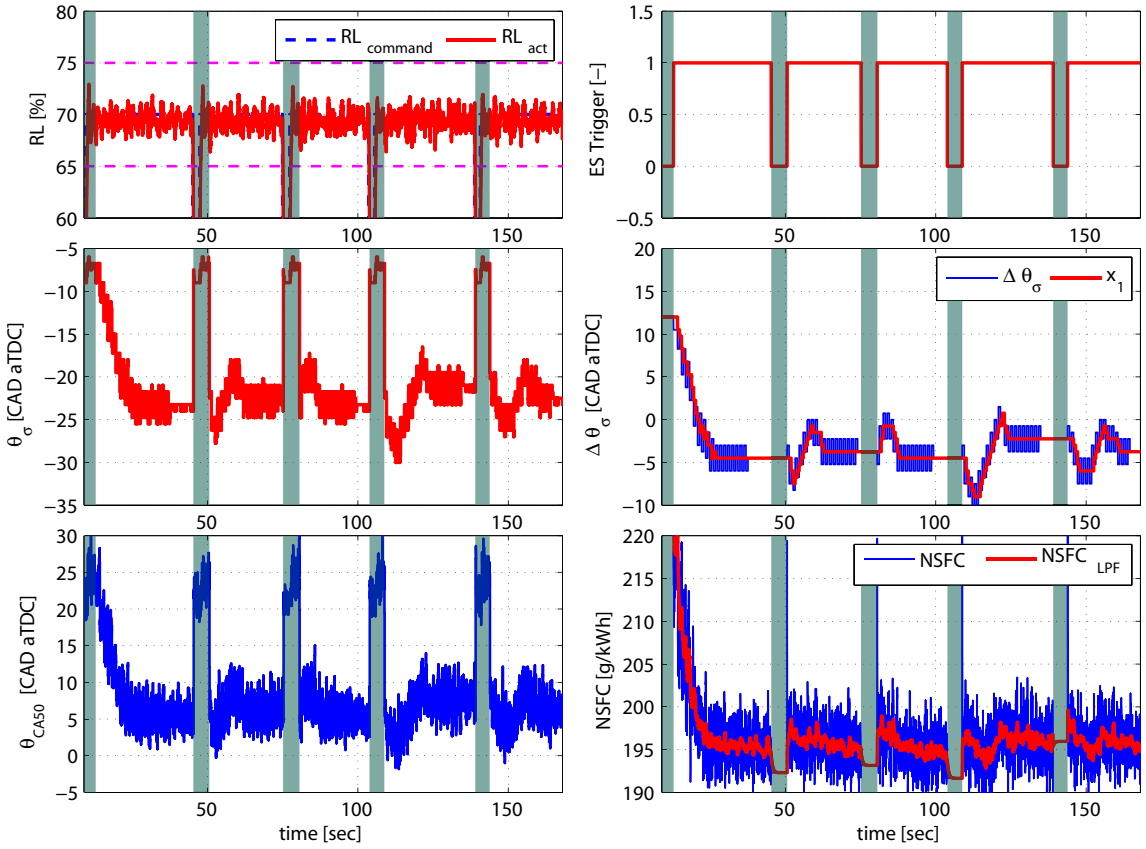

Figure 6.7 Extremum seeking control test result : N = 2000 RPM, Relative Load = 70%, $\Delta\theta_{\sigma,0}$ = 12 CAD, fuel = E70.

Fig. 6.8 shows similar experiments with the ones in Fig. 6.7 except the initial spark timing shift of $\Delta\theta_{\sigma,0}$ = 9 CAD (retarded from -19 to -10 CAD aTDC). The optimal spark timings for the five load perturbations are found as θ_{σ} = -23.5, -22.75, -21.25, -25 and -25 CAD aTDC, and the resulting spark timing on average is θ_{σ} = -23.5 CAD aTDC, which is very similar to the case shown in Fig. 6.7. Note that corresponding combustion phase $theta_{CA50}$ for this optimal spark timing is approximately 5.5 CAD aTDC, which achieves NSFC of 195 g/kWh.

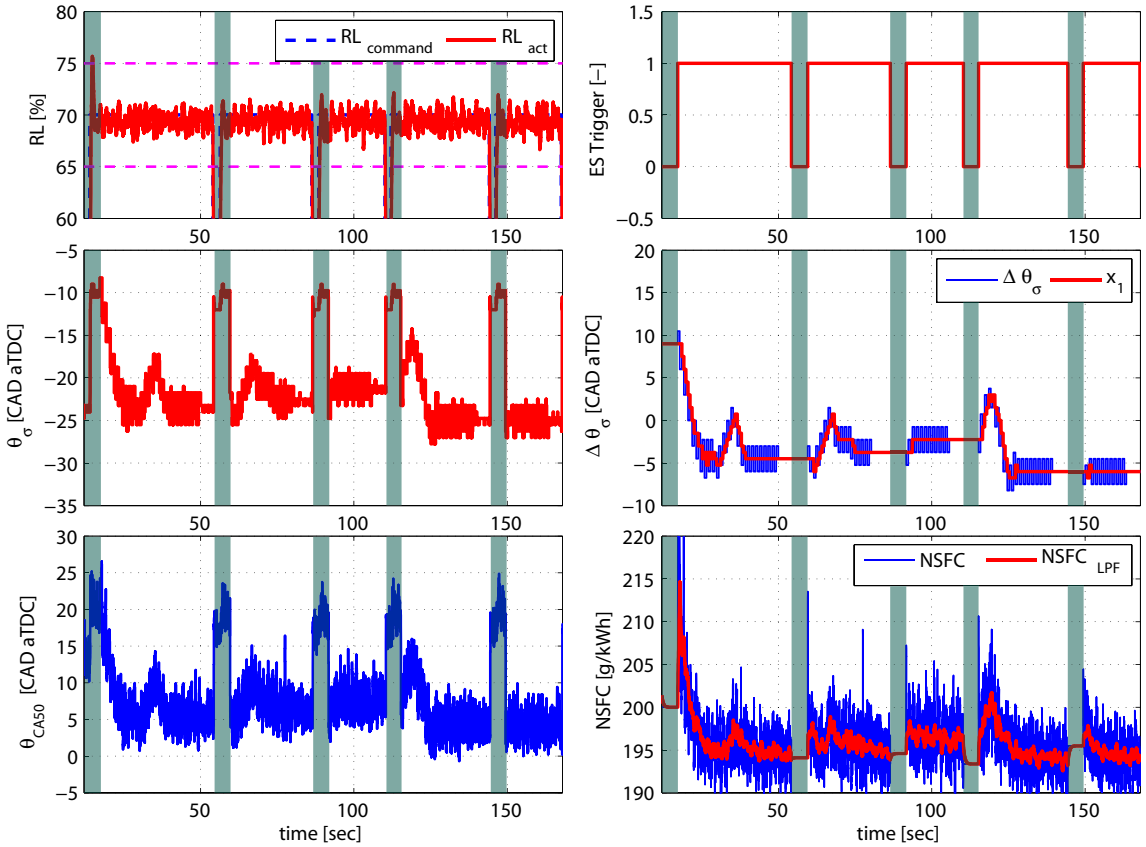

Figure 6.8 Extremum seeking control test result : N = 2000 RPM, Relative Load = 70%, $\Delta\theta_{\sigma,0}$ = 9 CAD, fuel = E70.

Finally, as shown in Fig. 6.9, spark timing has been retarded less aggressively by 6 CAD from ECU at the same engine operating conditions as ones shown in Fig. 6.7 and 6.8 so that the ES test is initiated from θ_σ = -13 CAD aTDC. The optimal spark timings are determined as -25, -22, -21.25, -27.25 and -23.5 CAD aTDC, respectively, after each convergence occurs. Despite small variations in the resulting optimized spark timing and associated θ_{CA50}, however, corresponding NSFC is within 1 g/kWh (between 195 and 196 g/kWh). The NMEP and NSFC flatness around the optimum as shown in Fig. 6.1 is the primary reason for the small variability in the converged θ_σ.

The ES control algorithm was tested for three different initial spark timings $\Delta\theta_{\sigma,0}$ = 12, 9 and 6 CAD (i.e. the initial spark timing θ_σ = -7, -10 and -13 CAD aTDC) at the engine speed of 2000 RPM and relative load of 70%. Although optimal spark timing has variations between -8.25 (the most advanced optimal spark timing) and -2.25 (the most retarded optimal spark timing), accumulative moving averages after fifth iteration of spark timing optimization demonstrate negligible variation with -4.8, -4.5 and -3.75, respectively. It takes approximately less than 20 seconds to converge to optimal spark position for most

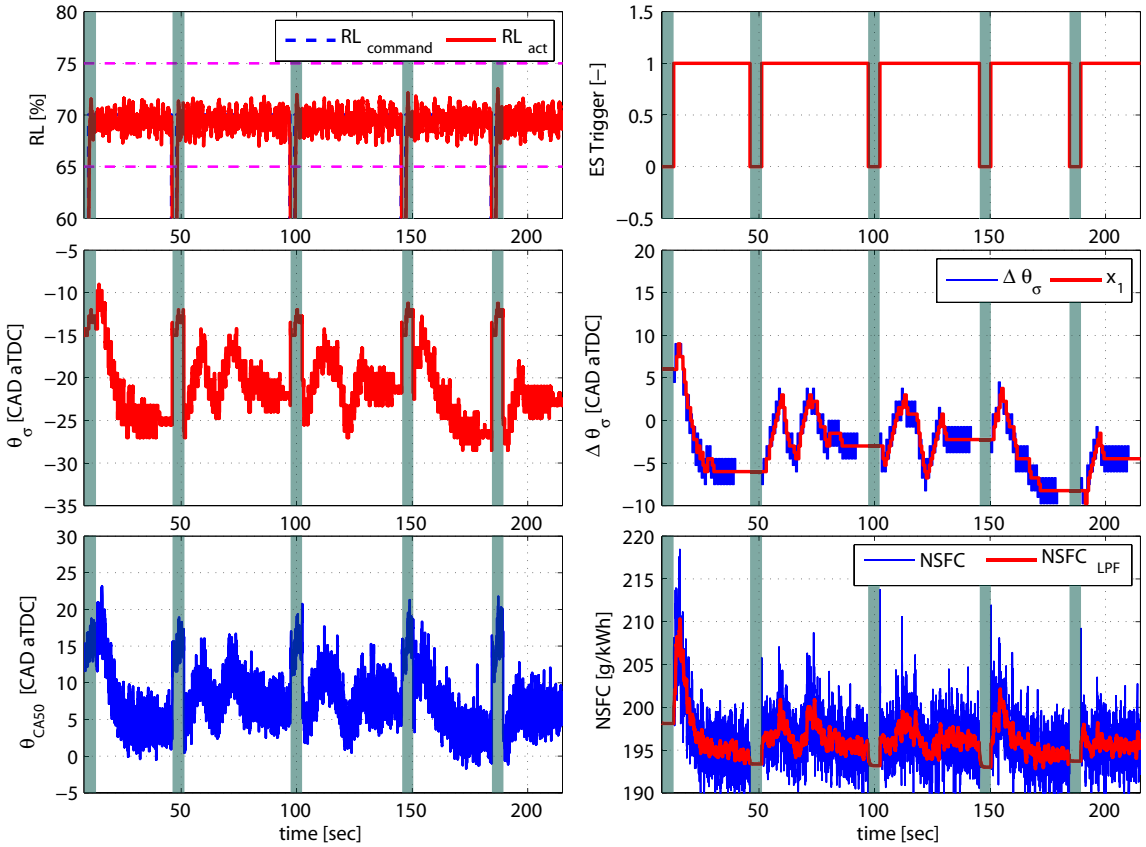

Figure 6.9 Extremum seeking control test result : N = 2000 RPM, Relative load = 70%, $\Delta\theta_{\sigma,0}$ = 6 CAD, fuel = E70.

of iterations. Notice that very similar ES control performances have been observed from other dynamometer engine test data for different engine speeds and loads, in which, we used same values for the parameters in the implemented ES control algorithm.

6.3.4 ES Verification under Sinusoidal Load

In this section, we present the experimental results of the implemented ES control algorithm in the dynamometer engine under sinusoidal load conditions. Notice that the sinusoidal load excitation is introduced by an electronic throttle actuator while air-to-fuel ratio (AFR) is always fixed at stoichiometric and variable valve timing (VVT) is managed via the ECU map. Test results at the engine speed of 2000 RPM and relative load of 50% are presented in Fig. 6.10 through 6.13. The contents of these figures are identical with ones in the previous section. The blue dashed line in the first top subplot is demanded relative load signal while the red solid line indicates achieved relative load in the dynamometer engine. For the experiment with sinusoidal loads we measure indicated specific fuel consumption (ISFC)

instead of NSFC as shown in the last subplot of first column.

We first applied a slow and small sinusoidal load superimposed on top of the fixed load input (50% RL) with an amplitude A_{RL} of 3% RL and a frequency f_{RL} of 0.01 Hz (or a half period of 50 seconds) as shown in Fig. 6.10. The base spark timing during the sinusoidal load excitation is commanded by the ECU map in addition to the ES compensation spark signal $\Delta\theta_\sigma$, which causes a comparatively constant combustion phase around the local target engine operating ranges. We also assume that the NSFC variation from the load excitation is relatively small compared with its variation from the spark timing changes. Therefore, the ES control for the optimum spark timing can be applicable even under small load excitations in the ES target range. Unlike the steady-state load tests, the base spark timing from the ECU map varies during ES so that we compare the compensated spark timing signal $\Delta\theta_\sigma$ to evaluate the ES performance. As before, the load was periodically perturbed outside the target ES range, causing the ES to stop and restart after ES convergence. The spark converges all five times at t = 86, 109, 162, 189 and 227 seconds with corrected spark timing $\Delta\theta_\sigma$ = 3.75, -0.75, -3, -7.5 and 0.75 CAD (i.e. -1.35 CAD on average), which achieves the combustion phase θ_{CA50} between 2 and 10 CAD aTDC. The associated ISFC ranges from 185 to 188 g/kWh, which clearly shows a huge fuel efficiency increase from 205 g/kWh (approximately 9% fuel efficiency improvement) by spark timing advance of 13.35 CAD.

Fig. 6.11 emulates sinusoidal driving conditions of a higher frequency f_{RL} = 0.05 Hz (a half period of 10 seconds) with the same amplitude A_{RL} of 3% RL as shown in Fig. 6.10 at N = 2000 RPM and RL = 50%. The target range of the ES control is [1900 RPM, 2100 RPM] engine speed and [40%, 60%] relative load. The initial spark timing was retarded by $\Delta\theta_{\sigma,0}$ = 12 CAD from the ECU value, which corresponds to the combustion phase θ_{CA50} of 22 CAD aTDC. It converges to θ_{CA50} = 5 CAD aTDC in 15 seconds after the first ES control. Corresponding ISFC level decreases from 210 to 180 g/kWh with an approximately 12% fuel efficiency increase. Compensated spark timings $\Delta\theta_\sigma$ after five ES tests are -4.5, -2.25, -1.5, 0.75 and -5.25 CAD with an average of -2.55 CAD (i.e. spark timing advance of 14.55 CAD after the ES test). Equivalent combustion phase θ_{CA50} varies within a 5 g/kWh variation from 3 to 8 CAD aTDC and ISFC varies from 185 to 186 g/kWh.

In Fig. 6.12 a frequency f_{RL} of sinusoidal load input is increased to 0.1 Hz (a half period of 5 seconds) with an amplitude A_{RL} = 3% RL. Values of the compensated spark timing $\Delta\theta_\sigma$ after converging are 0.75, -3, -4.5, 4.5 and -0.75 CAD for the five ES tests, which introduce a combustion phase θ_{CA50} located from 5 to 12 CAD aTDC and an associated ISFC between 185 and 189 g/kWh. Notice that, during the first and the fourth ES control in the test, the ES spark excitation stops at t = 30 and 155 seconds undesirably as

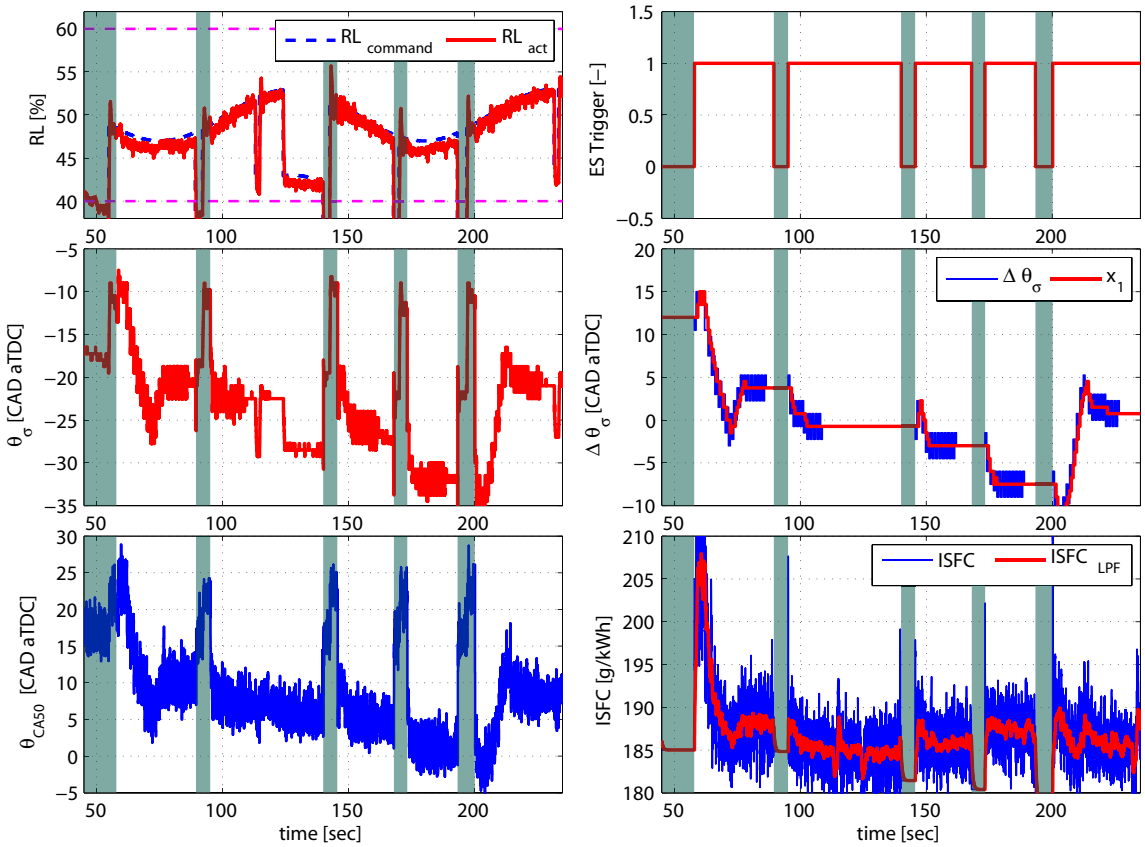

Figure 6.10 Extremum seeking control test result : N = 2000 RPM, Relative Load = 50%, $\Delta\theta_{\sigma,0}$ = 12 CAD, A_{RL} = 3%, f_{RL} = 0.01, fuel = E85.

shown in the second subplot of the second column (dashed circles), since the state x_1 in the ES controller meets the spark ES excitation stop criteria explained in the previous section 6.3.1. Specifically, the x_1 variation was less than a threshold x_{min} for a given number of the spark excitations n_σ. It is clear that a more sophisticated convergence criterion is needed for avoiding similar problems in vehicle implementation. Without these two ES cases, the converged values of $\Delta\theta_\sigma$ along with the associated θ_{CA50} and ISFC are comparable to the previous tests shown in Fig. 6.10 and 6.11.

We also conducted the ES control algorithm test with a sinusoidal load frequency f_{RL} of 0.15 Hz (a half period of 3.3 seconds) and its result is shown in Fig. 6.13. Due to the load variability the ES algorithm was always searching except at time 43 seconds where the first undesirable convergence happens with the same reason from the previous test in Fig. 6.12. The ES algorithm regulates the engine combustion phase θ_{CA50} in the range from 4 to 8 CAD aTDC and achieves ISFC between 185 to 189 g/kWh. This 3 to 4 g/kWh ISFC variation is primary due to the sinusoidal load changes as shown in the third subplot of the second column.

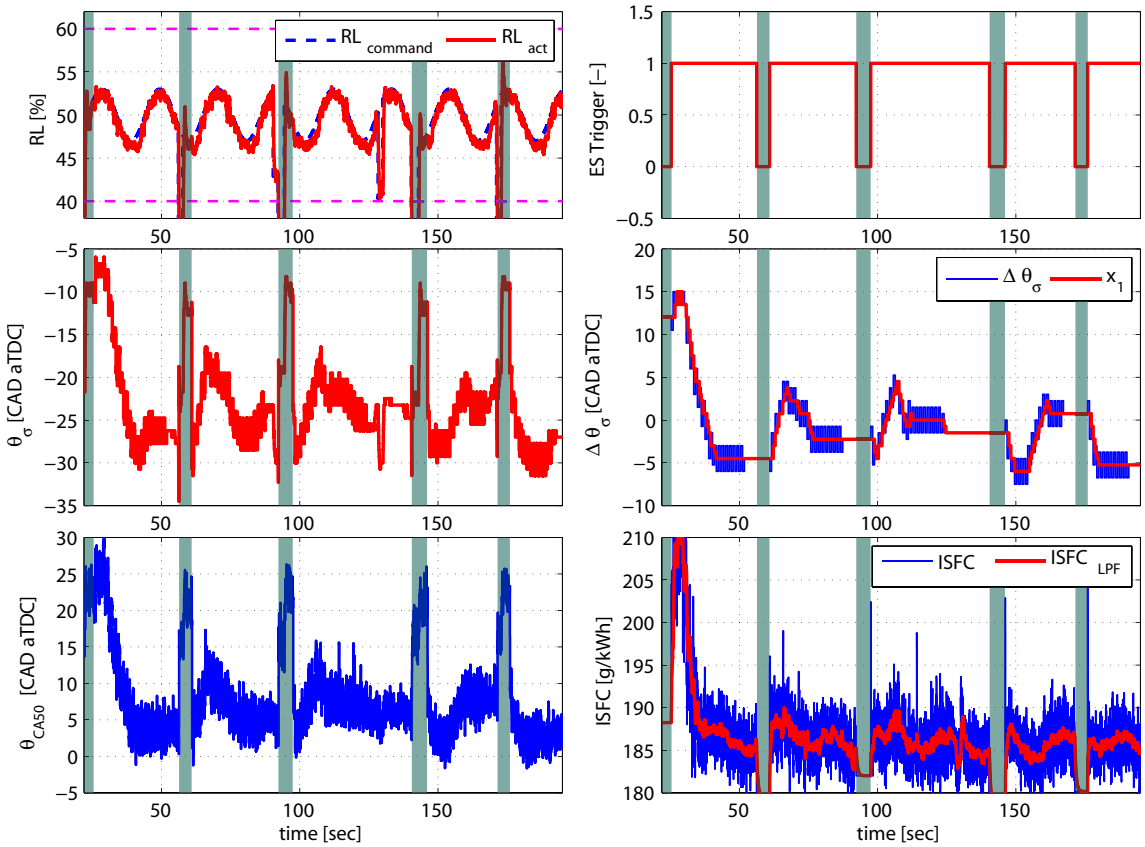

Figure 6.11 Extremum seeking control test result : N = 2000 RPM, Relative Load = 50%, $\Delta\theta_{\sigma,0}$ = 12 CAD, A_{RL} = 3%, f_{RL} = 0.05, fuel = E85.

In summary, the implemented ES algorithm in the dynamometer engine has been tested to accomplish the optimal spark timing under various transient load conditions introduced using sinusoidal perturbations of f_{RL} = 0.01, 0.05, 0.1 and 0.15 Hz under nominal load level, 50% RL. The ES finds and maintains the best ISFC (between 185 to 188 g/kWh) even under these transient load conditions. There is a constant change in the compensated ES spark signal $\Delta\theta_{\sigma}$ around -2 CAD (i.e. 14 CAD advanced from the initial ECU offset) and the values achieved demonstrate convincingly that the ES algorithm controls spark timing near its optimum value to achieve best fuel efficiency.

6.4 Conclusion

This chapter demonstrated an ES control algorithm via experiments applied in an experimental engine mounted in a dynamometer facility. First, NMEP and NSFC characteristics have been analyzed based on different spark timing and variable valve timing. Due to

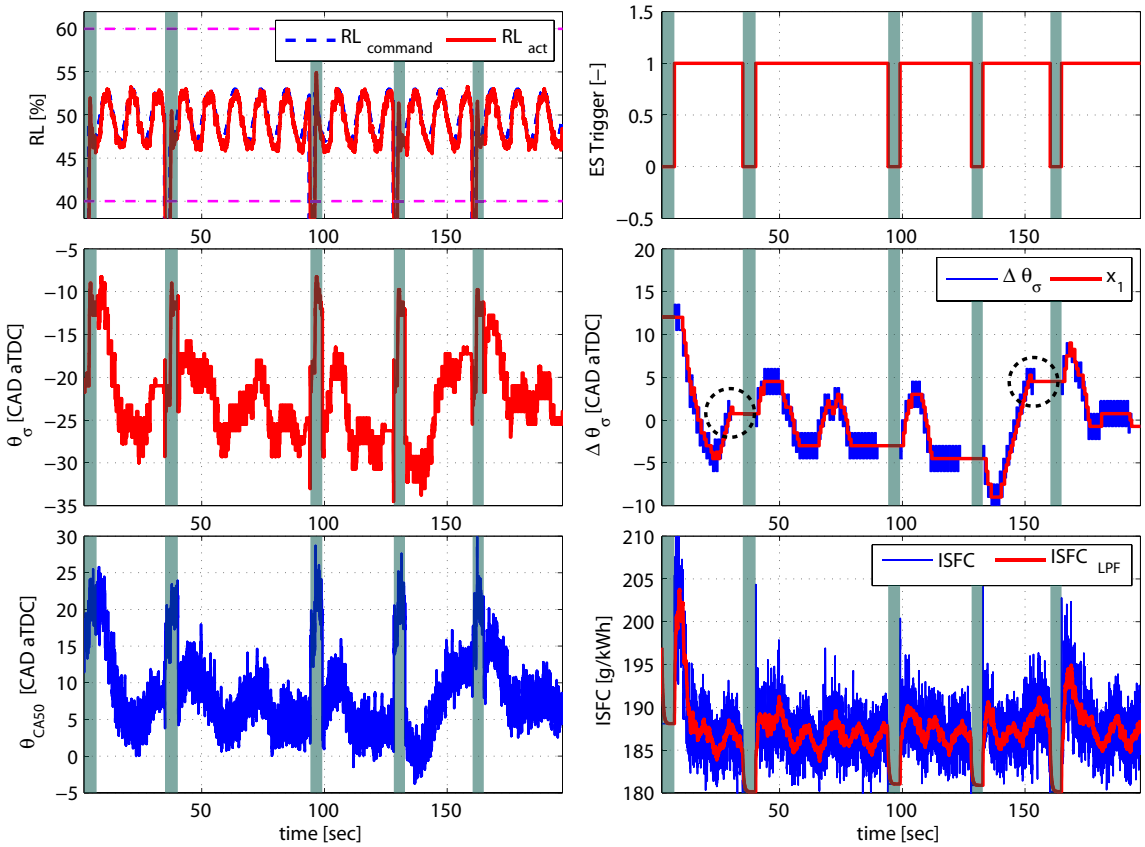

Figure 6.12 Extremum seeking control test result : N = 2000 RPM, Relative Load = 50%, $\Delta\theta_{\sigma,0}$ = 12 CAD, A_{RL} = 3%, f_{RL} = 0.1, fuel = E85.

small and negligible NSFC changes for IVO changes, the ES control has been tested only for spark timing. The ES control algorithm was implemented after minor modifications and two different types of load inputs have been applied during the ES algorithm test in the dynamometer engine, namely fixed and transient load inputs. The transient load input has been realized with biased sinusoidal load commands with various amplitudes and frequencies. It takes approximately 20 seconds to search the optimal spark timing under the fixed load condition. For the transient load inputs, the current ES algorithm determines the optimum up to the frequency of f_{RL} = 0.1 Hz. For higher frequencies, where the load changes faster than the rate of the ES convergence, the ES algorithm maintains the best ISFC despite variations in spark.

Our results show the potential benefits of the ES methodology but also highlight the need to modify the ES algorithm in a real vehicle if the normal driving profile involves aggressive driving. To make a better decision whether the converged optimum value is true or not, for instance, an additional diagnostic logic can be involved on top of the spark ES excitation stop criteria to compare a converged spark timing and an associated specific fuel

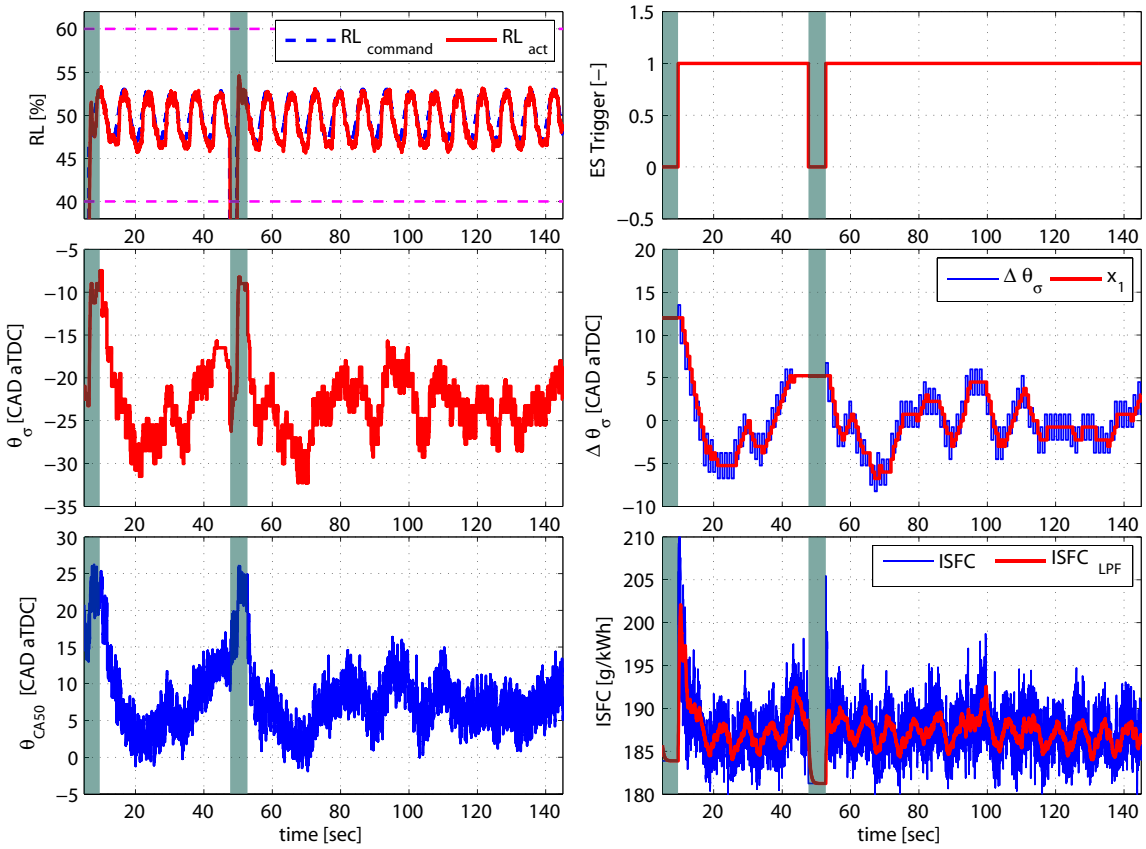

Figure 6.13 Extremum seeking control test result : N = 2000 RPM, Relative Load = 50%, $\Delta\theta_{\sigma,0}$ = 12 CAD, A_{RL} = 3%, f_{RL} = 0.15, fuel = E85.

consumption (SFC) level with the nominal ECU map value. Also, the undesirable convergence events can be filtered out with an accumulative moving average methodology after a couple of convergence events. It is envisioned that the ES will be coupled with an algorithm that identifies the driving patter (driver clarification) and enables the ES algorithm judiciously.

Chapter 7
Conclusions and Future Work

7.1 Conclusions

In this section we summarize the work completed in this dissertation. We first introduced two different types of gasoline engines which improves the engine fuel efficiency and reduce the emissions in Chapter 1:

- a heated-air intake homogeneous charge compression ignition (HCCI) engine capable to increase combustion efficiency while reducing NOx emissions due to low peak in-cylinder temperatures through the lean combustion characteristics (covered in Chapter 2 and 3),
- a turbocharged (TC) spark ignition direct injection (SIDI) engine equipped with variable valve timing (VVT) in flex-fuel vehicles (FFV) which improves significant thermal efficiency with simultaneous engine-out emission reduction due to the potential for engine diwnsizing with the internally recirculated exhaust gas (covered in Chapter 4, 5 and 6).

In Chapter 2 we developed the first crank-angle based control oriented model for a single cylinder heated-inlet air HCCI engine with two intake throttles that control the cold and hot air streams. The crank-angle based HCCI engine model combines the manifold filling dynamics (including the intake and exhaust manifold model in section 2.4.1 and 2.4.2) and the cylinder dynamics (including the Woschni heat transfer to consider the heat transfer through the cylinder parts in section 2.5.3 and the Arrhenius integral to compute the start of combustion θ_{SOC} in section 2.5.5). The good match in the prediction and validation using the dynamometer engine test data is also shown in section 2.6 and 2.7.

Although the phenomenological crank-angle resolved HCCI engine developed in Chapter 2 are indispensable for understanding and simulating HCCI combustion, low-order models are necessary for real-time feedback controller and observer design. A mean value model (MVM) of single cylinder heated air HCCI engine was, therefore, introduced in Chapter 3 validated using transient dynamometer engine test data. In section 3.3, we pro-

posed that the combustion duration, $\Delta\theta_{comb}$, defined as the duration between the crank angle of 10 and 90% fuel burned, can be a good proxy for both combustion stability and fuel efficiency with respect to the covariance of indicated mean effective pressure (IMEP) and indicated specific fuel consumption (ISFC), respectively. Based on this observation and the novel allocation of two actuators (hot and cold throttles), a feedforward compensator and a PI feedback controller were developed to regulate $\Delta\theta_{comb}$ and simulated with both the MVM and crank-angle based model in section 3.4.

A control-oriented mean value model for a flex-fuel vehicle (FFV) turbocharged (TC) spark ignition direct injection (SIDI) engine with variable valve timing (VVT) was introduced and parameterized in Chapter 4. The static VVT scheduling scheme that takes various engine performance variables (e.g. fuel efficiency, emission and combustion stability) into consideration was described in Section 4.3. The dynamic interaction between the throttle and the valve overlap and their transient effects on the intake manifold pressure and cylinder charge was analyzed in section 4.4. Then, the valve compensator was designed to improve the transient behaviors of cylinder charge during tip-ins and tip-outs when the VVT system transits from one set-point position to other as commanded by the static VVT schedule in section 4.4. This valve compensator was intended to regulate the load disturbance induced by the VVT perturbations for the on-board calibration such as an extremum seeking (ES) presented in Chapter 5.

In Chapter 5, the mean value model from Chapter 4 was modified to predict the combustion phasing (i.e. crank angle of 50% fuel burned θ_{CA50}) and mean effective pressure (MEP) at various engine speeds and loads. Statistical models were then introduced in section 5.2 to predict the effect of internal residual gas recirculation (iEGR) and spark timing θ_σ in the combustion efficiency and in the cycle-to-cycle combustion variations such that the engine model imitates well the real engine performance with respect to the optimal operating points of VVT and θ_{CA50} along with the practical noise levels of the engine performance variables. An ES controller was then designed in section 5.3 to determine the optimum VVT position and spark timing for the minimum net specific fuel consumption (NSFC) at given engine speeds and loads. Simulation results using the engine model with the designed extremum seeking algorithm showed that both spark timing θ_σ and VVT values can converge to the optimum within 60 seconds even though this convergence rate may be engine and vehicle specific.

The implementation and verification of the ES control algorithm in a dynamometer engine was presented in Chapter 6. Due to small and negligible NSFC changes for different IVO values, the ES control has been tested only for spark timing in an experimental engine. The ES control algorithm after minor modifications was implemented with the rapid pro-

totyping and two different types of load inputs have been applied during the ES algorithm test in the dynamometer engine, namely fixed and transient load inputs. The transient load input has been realized with biased sinusoidal load commands with various amplitudes and frequencies. The experimental results showed approximately 20 seconds to converge on the optimal spark timing under the fixed load condition. For the transient load inputs, the current ES algorithm determined the optimum up to the frequency of f_{RL} = 0.1 Hz (a half period of 5 seconds). For higher frequencies, where the load changes faster than the rate of the ES convergence, the ES algorithm maintains the best ISFC despite small variations in spark.

7.2 Future Work

In this section, we propose potential future directions related to the work completed in this dissertation. In the HCCI mean-value model presented in Chapter 3, the cylinder wall thermal dynamics are necessary to be modified to fully capture the first order response of the crank angle of 50% fuel burned θ_{CA50} [88], which requires more steady-state and transient experimental data. The engine was not available for demonstrating the closed-loop performance unfortunately due to the limited time for the dynamometer facility hence, in this dissertation, we only provided simulation results of the designed controller with the crank-angle resolved nonlinear model in [53]. To complete the verification of the designed controller performance, the implementation of the closed-loop controller in the dynamometer engine facility must be conducted.

In addition to the HCCI combustion, the mode transition between HCCI and SI combustion is also one of the most active research efforts [89, 90, 91, 92] to run HCCI engines over the entire engine speed and load range limits its practical application. The SI combustion model developed in Chapter 5 can be a good basis to predict the both HCCI and SI combustion behaviors and its transitions. Notice that the allocation of two throttle actuators (hot and cold) in section 3.4 was performed such that less hot throttle open with more cold throttle open can be achieved when the mode switch from HCCI to SI is required beyond the HCCI load limit (approximately 5 IMEP bars). Moreover, the expansion of the HCCI upper load limits with intake air boosting by a turbocharger can be well extended from this dissertation work.

The designed valve compensator in Chapter 4 was able to resolve the addressed transient coupling between throttle and VVT during load changes. Another transient air charge coupling can be addressed with the turbocharger wastegate actuator especially at high loads

[93, 94]. An additional controller design, which takes into account the effect of a turbocharger wastegate actuator on the cylinder charge flow rate together with throttle and VVT, can be proposed to improve the transient behavior over entire load conditions up to boosted operations. The dynamometer test with the extremum seeking (ES) controller for the optimal VVT was not completed in this dissertation due to lack of the dynamometer engine test data to analyze the effects of VVT and internal exhaust gas recirculation (iEGR) on the combustion efficiency and stability explicitly for the new engine with a higher compression ratio and a longer intake cam profile. Further investigation, therefore, must be performed for better understanding of VVT influences on both engine fuel efficiency and air-path characteristics, and successful implementation of the VVT ES control algorithm in the real engine.

Bibliography

[1] G. Singh, "Advanced combustion engine research and development," U.S. Department of Energy," Annual Progress Reports, 2009.

[2] A. C. Alkidas, "Combustion advancements in gasoline engines," *Energy Conversion and Management*, vol. 48, pp. 2751 –2761, 2007.

[3] M. Christensen, B. Johansson, and P. Einewall, "Homogeneous charge compression ignition (HCCI) using isooctane, ethanol and natural gas - A comparison with spark ignition operation," *SAE paper 972874*.

[4] S. Onishi, S. H. Jo, K. Shoda, P. D. Jo, and S. Kato, "Active thermo-atmosphere combustion (ATAC)–a new combustion process for internal combustion engines," *SAE Paper 790501*.

[5] J. Warnatz, U. Maas, and R. W. Dibble, *Combustion: physical and chemical fundamentals, modeling and simulation, experiments, pollutant formation*. Springer, 2006.

[6] H. Zhao, Z. Peng, and N. Ladommatos, "Understanding of controlled autoignition combustion in a four-stroke gasoline engine," *Journal of Automobile Engineering*, vol. 215, no. 12, pp. 1297 – 1310, 2001.

[7] J. Yang, T. Culp, and T. Kenney, "Development of a gasoline engine system using HCCI technoloty - the concept and the test results," *SAE Paper 2002-01-2832*.

[8] G. M. Shaver, "Stability analysis of residual-affected HCCI using convex optimization," *Control Engineering Practice*, vol. 17, pp. 1454–1460, 2009.

[9] J. O. Olsson, P. Tunestal, B. Johansson, S. Fiveland, R. Agama, M. Willi, and D. Assanis, "Compression ratio influence on maximum load of a natural gas fueled HCCI engine," *SAE paper 2002-01-0111*.

[10] R. H. Stanglmaier and C. E. Roberts, "Homogeneous charge compression ignition (HCCI): Benefits, compromises, and future engine applications," *SAE paper 1999-01-3682*.

[11] G. Haraldsson, P. Tunestål, and B. Johansson, "HCCI combustion phasing in a multi cylinder engine using variable compression ratio," *SAE paper 2002-01-2858*.

[12] P. A. Caton, H. H. Song, N. B. Kaahaaina, and C. F. Edwards, "Strategies for achieving residual-effected homogeneous charge compression ignition using variable valve actuation," *SAE Paper 2005-01-0165*.

[13] F. Agrell, H.-E. Ångström, B. Eriksson, J. Wikander, and J. Linderyd, "Integrated simulation and engine test of closed-loop HCCI control by aid of variable valve timings," *SAE paper 2003-01-0748*.

[14] S. Yamaoka, H. Kakuya, S. Nakagawa, T. Okada, A. Shimada, and Y. Kihara, "HCCI operation control in a multi-cylinder gasoline engine," *SAE paper 2005-01-0120*.

[15] D. J. Rausen, A. G. Stefanopoulou, J.-M. Kang, J. A. Eng, and T.-W. Kuo, "A mean-value model for control of homogeneous charge compression ignition (HCCI) engines," *ASME Journal of Dynamic Systems, Measurement and Control*, vol. 127, no. 3, pp. 355–362, 2005.

[16] N. Ravi, H.-H. Liao, A. F. Jungkunz, and J. C. Gerdes, "Modeling and control of exhaust recompression HCCI using split injection," in *Proceedings of American Control Conference*, 2010, pp. 3794–3802.

[17] J.-O. Olsson, P. Tunestal, and B. Johansson, "Closed-loop control of an HCCI engine," *SAE Paper 2001-01-1031*.

[18] G. Haraldsson, P. Tunestål, B. Johansson, and J. Hyvonen, "HCCI closed-loop combustion control using fast thermal management," *SAE paper 2004-01-0943*.

[19] ——, "Transient control of a multi cylinder HCCI engine during a drive cycle," *SAE paper 2005-01-0153*.

[20] S.-C. Kong, C. D. Marriott, R. D. Reitz, and M. Christensen, "Modeling and experiments of HCCI engine combustion using detailed chemical kinetics with multidimensional CFD," *SAE Paper 2001-01-1026*.

[21] S. Tanaka, F. Ayala, and J. C. Keck, "A reduced chemical kinetic model for HCCI combustion of primary reference fuels in a rapid compression machine," *Combustion and Flame*, vol. 133, pp. 467–481, 2003.

[22] G. Shaver, J. Gerdes, P. Jain, P. Caton, and C. Edwards, "Modeling for control of HCCI engines," in *Proceedings of American Control Conference*, Denver, Colorado, June 2003.

[23] S. B. Fiveland and D. N. Assanis, "Development of a two-zone HCCI combustion model accounting for boundary layer effects," *SAE Paper 2001-01-1028*.

[24] H. Barths, C. Felsch, and N. Peters, "Mixing models for the two-way-coupling of CFD codes and zero-dimensional multi-zone codes to model HCCI combustion," *Combustion and Flame*, vol. 156, no. 1, pp. 130 – 139, 2009.

[25] N. J. Killingsworth, S. M. Aceves, D. L. Flowers, and M. Krstić, "A simple HCCI engine model for control," in *Proceedings of the IEEE International Conference on Control Applications*, Munich, Germany, October 2006.

[26] N. Ravi, M. J. Roelle, A. F. Jungkunz, and J. C. Gerdes, "A physically based two-state model for controlling exhaust recompression HCCI in gasoline engines," in *Proceedings of ASME International Mechanical Engineering Congress and Exposition*, 2006, pp. 483–492.

[27] N. Ravi, M. J. Roelle, and J. C. Gerdes, "Controller-observer implementation for cycle-by-cycle control of an HCCI engine," in *Proceedings of ASME International Mechanical Engineering Congress and Exposition*, 2007, pp. 177–185.

[28] J. Bengtsson, P. Strandh, R. Johansson, P. Tunestal, and B. Johansson, "Model predictive control of homogeneous charge compression ignition (HCCI) engine dynamics," in *Proceedings of 2006 IEEE International Conference on Control Applications*, 2006, pp. 1675 –1680.

[29] A. Widd, K. Ekholm, P. Tunestal, and R. Johansson, "Experimental evaluation of predictive combustion phasing control in an HCCI engine using fast thermal management and VVA," in *Proceedings of IEEE International Conference on Control Applications*, 2009, pp. 334–339.

[30] C. J. Chiang, A. G. Stefanopoulou, and M. Janković, "Nonlinear observer-based control of load transitions in homogeneous charge compression ignition (HCCI) engines," *IEEE Transactions on Control Systems Technology (Special Issue on Control Applications in Automotive Engineering)*, May 2007.

[31] C.-J. Chiang and A. G. Stefanopoulou, "Sensitivity analysis of combustion timing and duration of homogeneous charge compression ignition (HCCI) engines," *Proceedings of American Control Conference*, 2006.

[32] H. M. Xu, M. L. Wyszynski, A. Megaritis, D. Yap, T. Wilson, J. Qiao, S. Richardson, S. Golunski, and S. Peucheret, "Research on expansion of operating windows of controlled homogeneous auto-ignition engines," *International Journal of Engine Research*, vol. 8, no. 1, pp. 29 – 40, 2007.

[33] B. Lecointe and G. Monnier, "Downsizing a gasoline engine using turbocharging with direct injection," *SAE Paper 2003-01-0542*.

[34] H. Kleeberg, D. Tomazic, O. Lang, and K. Habermann, "Future potential and development methods for high output turbocharged direct injected gasoline engines," *SAE Paper 2006-01-0046*.

[35] E. Sher and T. Bar-Kohany, "Optimization of variable valve-timing for maximizing performance of an unthrottled SI engine: a theoretical study," *Energy*, vol. 27, pp. 757–775, 2002.

[36] K. Atashkari, N. Nariman-Zadeh, M. Golcu, A. Khalkhali, and A. Jamali, "Modelling and multi-objective optimization of a variable valve-timing spark-ignition engine using polynomial neural networks and evolutionary algorithms," *Energy Conversion and Management*, vol. 48, pp. 1029–1041, 2007.

[37] T. Leroy, G. Alix, J. Chauvin, A. Duparchy, and F. L. Berr, "Fresh air charge and residual gas fraction on a dual independent variable valve timing SI engine," *SAE paper 2008-01-0983*.

[38] A. G. Stefanopoulou, J. S. Freudenberg, and J. W. Grizzle, "Variable camshaft timing engine control," *IEEE Transactions on Control Systems Technology*, vol. 8, pp. 23–34, 2000.

[39] M. Jankovic, , and S. W. Magner, "Variable cam timing: Consequences to automotive engine control design," in *15th IFAC Triennial World Congress*, 2002.

[40] A. G. Stefanopoulou and I. Kolmanovsky, "Analysis and control of transient torque response in engines with internal exhaust gas recirculation," *IEEE Transactions on Control Systems Technology*, vol. 7, no. 5, pp. 555 – 566, 1999.

[41] M. Jankovic, F. Frischmuth, A. Stefanopoulou, and J. A. Cook, "Torque management of engines with variable cam timing," *IEEE Control Systems Magazine*, vol. 18, no. 5, pp. 34 – 42, 1998.

[42] Y.-W. Kim, G. Rizzoni, and V. Utkin, "Automotive engine diagnosis and control via nonlinear estimation," *Control Systems Magazine, IEEE*, vol. 18, no. 5, pp. 84 –99, Oct. 1998.

[43] T. Leroy, J. Chauvin, and N. Petit, "Motion planning for experimental air path control of a variable-valve-timing spark ignition engine," *Control Engineering Practice*, vol. 17, no. 12, pp. 1432 –1439, 2009.

[44] M. Muller, E. Hendricks, and S. C. Sorenson, "Mean value modelling of turbocharged spark ignition engines," in *SAE Special Publications*, vol. 1330, Detroit, MI, USA, 1998, pp. 125 – 145.

[45] L. Eriksson, L. Nielsen, J. Brugard, J. Bergstrom, F. Pettersson, and P. Andersson, "Modeling of a turbocharged SI engine," *Annual Reviews in Control*, vol. 26 I, pp. 129 – 137, 2002.

[46] A. Y. Karnik, J. H. Buckland, and J. S. Freudenberg, "Electronic throttle and wastegate control for turbocharged gasoline engines," in *Proceedings of American Control Conference*, vol. 7, Portland, OR, United states, 2005, pp. 4434 – 4439.

[47] L. Jiang, A. Stefanopoulou, J. Vanier, and H. Yilmaz, "Parameterization and simulation for a turbocharged spark ignition direct injection engine with variable valve timing," in *SAE Technical Paper*, no. 2009-01-0680, Detroit, MI, United States, 2009.

[48] R. J. Wakeman and D. O. Wright, “Closed loop turbocharger control with transient wastegate functions,” in *SAE Special Publications*, Detroit, MI, Untied States, 1986, pp. 131 – 135.

[49] J. R. Zurlo, E. O. Reinbold, and J. Mueller, “Waukesha turbocharger control module: a tool for improved engine efficiency and response,” in *American Society of Mechanical Engineers, Internal Combustion Engine Division (Publication) ICE*, vol. 27-4, Fairborn, OH, USA, 1996, pp. 35 – 40.

[50] J. Buckland, J. Grizzle, J. Freudenberg, and J. J., “Estimation of exhaust manifold pressure in turbocharged gasoline engines with variable valve timing,” in *Proceedings of the ASME 2008 Dynamics Systems and Control Conference*, Ann Arbor, MI USA, 2008.

[51] J. H. Buckland, J. S. Freudenberg, G. J. W., and M. Jankovic, “Practical observers for unmeasured states in turbocharged gasoline engines,” in *Proceedings of American Control Conference*, Seattle, MO, United States, June 2009, pp. 2714–2719.

[52] C. D. Marriott, M. A. Wiles, J. M. Gwidt, and S. E. Parrish, “Development of a naturally aspirated spark ignition direct-injection flex-fuel engine,” *SAE Paper 2008-01-0319*.

[53] Y. Wang, S. Makkapati, M. Janković, M. Zubeck, and D. Lee, “Control oriented model and dynamometer testing for a single-cylinder, heated-air HCCI engine,” *SAE paper 2009-01-1129*, 2009.

[54] D. Lee, A. G. Stefanopoulou, S. Makkapati, and M. Janković, “Modeling and control of a heated air intake homogeneous charge compression ignition (HCCI) engine,” in *Proceedings of American Control Conference*, Baltimore, MD, USA, 2010.

[55] D. Lee, L. Jiang, H. Yilmaz, and A. G. Stefanopoulou, “Air charge control for turbocharged spark ignition engines with internal exhaust gas recirculation,” in *Proceedings of American Control Conference*, Baltimore, MD, USA, 2010.

[56] ——, “Preliminary resluts on optimal variable valve timing and spark timing control via extremum seeking,” in *Proceedings of the 2010 IFAC Symposium on Mechatronic Systems*, Cambridge, MA, USA, 2010.

[57] D. A. S. Fiveland, “A four-stroke homogeneous charge compression ignition engine simulation for combustion and performance studies,” *SAE Paper 2000-01-0332*.

[58] S. Salvador, D. Flowers, C. Westbrook, R. Smith, W. Pitz, R. Dibble, M. Christensen, and B. Johansson, “A multi-zone model for prediction of HCCI combustion and emissions,” *SAE Paper 2000-01-0327*.

[59] S.-C. Kong, C. Marriott, R. Reitz, and M. Christensen, “Modeling and experiment of HCCI engine combustion using detailed chemical kinetics with multidimensional CFD,” *SAE Paper 2001-01-1026*.

[60] J. Millet, F. Maroteaux, and F. Ravet, "Modeling of HCCI combustion by one step reaction function: in view of assisting the optimization of engine management system," *SAE Paper 2007-24-0033*.

[61] J. B. Heywood, *Internal Combustion Engine Fundamentals*. McGraw-Hill Inc, 1988.

[62] J. A. Caton and J. B. Heywood, "An experimental and analytical study of heat transfer in an engine exhuast port," *International Journal of Heat Mass Transfer*, vol. 24, pp. 581–595, 1981.

[63] G. Woschni, "A universally applicable equation for the instantaneous heat transfer coefficient in the internal combustion engine," *SAE Paper 670931*.

[64] Y. Shiao and J. J. Moskwa, "Cylinder pressure and combustion heat release estimation for SI engine diagnostics using nonlinear sliding observers," *IEEE Transactions on Control Systems Technology*, vol. 3, pp. 70–78, 1995.

[65] J. Chang, O. Güralp, Z. Filipi, and D. N. Assanis, "New heat transfer correlation for an HCCI engine derived from measurements of instantaneous surface heat flux," *SAE paper 2004-01-2996*.

[66] D. J. Rausen, A. G. Stefanopoulou, J.-M. Kang, J. A. Eng, and T.-W. Kuo, "A mean-value model for control of homogeneous charge compression ignition (HCCI) engines," in *Proceedings of American Control Conference*, 2004, pp. 125–131.

[67] D. E. Finkel, *DIRECT Optimization Algorithm User Guide*, North Carolina State University.

[68] *Manual for optimization toolbox*, MathWorks, Inc.

[69] M. Y. Au, J. W. Girard, R. Dibble, D. Flowers, S. M. Aceves, J. Martinez-Frias, R. Smith, C. Seibel, and U. Maas, "1.9-liter four-cylinder HCCI engine operation with exhaust gas recirculation," *SAE paper 2001-01-1894*, 2001.

[70] F. Agrell, H.-E. Ångström, B. Eriksson, J. Wikander, and J. Linderyd, "Integrated simulation and engine test of closed-loop HCCI control by aid of variable valve timings," *SAE paper 2003-01-0748*, 2003.

[71] G. M. Shaver, M. Roelle, and J. C. Gerdes, "A two-input two-output control model of HCCI engines," in *Proceedings of 2006 American Control Conference*, 2006.

[72] G. Haraldsson, P. Tunestål, B. Johansson, and J. Hyvonen, "HCCI closed-loop combustion control using fast thermal management," *SAE paper 2004-01-0943*, 2004.

[73] M. J. Roelle, N. Ravi, A. F. Jungkunz, and J. C. Gerdes, "A dynamic model of recompression HCCI combustion including cylinder wall temperature," in *Proceedings of IMECE2006*, 2006.

[74] D. Blom, M. Karlsson, K. Ekholm, P. Tunestal, and R. Johansson, "HCCI engine modelling and control using conservation principles," *SAE Paper 2008-01-0789*.

[75] C.-J. Chiang, A. G. Stefanopoulou, and M. Janković, "Nonlinear observer-based control of load transitions in homogeneous charge compression ignition engines," *IEEE Transactions on Control Systems Technology*, vol. 35, pp. 438–448, 2007.

[76] J. C. Kantor, "A dynamical instability of spark-ignited engines," *Science*, vol. 224, pp. 1233–1235, 1984.

[77] D. J. Rausen, A. G. Stefanopoulou, J.-M. Kang, J. A. Eng, and T.-W. Kuo, "A mean-value model for control of homogeneous charge compression ignition (HCCI) engines," *ASME Journal of Dynamic Systems*, vol. 127, no. 3, pp. 355–362, 2005.

[78] E. Pipitone, "A comparison between combustion phase indicators for optimal spark timing," *Journal of Engineering for Gas Turbines and Power*, vol. 130, no. 5, 2008.

[79] Z. Ivanic, F. Ayala, J. Goldwitz, , and J. B. Heywood, "Effects of hydrogen enhancement on efficiency and NOx emissions of lean and EGR-diluted mixtures in a SI engine," *SAE Paper 2005-01-0253*.

[80] M. Krstic, "Performance improvement and limitations in extremum seeking control," *Systems & Control Letters*, vol. 39, no. 5, pp. 313 – 326, 2000.

[81] J.-Y. Choi, M. Krstic, K. Ariyur, and J. Lee, "Extremum seeking control for discrete-time systems," *IEEE Transactions on Automatic Control*, vol. 47, no. 2, pp. 318 –323, 2002.

[82] M. K. Kartik B. Ariyur, *Real-time optimization by extremum-seeking control*. Wiley-IEEE, 2003.

[83] O. Jacobs and G. Shering, "Design of a single-input sinusoidal perturbation extremum-control system," *Proceedings IEE*, vol. 115, pp. 212–217, 1968.

[84] K. S. Peterson and A. G. Stefanopoulou, "Extremum seeking control for soft landing of an electromechanical valve actuator," *Automatica*, vol. 40, no. 6, pp. 1063–1069, 2004.

[85] K. B. Ariyur and M. Kristic, "Multivariable extremum seeking feedback: Analysis and design," *Fifteenth International Symposium on Mathematical Theory of Networks and Systems*, 2002.

[86] D. Popovic, M. Jankovic, S. Magner, and A. R. Teel, "Extremum seeking methods for optimization of variable cam timing engine operation," *IEEE Transactions on Control Systems Technology*, vol. 14, no. 3, pp. 398–407, May 2006.

[87] *Manual for INTECRIO*, ETAS, Inc.

[88] A. Widd, P. Tunestal, and R. Johansson, "Physical modeling and control of homogeneous charge compression ignition (HCCI) engines," in *Proceedings of the 47th IEEE Conference on Decision and Control*, 2008, pp. 5615–5620.

[89] L. Koopmans, H. Strom, S. Lundgren, O. Backlund, and I. Denbratt, "Demonstrating a SI-HCCI-SI mode change on a Volvo 5-cylinder electronic valve control engine," *SAE paper 2003-01-0753*.

[90] N. Milovanovic, D. Blundell, S. Gedge, and J. Turner, "SI-HCCI-SI mode transition at different engine operating conditions," *SAE paper 2005-01-0156*.

[91] G. M. Shaver, M. J. Roelle, and J. C. Gerdes, "Modeling cycle-to-cycle dynamics and mode transition in HCCI engines with variable valve actuation," *Control Engineering Practice*, vol. 14, pp. 213 –222, 2006.

[92] H. Wu, N. Collings, S. Regitz, J. Etheridge, and M. Kraft, "Experimental investigation of a control method for SI-HCCI-SI transition in a multi-cylinder gasoline engine," *SAE paper 2010-01-1245*.

[93] T. Leroy, J. Chauvin, and N. Petit, "Controlling air and burned gas masses of turbocharged VVT SI engines," in *47th IEEE Conference on Decision and Control*, 2008, pp. 5628 –5634.

[94] ——, "Controlling in-cylinder composition on turbocharged variable-valve-timing spark ignition engines," in *Proceedings of European Control Conference*, 2009, pp. 3803–3808.